Dissertations, Master's Theses and Master's Reports

2019

Online Learning of the Spatial-Temporal Channel Variation in Underwater Acoustic Communication Networks

Wensheng Sun
Michigan Technological University, wsun3@mtu.edu

ONLINE LEARNING OF THE SPATIAL-TEMPORAL CHANNEL VARIATION

IN UNDERWATER ACOUSTIC COMMUNICATION NETWORKS

By

Wensheng Sun

A DISSERTATION

Submitted in partial fulfillment of the requirements for the degree of

DOCTOR OF PHILOSOPHY

In Electrical Engineering

MICHIGAN TECHNOLOGICAL UNIVERSITY

2019

This dissertation has been approved in partial fulfillment of the requirements for the Degree of DOCTOR OF PHILOSOPHY in Electrical Engineering.

Department of Electrical and Computer Engineering

Dissertation Advisor: *Dr. Zhaohui Wang*

Committee Member: *Dr. Michael C. Roggemann*

Committee Member: *Dr. Andrew Barnard*

Committee Member: *Dr. Jiguang Sun*

Department Chair: *Dr. Glen E. Archer*

Dedication

This work is dedicated to my parents, my wife and my elder sister.

Contents

List of Figures

List of Tables

Preface

This thesis summarizes the research I have conducted during my Ph.D. program in the Electrical and Computer Engineering Department at Michigan Technological University. Under the supervision of my advisor, Dr. Zhaohui Wang, two journal articles and four conference papers were published, which are partially presented in this thesis.

The contents in Chapter 2 include materials published in [1, 2, 3, 4]. As the first author of [1], I designed and conducted the KWAUG14 experiment, and completed the data analysis under the supervision the second author, my advisor Dr. Zhaohui Wang. Dr. Wang also provides help in the presentation of the paper. As the third and fourth author, Dr. Jamalabdollahi, Mohsen and Dr. Reza Zekavat provides insightful advice to the paper. The work was completed by me and my advisor. As the first author of [2], I lead the experimental data collection and analysis under the supervision of the third author Dr. Zhaohui Wang. As the second author, Dr. Chaofeng Wang provides help during the experiment and data collection. As the fourth author, Dr. Min Song provides helpful comments on the presentation. As the second author of [3] and the fourth author of [4], I lead the experimental data collection and data processing and presentation under the guidance of my advisor.

The work in Chapter 3 was published in [5]. As the first author, under the guidance of my adivsor, I designed and implemented the algorithm and conducted the performance analysis with simulated and experimental data. This article was completed by me and my advisor.

The work in Chapter 4 has been submitted to "IEEE Open Journal of the Communications Society". As the first author, I designed and implemented the algorithm under the guidance of my advisor, who is the second author. As the third author, Dr. Zafar Iqbal provides invaluable advice about the GMP algorithm.

Acknowledgments

I am deeply grateful to my advisor, Dr. Zhaohui Wang, whose supports enable me focusing on my research. All the insightful advice about research and life in general reshape my attitude towards science and engineering. It is not possible to finish my program without her help.

I am indebted to my advisory committee, Dr. Michael C. Roggemann, Dr. Andrew Barnard and Dr. Jiguang Sun. Their reviews about the thesis are invaluable, based on which significant improvements have been made.

It was my honor to work with Professor Min Song, Professor.Daniel R. Fuhrmann, Dr. Zafar Iqbal, Dr. Reza Barazideh, Professor Balasubramaniam Natarajan and Professor Nina Mahmoudian. I am obliged to Dr. Guy Meadows, Mike Abbott, Jamey Anderson, and Colin Tyrell from the Great Lakes Research Center for their support with the experiments. I am beholden to my colleagues: Dr. Chaofeng Wang, Li Wei, Zijian Zhu, Krishna Chaitanya Poduru, and Yi Zhang for their help and discussions. I am thankful to all the friends I have made during this journey, their presence and companion makes this journey a lot more memorable.

Thank my parents and my sister for their love and support. Thank my parent-in-laws for helping me psychologically and sharing my emotion. Last but not the least,

Abstract

Influenced by environmental conditions, underwater acoustic (UWA) communication channels exhibit spatial and temporal variations, posing significant challenges for UWA networking and applications. This dissertation develops statistical signal processing approaches to model and predict variations of the channel and relevant environmental factors.

Firstly, extensive field experiments are conducted in the Great Lakes region. Three types of the freshwater river/lake acoustic channels are characterized in the aspects of statistical channel variations and sound propagation loss, including stationary, mobile and under-ice acoustic channels. Statistical data analysis shows that relative to oceanic channels, freshwater river/lake channels have larger temporal coherence, higher correlation among densely distributed channel paths, and less sound absorption loss. Moreover, variations of the under-ice channels are less severe than those in open water in terms of multipath structure and Doppler effect. Based on the observed channel characteristics, insights on acoustic transceiver design are provided, and the following two works are developed.

online modeling and prediction of slowly-varying channel parameters are investigated,

by exploiting their inherent temporal correlation and correlation with water environment. The temporal evolution of the channel statistics is modeled as the summation of a time-varying environmental process, and a Markov latent process representing unknown or unmeasurable physical mechanisms. An algorithm is developed to recursively estimate the unknown model parameters and predict the channel parameter of interest. The above model and the recursive algorithm are further extended to the channel that exhibits periodic dynamics. The proposed models and algorithms are evaluated via extensive simulations and data sets from two shallow-water experiments. The experimental results reveal that the average channel-gain-to-noise-power ratio, the fast fading statistics, and the average delay spread can be well predicted.

The inhomogeneity of the sound speed distribution is challenging for Autonomous underwater vehicles (AUVs) communications and acoustic signaling-based AUV localization due to the refraction effect. Based on the time-of-flight (TOF) measurements among the AUVs, a distributed and cooperative algorithm is developed for joint sound speed estimation and AUV tracking. The joint probability distribution of the time-of-flight (TOF) measurements, the sound speed parameters and the AUV locations are represented by a factor graph, based on which a Gaussian message passing algorithm is proposed after the linearization of nonlinear measurement models. Simulation results show that the AUV locations and the sound speed parameters can be tracked with satisfying accuracy. Moreover, significant localization improvement can be achieved when the sound speed stratification effect is taken into consideration.

Chapter 1

Introduction

Planet earth is known as "blue marble", more than 70% of its surface is covered by water. Human as dwellings of this planet conduct all kinds of activities related to water, including but not limited to deep ocean and polar region exploration, undersea natural resource exploitation, recreational sports and military activities. Most of the activities require data communication or status monitoring and consist of the drive for underwater communications.

Common carriers of information for underwater communication include radio wave, optical wave, magnetic wave and acoustic wave [6, 7, 8]. Among them the most popular carrier for long distance communication is acoustic wave due to its unique characteristics compared with other candidates [8].

1.1 Characteristics of the Underwater Acoustics Channels

As a mechanical wave, acoustic wave has a relative lower frequency than electromagnetic (EM) waves. The acoustic frequency ranges from 10 Hz to 100 kHz [9], whilst the frequency of EM waves is several orders of magnitude higher than acoustics. Acoustics have a relatively slow propagation speed in water, the nominal propagation speed is 1500 m/s in sea water and smaller in fresh water. On the contrary, the nominal speed of optical and radio wave is significantly higher, i.e. approximately 2.25×10^8 m/s.

Directly related to the acoustic propagation, underwater acoustic communication channels also have many signature properties compared to terrestrial radio channels.

- Large Doppler effect. Due to the low propagation speed, underwater acoustic channels exhibit large Doppler effect due to the movement of the medium and transmitting and receiving platform. The Doppler shift is defined as

$$f = \frac{c \pm v_r}{c \pm v_s} f_0, \tag{1.1}$$

  where the v_r and v_s are the speed of the receiver and transmitter, respectively.

f_0 is the frequency of the original wave. It can be observed that a relatively slow movement can cause significant Doppler shift in the underwater acoustic environment since the speed of sound is 5 order of magnitude less than the speed of EM wave.

- Large delay spread. Different from terrestrial radio channels, underwater acoustic channels are featured with severe multipath effect caused by the reflections of the boundary of the water body and sometimes refraction effect, such as the SOFAR channel. While the typical delay spread in terrestrial radio channels is in the order of nanoseconds, underwater acoustic channels could have a delay spread in the order of milliseconds. Due to the highly coherent channels, special algorithms should be designed to decode and estimate the underwater acoustic channels [10].

- Limited bandwidth. As mentioned in the previous section, the frequency of acoustics ranges from 1 - 100 kHz. This essentially constrains the available bandwidth for communication use. Due to the drive for high data throughput, modern underwater acoustic communication systems usually use the high frequency band.

- Transmission loss. The smaller propagation loss in water is the most important property that makes acoustics the popular choice of carrier for long distance underwater wireless communication. Typically, the sound wave can propagate a distance of several kilometers. In special environments such as the SOFAR

channel, it can even propagate hundreds of kilometers [11]. On the contrary, the radio or optical waves can only propagate a distance of several tens meters. Thus, radio and optics are commonly used for short-distance underwater communications.

1.2 Spatial-Temporal Variations of the UWA Channels

Different from terrestrial radio channels, underwater acoustic channels are prone to variations rooted in the change of the acoustic wave propagation and ambient noise.

- The temporal channel variations can be categorized as fast variations and slow variations, which are also known as fast fading and slow fading in wireless communications. Fast variations is caused by the multipath propagation of the acoustic waves due to reflection at the boundary. Fast variation statistics are highly correlated with the environment. For example, the wind speed changes the surface dynamic, which in turn could change the multipath structure of the channel. Moreover, wind and rain drops creates bubbles and changes the reflection and scattering of the acoustic waves near surface. In terrestrial radio channels, slow channel variations are usually caused by blocking of the signals.

Although this is also a reason for the slow variations in UWA channels, sound speed variation is an additional cause of shadowing in underwater environment.

- The spatial variations is mainly caused by the heterogeneous sound speed distribution in water. The sound stratification effect causes refraction of acoustic waves, leading to non-straight line sound propagation and the convergence of acoustic energy in some regions while limited acoustic energy in other regions. The sound speed in water varies with environment factors, such as salinity, temperature and pressure [12]. In shallow water environment such as river and lake, the temperature structure of the water column is the major factor on the speed of sound. In deep ocean environment, the pressure plays the most important role. Typically, the sound speed increases with depth as the pressure also increases. The plot sound speed versus depth is known as sound speed profile (SSP). It dominates the propagation of the acoustic wave. According to Snell's Law, the acoustic waves bend upwards in a increasing SSP and vice versa. Knowledge of the sound speed is critical for the design, deployment and performance analysis of an underwater communication system.

- Another important aspect of a UWA channel is the ambient noise. The ambient noise in the communication frequency band above 1 kHz is primarily caused by heavy precipitation, wind-induced bubble and spray, heavy traffic noise and thermal noise [9]. The hydrodynamic noise, generated by bubbles, whitecaps,

water droplets, surface waves and turbulence, are highly related to the time-varying environmental factors. For the frequency band from 1 kHz to 25 kHz, Knudsen's curves [13] have been popularly used to depict the dependence of hydrodynamic noise on the sea state [14],

$$NL = 56 + 19 \log_{10}(ss) - 17 \log_{10}(f), \qquad (1.2)$$

where NL is the noise level in dB re $1\mu Pa/\sqrt{Hz}$, f is the frequency in kHz, $1 < ss < 6$ is the sea state which is linearly related to the mean wind speed in m/s [9]. Based on extensive field measurements, the empirical models for the sound pressure level cause by the wind and rain drops are obtained via curve fitting in [15]. For the wind-generated sound in the frequency band from 1 kHz to 50 kHz, the noise pressure level in dB re $1\mu Pa^2/Hz$ is modeled as

$$NL = -15.7 \log_{10}(f/8) + 20 \log_{10}(53.91V - 104.5), \qquad (1.3)$$

where V is the wind speed in m/s and f is the frequency in kHz. The rain fall induced noise pressure level in dB re $1\mu Pa^2/Hz$ in the band of 1 kHz-10 kHz is

$$NL = \log_{10}(f/5) \times [8.33 \log_{10}(R) - 14.3] + 15.4 \log_{10}(R) + 42.4, \qquad (1.4)$$

where f is the frequency in kHz, and R is the rainfall rate in the range of

6

$2 \sim 200$ millimeter/hour.

1.3   Contributions

In this thesis, the challenging spatial-temporal variation of the underwater acoustic channels are identified. Specifically, the large scale temporal channel variation is modeled and predicted in a point-to-point communication link. Moreover, sound speed, whose variation accounts for the large-scale variation of the acoustic channels , is estimated and tracked in a mobile sensor network.

In Chapter 2, based on extensive experimental data, this work characterized the acoustic channels in freshwater rivers and lakes with and without ice coverage, and compared the channel characteristics with those in oceans. Data analysis showed that relative to oceanic channels, freshwater river/lake acoustic channels have larger temporal coherence, higher correlation among densely distributed channel paths, and less sound absorption loss. Additional, channel analyses revealed that under-ice acoustic channels could achieve longer transmission distances than open-water channels, benefited from the SSP-induced surface-ducted sound propagation and possibly low ambient noise levels. Furthermore, with the ice layer being a rigid surface reflector, under-ice channels are more deterministic than open-water channels and have almost

zero Doppler effect when both transmitter and receiver are stationary. Possible impacts on transceiver design were discussed based on the observed characteristics.

Chapter 3 adopts a data-driven perspective and models the temporal evolution of a slowly-varying channel parameter of interest as the summation of a time-invariant component, a time-varying process that can be explicitly represented by available environmental parameters, and a Markov latent process that describes the contribution from unknown or unmeasurable physical mechanisms. An algorithm is developed to recursively estimate the unknown model parameters and predict the channel parameter of interest, based on sequentially collected channel measurements and environmental parameters in real time. We further extend the above model and the recursive algorithm to the channel that exhibits periodic (a.k.a. *seasonal*) dynamics, by introducing a multiplicative seasonal autoregressive process to model the seasonal correlation. The proposed models and algorithms are evaluated via extensive simulations and data sets from two shallow-water experiments. The experimental results reveal that the average channel-gain-to-noise-power ratio, the fast fading statistics, and the average delay spread can be well predicted.

Chapter 4 focuses on the estimation of the most important environment factor to the acoustic channels, the sound speed, jointly with the tracking of an mobile AUV network. The sound speed is modeled to capture the spatial and temporal variations. The analytic results of the propagation delay and its gradient w.r.t. the sound speed

parameters are obtained. Based on the propagation delay between sensor nodes, a Gaussian message passing (GMP)-based method is proposed to recursively estimate the parameters of the time-varying sound speed and the locations of the sensors in a mobile network. The algorithm is extended to sound speed models with spatial and temporal variations. Extensive simulations demonstrates the time-varying inhomogeneous sound speed and the mobile network can be well tracked. Moreover, the improvement of the localization accuracy compared to the algorithm based on the assume straight line propagation is investigated.

Contributions of the thesis are summarized and potential future works are discussed in Chapter 5.

Notation: Bold upper case letters and lower case letters are used to denote matrices and column vectors, respectively. $\mathbf{A}^{\mathrm{T}}$ denotes the transpose of matrix $\mathbf{A}$. $\det(\mathbf{A})$ denotes the determinant of matrix $\mathbf{A}$. $[\mathbf{a}]_m$ denotes the mth element of vector $\mathbf{a}$, and $[\mathbf{A}]_{m,k}$ denotes the (m,k)th element of matrix $\mathbf{A}$. $\mathbb{E}[x]$ denotes the expectation of random variable x. $\mathcal{N}$ denotes a index set.

Chapter 2

Experimental Investigation of

Underwater Acoustic Channels[1]

2.1 Introduction

Underwater acoustic (UWA) channels are often regarded as one of the most challenging medium for wireless communications. Significant progress on UWA channel characterization and communications has been witnessed in the last two decades, whereas most of the effort has been focused on oceanic and open-water environment [16], only very limited research on under-ice acoustic channels is available [17, 18]. Driven by

---

[1]Some contents in this chapter were previously published in *2015 ACM WUWNet Conference, 2017 WUWNet Conference, 2014 IEEE Asilomar Conference, 2018 IEEE CCWC Conference* and *2019 IEEE/OES AUV Workshop*. Refer to Appendix A for granted permission letters

the demand of a wide range of aquatic applications of UWA communications and networking in freshwater rivers/lakes and ice-covered regions, such as water pollution monitoring and disaster prevention [19, 20, 21, 22] and exploitation in polar regions [23], it is imperative to understand the acoustic channels in those environments and to examine suitable communication techniques tailored to the channel characteristics.

The distinction between oceanic acoustic channels and freshwater river/lake acoustic channels could dictate very different transceiver designs. For example, the inter-carrier-interference (ICI) in multicarrier communications incurred by large Doppler spreads in oceanic channels has to be explicitly addressed [24, 25], while the inter-symbol-interference (ISI) in single-carrier communications incurred by dense channel paths in freshwater river/lake channels needs careful consideration [26]. Additionally, different from the open-water environment, the under-ice environment often features a sound speed profile (SSP) that has a positive gradient with respect to water depth. According to Snell's law, such a SSP refracts acoustic rays upward to the ice layer where they are reflected back to water, leading to a surface-ducted sound propagation. Should the receive node be within the surface duct, long-range acoustic communications can be achieved. In addition, relative to the open-water environment where the surface wave serves as a moving reflector, the ice layer is rigid, leading to less variation in the reflected path lengths (hence the Doppler effect) and the path amplitudes.

12
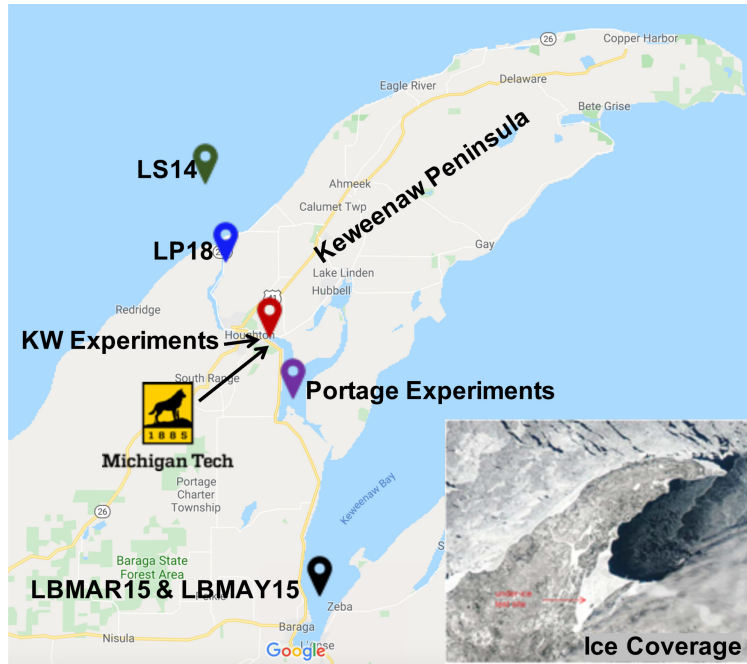
Figure 2.1: Overview of the UWA experiment sites

This Chapter aims to provide some insights on the difference between oceanic acoustic channels and freshwater river/lake acoustic channels, and the difference between open-water and under-ice acoustic channels, based on a series of underwater acoustic communication experiments conducted in the Keweenaw Peninsula area as depicted in Fig. 2.1. The data sets for freshwater river/lake acoustic channel analysis were collected from three types of experiments conducted by our research group with the help of the Great Lakes Research Center (GLRC), including four stationary experiments, two mobile experiments and two under-ice experiments, and the data sets for oceanic channel analysis were collected from one stationary and one mobile experiments conducted by the Woods Hole Oceanographic Institution (WHOI) and held off the coast of Martha's Vineyard, Massachusetts in 2008 and 2010, respectively.

UWA channels are defined by a plethora of environmental parameters, such as water temperature and salinity, surface waves, bottom properties, and geometry of transmitters and receivers. In this Chapter, we consider the characteristics of UWA channels in the following aspects that pertain to communications.

- *Temporal and spatial channel variations* The underwater acoustic channels are easily affected by environment factors, e.g., the wind speed will change the ambient noise level and the temperature of the water will change propagation of the sound speed due to the change of sound speed distribution. Additionally, the distribution of the energy in the water field is usually not uniform. Some areas have more acoustic energy, whereas others known as shadow zone have negligible energy. This unevenly distribution of energy causes spatial variation of acoustic channels. A different type of spatial variations is the channel difference between close links in a network.

- *Multipath characteristics:* The channel multipath characteristics depend on both environment conditions and geometry of transmitters and receivers. Typically, oceanic channels are often sparse with energy concentrated on a few paths and the paths exhibit large Doppler spreads incurred by time-varying surface reflections and/or mobile obstacles [24, 25]. On the other hand, freshwater river/lake channels often have densely distributed paths with smaller Doppler spreads. Despite extensive effort on characterizing various types of oceanic

14

channels, to the authors' best knowledge, there has been limited study on the multipath characteristics in freshwater rivers/lakes [27].

- *Sound propagation loss:* Sound propagation loss in water consists of absorption loss, spreading loss, and scattering loss. The absorption loss in seawater arises from the chemical relaxation (due to boric acid and magnesium sulphate) and absorption by pure water [28, 29]. Intuitively, less sound absorption in freshwater can be expected due to less salty content, whereas there has been very limited experimental study on sound absorption in freshwater rivers or lakes, with sporadic investigations in [30, 31, 32].

2.2 Theoretic Basics

2.2.1 Slowly-varying Channel Parameters

The UWA channel features multiple time-varying sound propagation paths. Denote N_{pa} as a generic representation of the number of paths. The channel impulse response (CIR) at time t is

$$h(t;\tau) = \sum_{p=1}^{N_{\mathrm{pa}}} A_p(t)\delta(\tau - \tau_p(t)), \qquad (2.1)$$

where $A_p(t)$ and $\tau_p(t)$ are the time-varying amplitude and delay of the pth path, respectively.

For an UWA transmission with N_{bl} short blocks, the channel is often assumed block-stationary and could change from one block to another. For the ℓth block in the kth transmission, the CIR can be approximated as

$$h_{k,\ell}(t;\tau) = \sum_{p=1}^{N_{\mathrm{pa},k,\ell}} A_{p,k,\ell}\delta(\tau - (\tau_{p,k,\ell} - a_{p,k,\ell}t)), \tag{2.2}$$

where $N_{\mathrm{pa},k,\ell}$ denotes the number of paths, and for each path, e.g., the pth path, the amplitude is approximated as a constant $A_{p,k,\ell}$, and the delay variation is approximated by a first-order polynomial $(\tau_{p,k,\ell} - a_{p,k,\ell}t)$ with $\tau_{p,k,\ell}$ being the initial delay and $a_{p,k,\ell}$ being the Doppler rate, respectively. Estimation of the path parameters is typically performed in each block based on training symbols. An example of the estimated CIR based on the pilot subcarriers in one OFDM block in the SPACE08 experiment is depicted in Fig. 2.2. In addition, the channel SNR in the ℓth block of the kth transmission can be denoted as

$$\zeta_{k,\ell} := \frac{1}{N_{0,k,\ell}} \sum_{p=1}^{N_{\mathrm{pa},k,\ell}} |A_{p,k,\ell}|^2, \tag{2.3}$$

where $N_{0,k,\ell}$ is the noise power in the ℓth block.

Different from the fast variation of path parameters, the structure of the CIR could

16
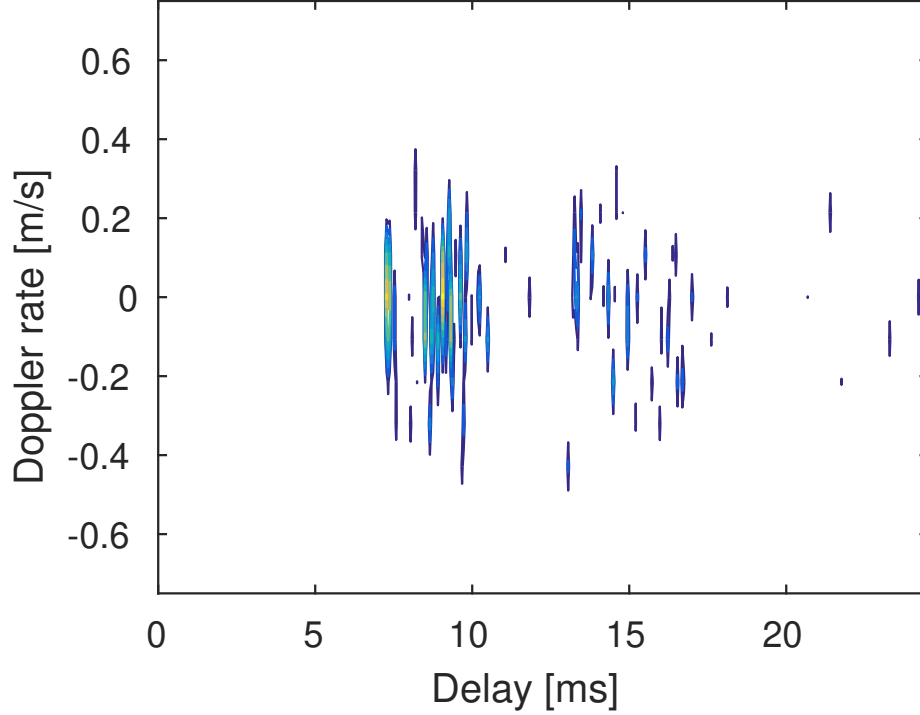
Figure 2.2: An example of the estimated channel impulse response within an OFDM block duration of 129.46 milliseconds in SPACE08.

change slowly from one transmission to another in accordance with environmental conditions. Corresponding to the multiple (N_{bl}) individual CIRs in the kth transmission, several examples of slowly-varying channel parameters are in the following.

- *The average channel SNR* in decibel (dB), defined as

$$\overline{\zeta}_{\mathrm{dB}}[k] := \frac{1}{N_{\mathrm{bl}}} \sum_{\ell=1}^{N_{\mathrm{bl}}} 10 \log_{10}(\zeta_{k,\ell}). \qquad (2.4)$$

- *The fast fading statistics.* Despite the fast variation of path parameters within one transmission, the statistics of the fast variation could change slowly from one transmission to another. In this Chapter, we adopt a Nakagami-m channel

fading model [33], and examine the temporal evolution of the fading parameter m from one transmission to another. For the kth transmission, the fading parameter m can be estimated based on the block SNRs $\{\zeta_{k,1}, \cdots, \zeta_{k,N_{\mathrm{bl}}}\}$ that follow a corresponding Gamma distribution.

- *The average RMS delay spread* that quantifies the channel dispersion in delay [34],

$$\tau_{\mathrm{spread}}[k] := \frac{1}{N_{\mathrm{bl}}} \sum_{\ell=1}^{N_{\mathrm{bl}}} \frac{\sqrt{\sum_{p=1}^{N_{\mathrm{pa},k,\ell}} |A_{p,k,\ell}|^2 (\tau_{p,k,\ell} - \bar{\tau}_{k,\ell})^2}}{\sqrt{\sum_{p=1}^{N_{\mathrm{pa},k,\ell}} |A_{p,k,\ell}|^2}}, \qquad (2.5)$$

with

$$\bar{\tau}_{k,\ell} := \frac{\sum_{p=1}^{N_{\mathrm{pa},k,\ell}} |A_{p,k,\ell}|^2 \tau_{p,k,\ell}}{\sum_{p=1}^{N_{\mathrm{pa},k,\ell}} |A_{p,k,\ell}|^2}. \qquad (2.6)$$

- *The average RMS Doppler spread* that quantifies the channel dispersion in the Doppler rate, denoted by $a_{\mathrm{spread}}[k]$, which can be similarly defined as $\tau_{\mathrm{spread}}[k]$ through replacing $\tau_{p,k,\ell}$ by $a_{p,k,\ell}$ in (2.5) and (2.6).

2.2.2 Multipath Characterization

Denote T as the block length of the waveform, and $\hat{h}(t, \tau)$ as the estimated channel using the least squares (LS) method. Based on the channel estimates of N_{bl} blocks, the channel power delay profile is estimated as [35],

18

$$\hat{P}(\tau) = \int_0^{N_{\text{bl}}T} |\hat{h}(t,\tau)|^2 dt. \tag{2.7}$$

The Doppler spectrum is introduced to characterize the Doppler effect of channel paths,

$$\hat{P}(\nu) = \int_0^{\text{T}} |\hat{S}(\nu,\tau)|^2 d\tau, \tag{2.8}$$

where

$$\hat{S}(\nu,\tau) = \int_0^{N_{\text{bl}}T} \hat{h}(t,\tau) \exp(-2\pi i \nu t) dt. \tag{2.9}$$

The channel auto-correlation function defined as

$$\hat{R}(\Delta t) = \frac{1}{T} \int_0^T \mathbb{E}\left[\hat{h}^*(t,\tau)\hat{h}(t+\Delta t,\tau)\right] d\tau \tag{2.10}$$

is used to characterize the channel temporal coherence property.

The normalized cross covariance is introduced to quantify the correlation of channel taps,

$$\hat{M}(\tau_k,\tau_l) = \frac{\chi(\tau_k,\tau_l)}{\sqrt{\chi(\tau_k,\tau_k)\chi(\tau_l,\tau_l)}}, \tag{2.11}$$

where

19

$$\tilde{h}(t,\tau) = \hat{h}(t,\tau) - \frac{1}{N_{\mathrm{bl}}T}\int_0^{N_{\mathrm{bl}}T}\hat{h}(t,\tau)dt, \tag{2.12}$$

$$\chi(\tau_k,\tau_l) = \left|\int_0^{N_{\mathrm{bl}}T}\tilde{h}^*(t,\tau_k)\tilde{h}(t,\tau_l)dt\right|. \tag{2.13}$$

2.2.3 Sound Propagation Loss

We adopt an empirical model for underwater sound propagation loss over a distance of d,

$$\mathrm{TL}(d) = \beta 10\log_{10}(d) + \alpha(f)d + \xi, \tag{2.14}$$

where the first term corresponds to the spreading loss, the second term corresponds to the frequency-dependent absorption loss, and the last term is a scaling factor related to the scattering loss. In the scenario with an *unknown* gain factor of the automatic gain control (AGC) at the receiver, it is difficult to directly map the recorded signal strength to sound intensity. Therefore, in this Chapter we mainly focus on the relative sound propagation loss corresponding to a reference distance d_0. For a source transmitting at a particular sound level, denote $I(d)$ as the sound intensity after propagating a distance of d. The relative propagation loss in dB can be formulated as

$$\mathrm{TL}_{(d,d_0)} = \mathrm{TL}_d - \mathrm{TL}_{d_0} = 10\log_{10}\frac{I(d_0)}{I(d)}. \tag{2.15}$$

Denote $P(d)$ as the power of the received digital signal after AGC, and $G(d)$ as the unknown AGC factor of the receiver. We have

$$\frac{I(d_0)}{I(d)} = \frac{P(d_0)/G(d_0)}{P(d)/G(d)} = \frac{P(d_0)G(d)}{P(d)G(d_0)}. \tag{2.16}$$

To measure the relative propagation loss, we consider a system with a mobile transmitter and a stationary receiver, and assume that the ambient noise intensity I_{n} at the receiver does not change much within consecutive channel sounding transmissions. Denote $P_{\mathrm{n}}(d)$ as the noise power within the recorded digital signal corresponding to a transmission distance of d. We have

$$\frac{P_{\mathrm{n}}(d_0)}{P_{\mathrm{n}}(d)} = \frac{I_{\mathrm{n}}G(d_0)}{I_{\mathrm{n}}G(d)} = \frac{G(d_0)}{G(d)}. \tag{2.17}$$

Substituting (2.17) into (2.16) yields

$$\frac{I(d_0)}{I(d)} = \frac{P(d_0)/G(d_0)}{P(d)/G(d)} = \frac{P(d_0)P_{\mathrm{n}}(d)}{P(d)P_{\mathrm{n}}(d_0)}, \tag{2.18}$$

which leads to

$$\mathrm{TL}_{(d,d_0)} = 10\log_{10}\frac{P(d_0)P_{\mathrm{n}}(d)}{P(d)P_{\mathrm{n}}(d_0)} = 10\log_{10}\frac{\mathrm{SNR}(d_0)}{\mathrm{SNR}(d)}. \tag{2.19}$$

Hence, the relative propagation loss can be computed based on the received signal-to-noise ratio (SNR) at different distances.

2.3 Stationary Acoustic Channels

2.3.1 Freshwater Lake Channels

Table 2.1
OFDM parameters in field experiments.

Parameters	Lake tests	SPACE08	MACE10
center frequency [kHz]: f_c	17	13	13
bandwidth [kHz]: B	6	9.77	4.883
# of subcarriers: K	1024	1024	1024
symbol duration [ms]: T	170.7	104.86	209.7
frequency spacing [Hz]: $1/T$	5.8594	9.54	4.77
guard interval [ms]: T_g	79.3	24.6	40.3

A stationary experiment (KWAUG14) was conducted in the Keweenaw Waterway adjacent to Michigan Tech's campus from Aug. 27 to 31, 2014 over a range of weather conditions. Two AquaSeNT OFDM modems [36] — one as a transmitter, and the other as a receiver — were deployed on two sides of the waterway with a distance of 312 m; as shown in Fig. 2.3. The water depth was about 3 m. Both modems were at 1.5 m in water. A sequence of channel probing signals followed by 20 OFDM-modulated blocks was transmitted every 15 mins for five consecutive days. Parameter settings of OFDM blocks in this experiment are summarized in Table 2.1.
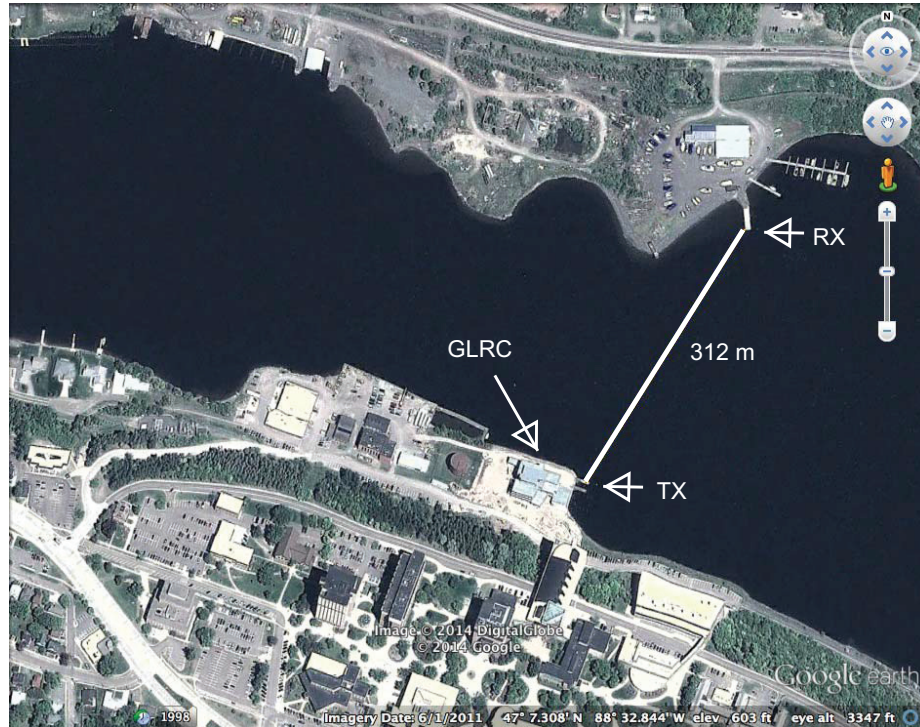
Figure 2.3: KWAUG14 experiment setup.

Fig. 2.4 shows the weather conditions, received SNRs, and false alarms during the experiment. One can observe that (1) the received SNR exhibits a large diurnal pattern — the SNR in night-time transmissions is much higher than that in daytime transmissions, and there are small-scale variations on top of the large-scale variations; the diurnal change in the signal and noise strength could be related to the well-known "afternoon effect" caused by the diurnal and seasonal change in water surface temperature [37], and also the increase of ambient interferences in daytime; (2) as shown in the highlighted area of the received SNR curve, the received SNR has large short-term fluctuations during the rainy condition, and a close examination of the waveforms recorded during the rainy period reveals a considerable amount of impulsive interferences; and (3) the false alarms triggered by ambient interferences
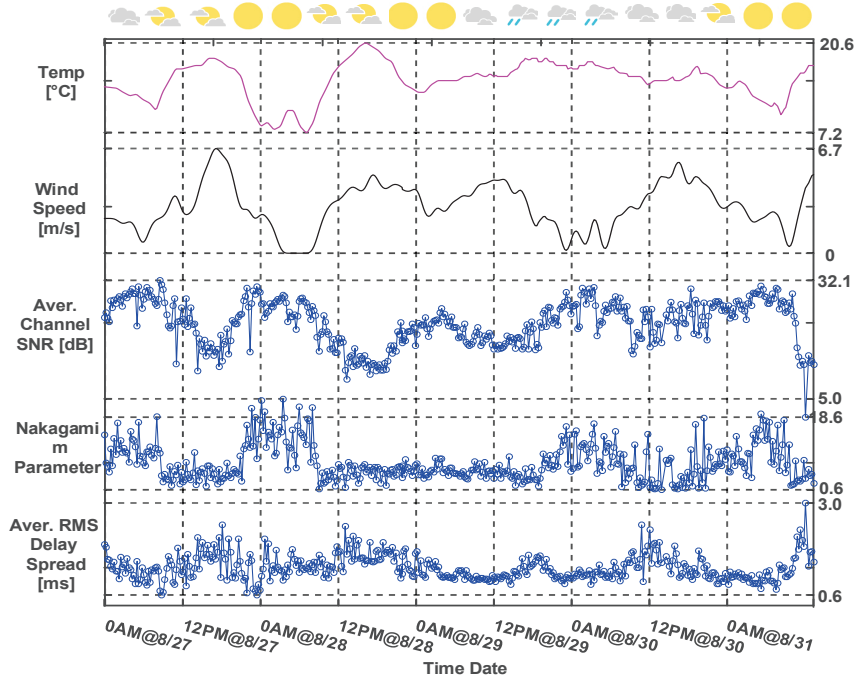
Figure 2.4: KWAUG14: Evolution of several slowly-varying channel parameters. The sequences of the average channel SNR are scaled by corresponding transmission power levels. RMS: root mean square.

appear mainly in the daytime, which might be due to heavy boating activities.

Fig. 2.5 shows the average normalized channel power profile, the average normalized channel auto-correlations, and the representative normalized cross-correlation of channel taps during the early morning and the afternoon transmissions on Aug. 28, where the early morning results are averaged over 24 files recorded from 00:00 am to 5:45 am, and the afternoon results are averaged over 24 files recorded from 1:00 pm to 6:45 pm. One can see that the early morning channel is highly correlated and that the afternoon channel still maintains a high correlation around 0.8. Fig. 2.5 (c) and (d) reveal higher correlation of channel taps in the early morning transmissions.

24
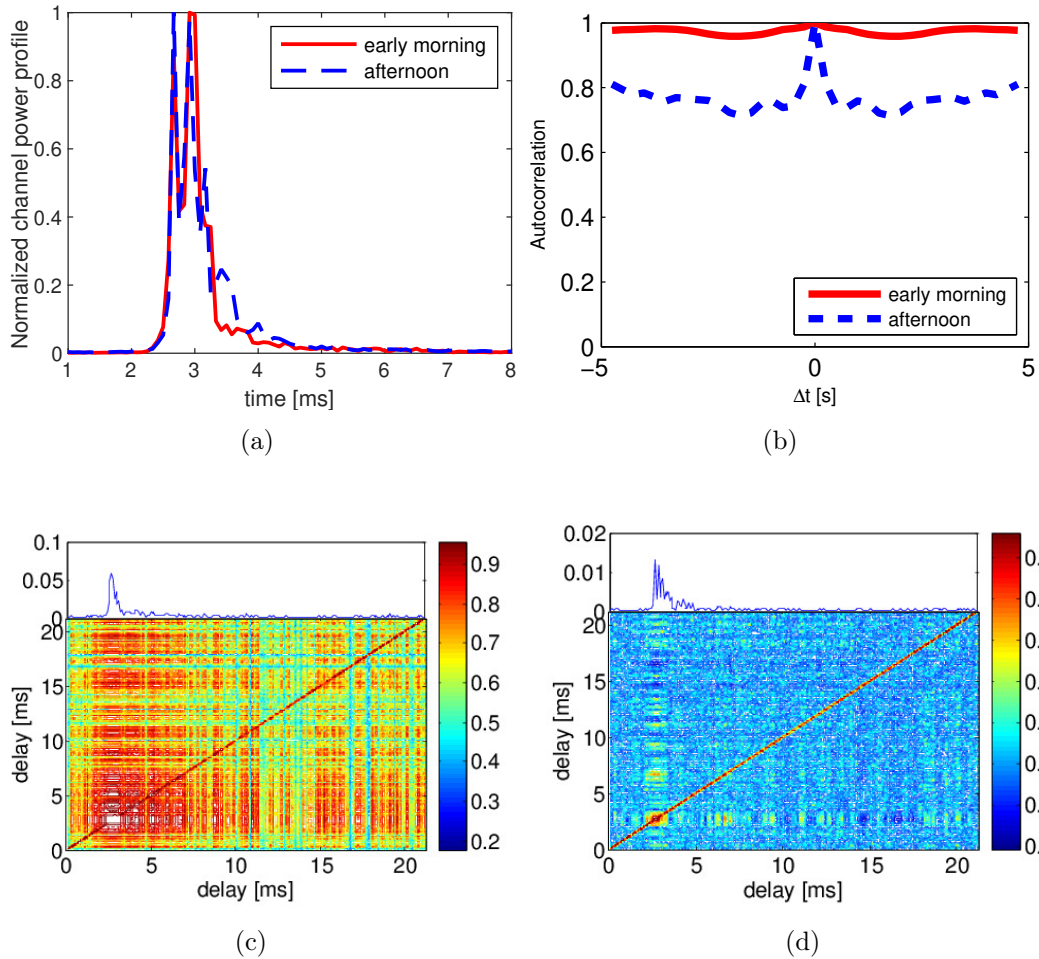
Figure 2.5: KWAUG14: (a) normalized channel power profile; (b) normalized auto-correlation; (c) normalized cross-correlation of channel taps in early morning transmissions; and (d) normalized cross-correlation of channel taps in afternoon transmissions.

2.3.2   Seawater Ocean Channels

We use the data collected from the *surface processes and acoustic communications experiment* (SPACE08) to study the channel characteristics in the oceanic environment [38]. The slowly-varying channel parameters and the weather conditions are depicted
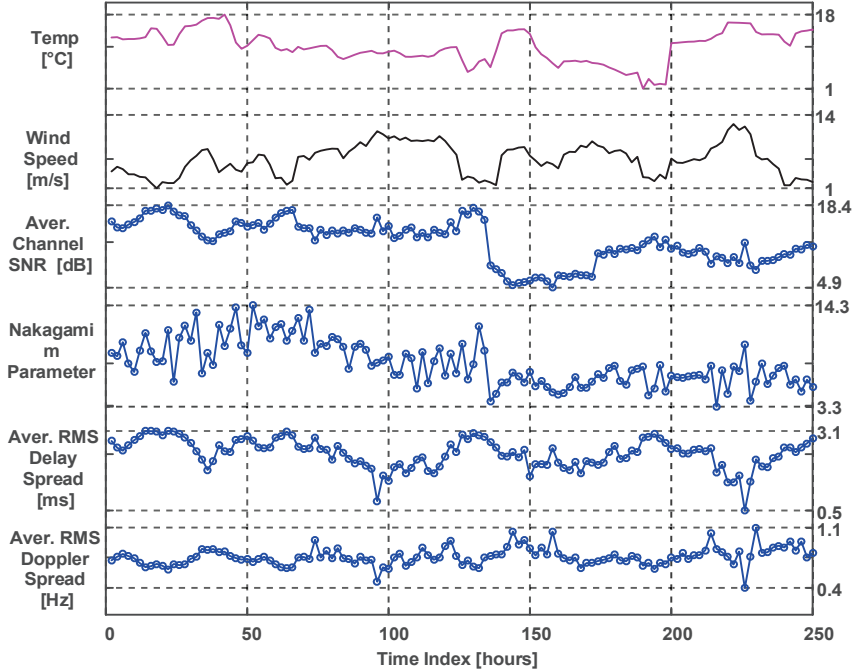
Figure 2.6: SPACE08: Evolution of several slowly-varying channel parameters. The sequences of the average channel SNR are scaled by corresponding transmission power levels. RMS: root mean square.

in Fig. 2.6. The experiment was conducted by the Woods Hole Oceanographic Institution (WHOI), and held off the coast of Martha's Vineyard, Massachusetts, from Oct. 14 to Nov. 1, 2008. The water depth was about 15 m. Among all the six receivers, we only consider the data collected by the receiver labeled as S3 which was 200 m away from the transmitter. There are ten recorded files on each day, and each file consists of 20 OFDM blocks. However, some data files recorded in the afternoon on Julian date 300 were distorted, which are excluded for channel characterization. Parameter settings of this experiment are summarized in Table 2.1.

Fig. 2.7 (a) shows the channel Doppler spectrum averaged over all the recorded files in SPACE08. For comparison, the channel Doppler spectrum in the Portage Lake

26

experiment averaged over all the recorded data files is also plotted. The higher side-lobes of the Doppler spectrum in SPACE08 indicate larger Doppler spreads of channel paths. Fig. 2.7 depicts the normalized auto-correlation of SPACE08 channels. Compared to the lake channels in Figs. 2.5 (b), the sea channel exhibits lower temporal correlations.

Fig. 2.8 illustrates the normalized cross covariance of channel taps averaged over the files recorded on each day. Comparing the result with that in Figs. 2.5, one can see that the channel taps in the lake environment have higher correlation.
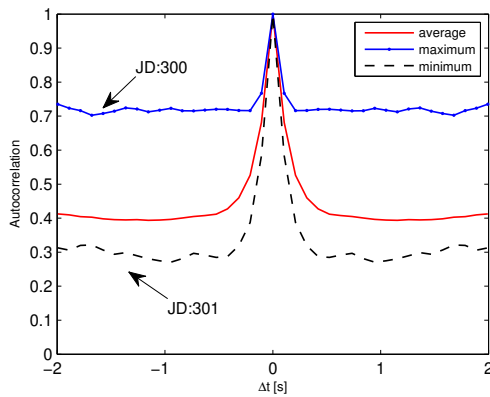
Figure 2.7: SPACE08: The normalized channel auto-correlations.

2.3.3 Spatial-Temporal Variation in UWA Network

A stationary networking experiment (KWST16) was conducted in Keweenaw Waterway in April, 2016. Four OFDM modems were deployed in the river, which is depicted in Fig. 2.9. The four acoustic nodes take turns to transmit while the others listen.
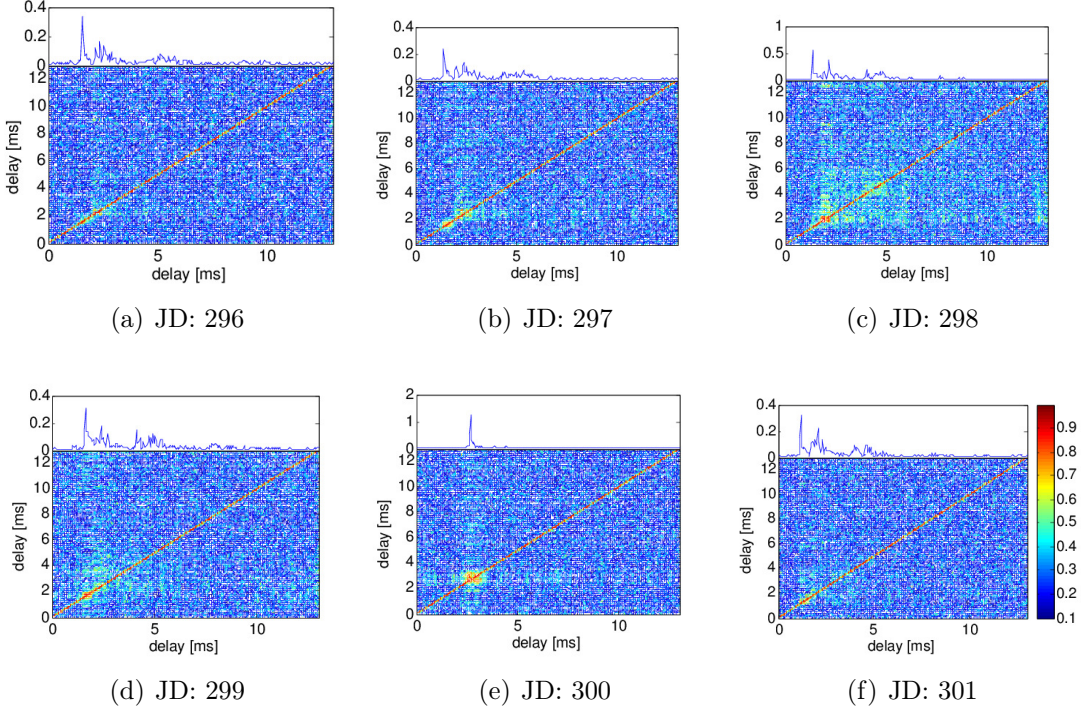
Figure 2.8: SPACE08: Normalized channel cross covariances; JD: Julian date.

In an OFDM modulated waveform, the pilot signal-to-noise ratio (PSNR) can be measured in the frequency domain with the following formula,

$$\text{PSNR} = \frac{\mathbb{E}_{i \in \mathcal{I}_\text{P}}[|y_i|^2] - \mathbb{E}_{i \in \mathcal{I}_\text{N}}[|y_i|^2]}{\mathbb{E}_{i \in \mathcal{I}_\text{N}}[|y_i|^2]}, \tag{2.20}$$

where y_i is the observation on the ith subcarrier, $\mathcal{I}_\text{N}$ and $\mathcal{I}_\text{P}$ are the set of null and pilot subcarriers, respectively.

The PSNRs from two links, their reciprocal links and the wind speed during the experiment are plotted in Fig. 2.10. The temporal variation of the channel is clear. Besides, the reciprocal channels are similar to each other and can be considered

28
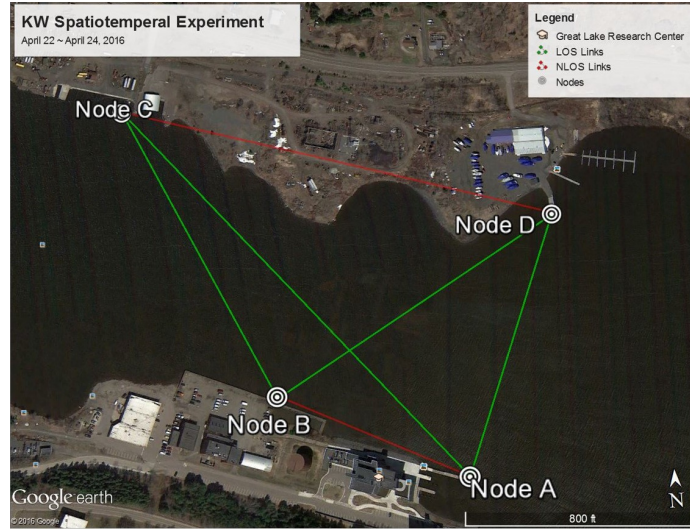
Figure 2.9: KWST16: The spatial-temporal variation experiment setup in Keweenaw Waterway.

symmetric. Moreover, the spatial variations can be observed by comparing different acoustic communication links. On the other hand, the variation pattern are similar in different links and highly correlated with the wind speed. The similarity between different links in the network is illustrated in the covariance matrix plot in Fig. 2.11. It can be observed that the majority of the links have a normalized correlation greater than 0.5. The similarity between different links can be exploited to predict the link states given status of certain observed links.

2.4 Under-Ice Acoustic Channels

The under-ice experiment (LBMAR15) was conducted on March 10, 2015 when the experiment area was fully covered by ice with depth around 0.5 m, and the open-water
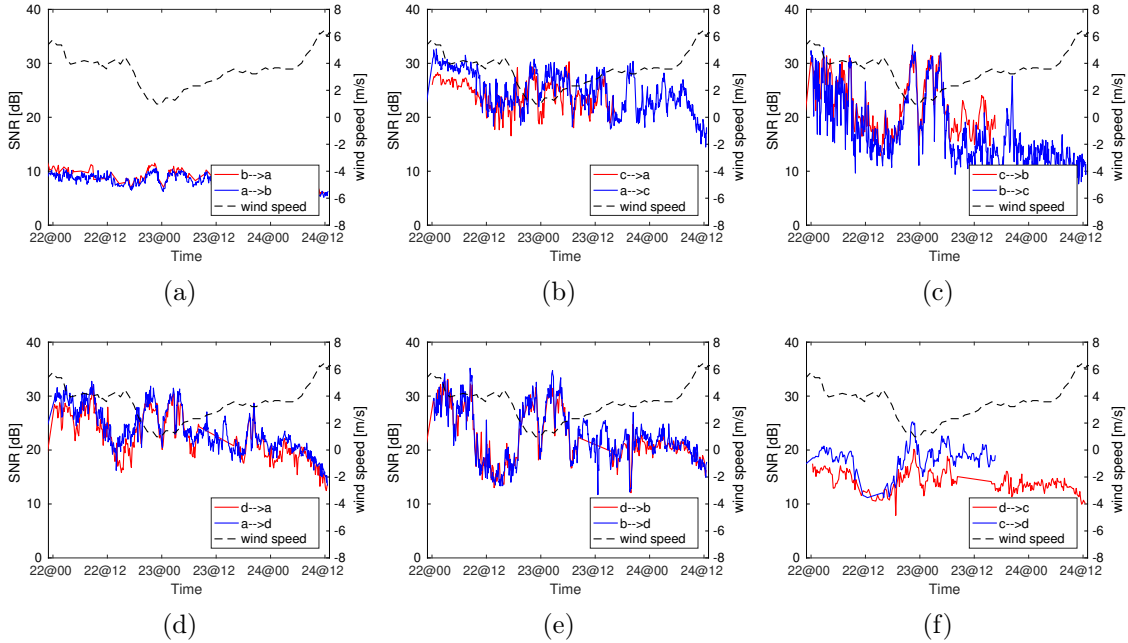
Figure 2.10: KWST16: spatial and temporal variation of the acoustic links. Terminating nodes of the links are indicted in the legends.

experiment (LBMAY15) was conducted on May 14, 2015, within about one month since the ice disappeared. In both experiments, a pair of acoustic modems within the frequency band [14 ∼ 20] kHz were used, one as a source node and the other as a receive node. As illustrated in Fig. 2.12, the receive modem was deployed at a base site, while the transmit modem was deployed sequentially at four different sites in the under-ice experiment, which were about 500 m, 1 km, 2 km and 4 km from the base site, respectively, and at six different sites in the open-water experiment, which were about 450 m, 2 km, 3.9 km, 7.6 km, 11.2 km, 15.1 km away from the base site, respectively. The modems were about 9.5 m in water in the under-ice experiment, and 9 m in water in the open-water experiment. The water depth varies from 55 m to 90 m in the experiment area. The transmitted waveform is modulated by OFDM
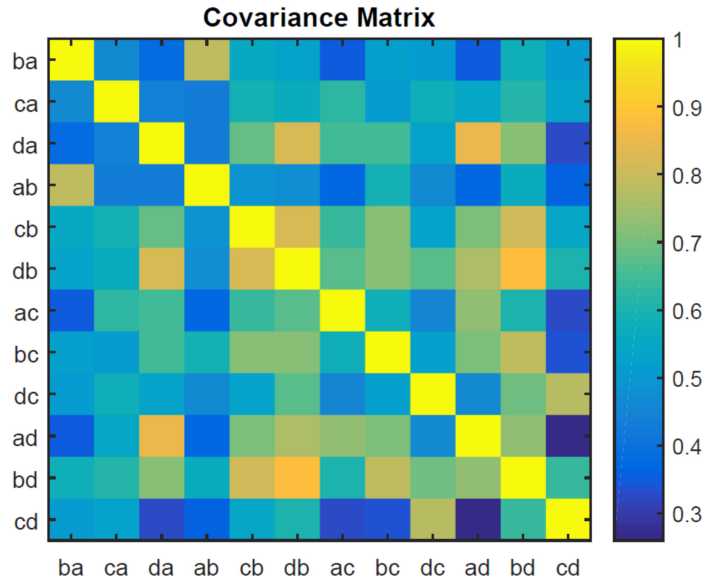
Figure 2.11: KWST16: The covariance of any two acoustic links.

technique.

Due to limited salty content in water, the SSP largely depends on the water temperature profile. The SSP in the under-ice experiment was not measured. The measured SSP in the open-water experiment at different sites is shown in Fig. 2.12, where the SSP with a positive gradient can still be observed in the water further offshore, e.g., at the sites of 2 km and 3.9 km away from the base site.

2.4.1 Transmission Loss

With the maximal modem transmission power of 30 Watts, Fig. 2.13 shows the average SNR and the average PSNR in both experiments. Due to the surface-ducted sound propagation and possibly low ambient noise level in the under-ice environment, the
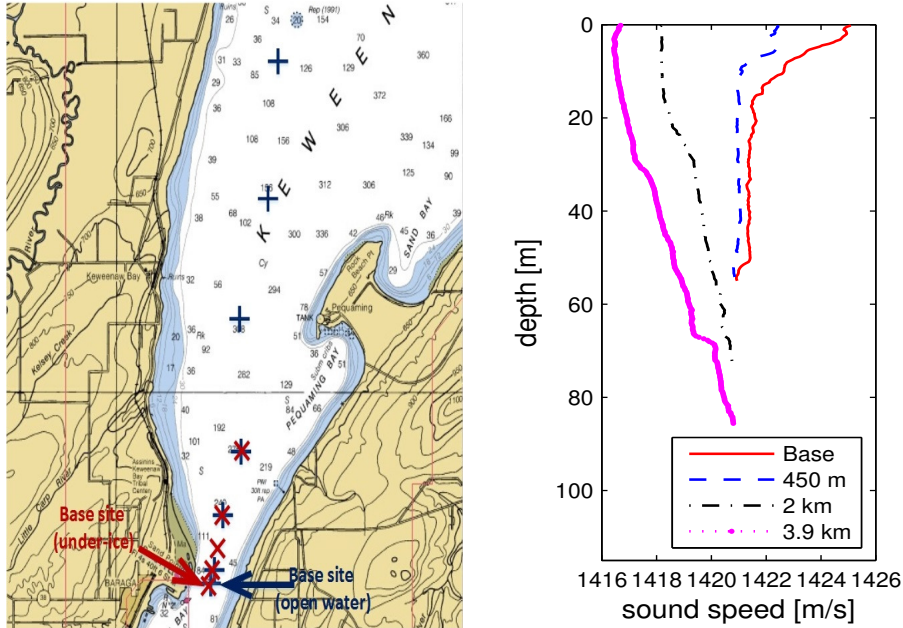
Figure 2.12: LBMAR15 and LBMAY15: Experimental setup at L'Anse Bay (Left). "x": under-ice test sites; "+": open-water test sits. SSPs in the open-water experiment (Right).

under-ice channel enjoys higher receive SNRs than the open-water channel, and the difference between the two types of channels is pronounced in PSNRs, indicating more severe intercarrier interference hence larger Doppler effect in the open-water channel.

2.4.2 Multipath Channel Characteristics

The evolution of channel impulse responses in both experiments are illustrated in Fig. 2.14, which shows that the under-ice channel is more stable than the open-water channel. Particularly for the channels at a transmission distance around 500 m, the magnitude histogram of the largest channel tap (the tap corresponding to the direct
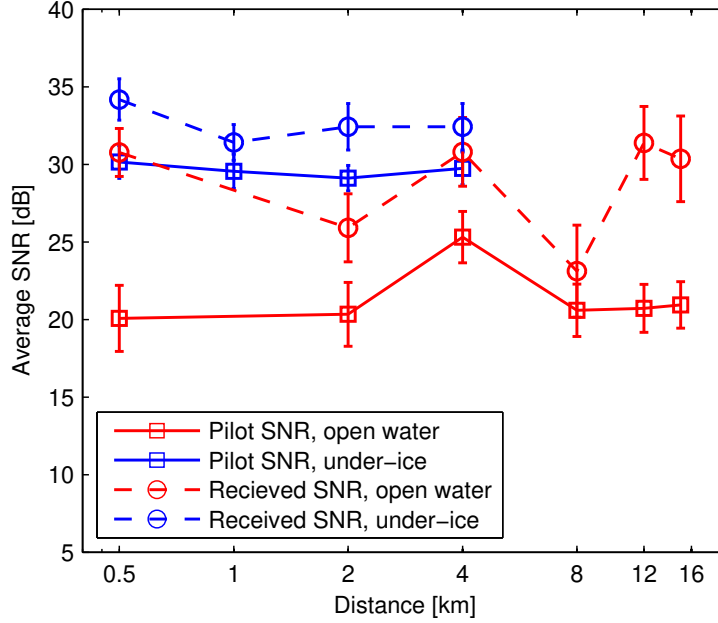
Figure 2.13: LBMAR15 and LBMAY15: The average and standard deviation of SNRs at different transmission distances.

path) normalized by the noise standard deviation is shown in Fig. 2.15, along with the Rician fitting curves with a K-factor of 26.4 and 4.46 in the under-ice experiment and the open-water experiment, respectively. The large difference in the K-factors reveals that the under-ice channel is more deterministic than the open-water channel. Using compressed sensing techniques, the Doppler scale factor of each individual path can be estimated. Corresponding to the channels at the distances of 500 m and 2 km, all the paths in the under-ice environment have zero Doppler rate, while the open-water channel suffers Doppler spreads at different levels, as depicted in Fig. 2.17. This can also be observed from the scattering plots as shown in Fig. 2.16. Similar observations can be obtained for the two types of channels at other transmission distances.
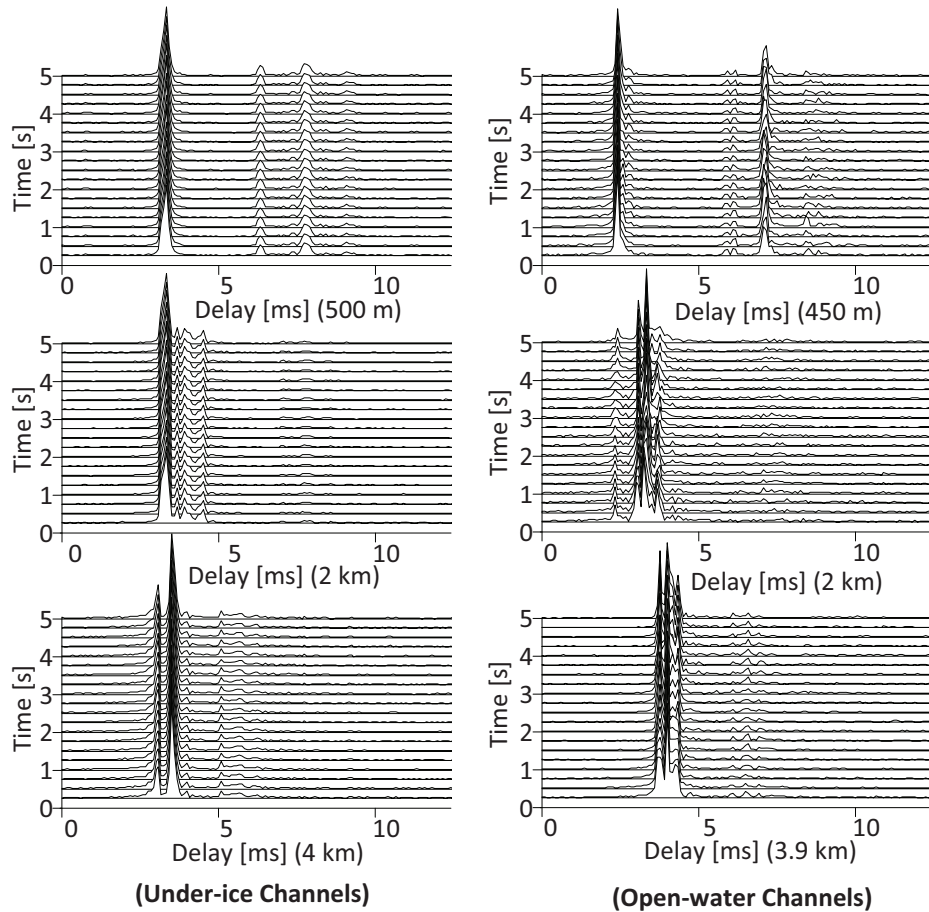
Figure 2.14: LBMAR15 and LBMAY15: Evolution of channel impulse responses.

2.4.3 Spatial Variations and Impulsive Noises

On March 17, 2017, an under-ice experiment was conducted in Portage Lake, MI. The experimental setup is shown in Fig. 2.18. During the experiment, the Portage Lake was covered by about 40 cm thick ice. The water depth in the area varies from 8.3 to 11.3 meters. Three transceivers are installed at the three locations highlighted in Fig. 2.18. Each transceiver will take turn to act as transmitters while the rest act
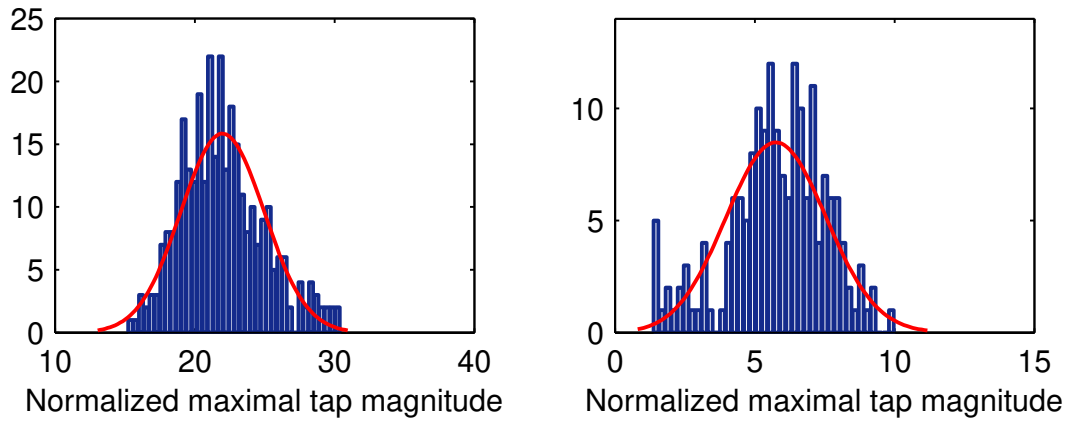
Figure 2.15: Histogram and Rician fitting of the normalized maximal channel tap magnitude at the test site about 500 m. Left: under ice, $K = 26.4$ in Rician fitting; right: open water, $K = 4.46$ in Rician fitting.

as receivers.

In this experiment, the recorded acoustic channels are stable and exhibits negligible Doppler effect as in other under-ice experiments. However, impulsive noises can be frequently observed in the recorded waveforms. An example of the recorded signal contaminated with impulsive noise at the receiver is depicted in Fig. 2.19.

During the experiment, we change the depths of both the transmitter and the receiver. Figs. 2.20 show that even at the same location, channel quality and the received SNRs change significantly mainly due to the shadowing effect caused by the structure of the sound speed.

(a) under-ice, 0.5 km

(b) open water, 0.5 km

(c) under-ice, 2 km

(d) open water, 2 km
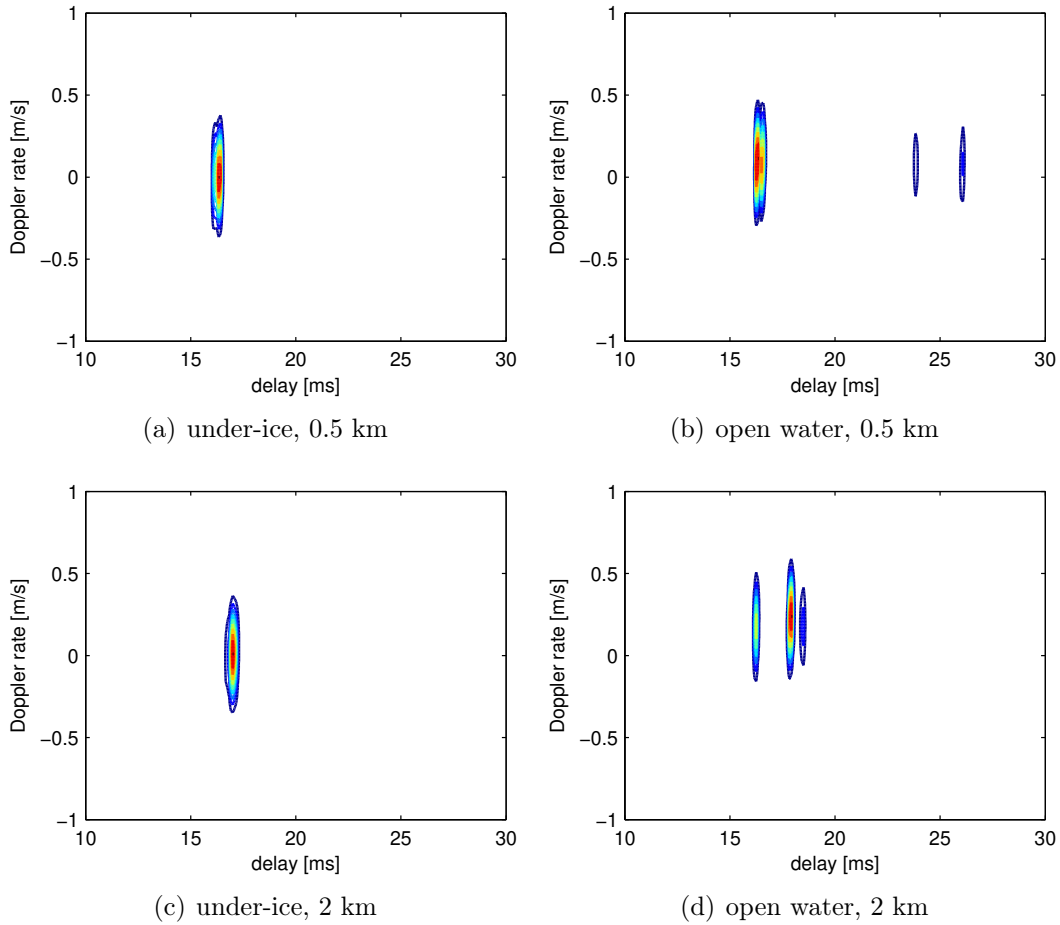
Figure 2.16: LBMAR15 and LBMAY15: Scattering function generated using m-sequence

2.5 Mobile Acoustic Channels

2.5.1 Transmission Loss

In this section, we study the relative sound propagation loss in two mobile experiments: one was held in the Lake Superior and the other was held off the coast of
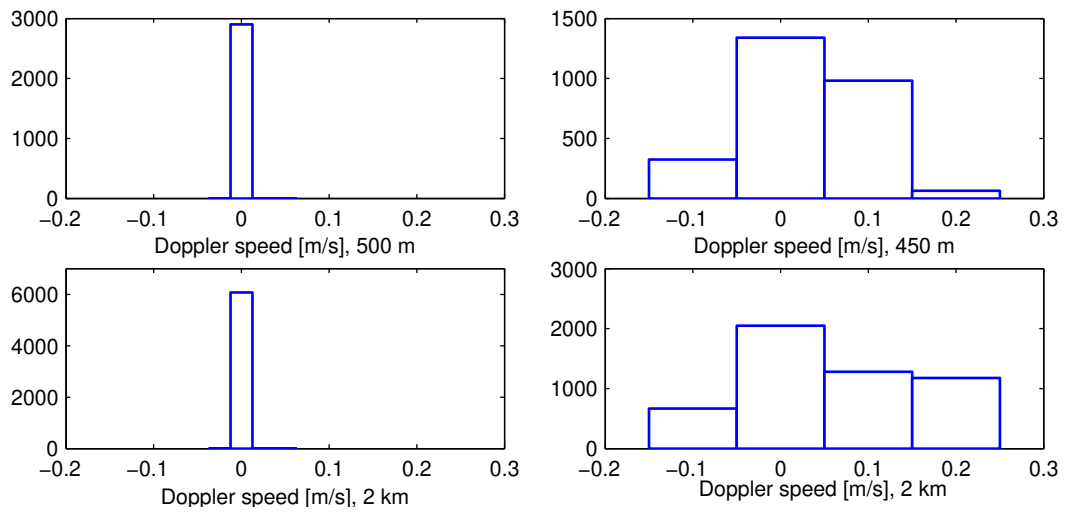
Figure 2.17: LBMAR15 and LBMAY15: Histogram of Doppler speeds of channel paths. Left: under ice; right: open water.
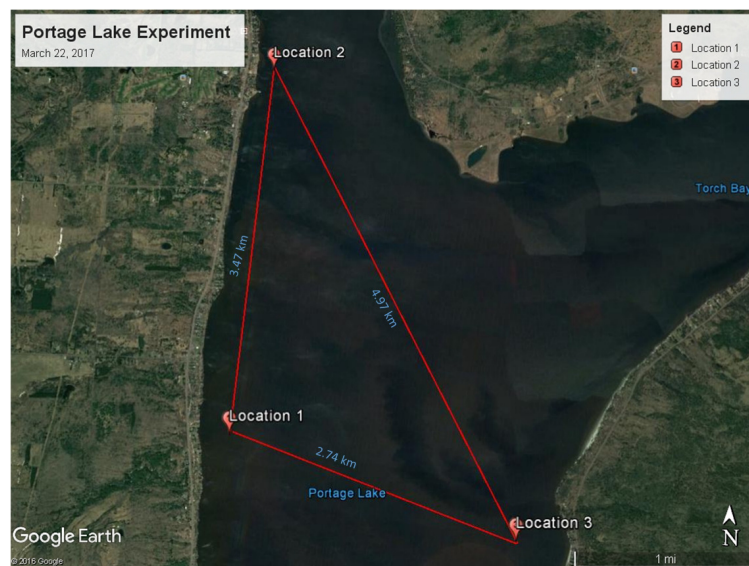
Figure 2.18: Setup of the Portage-MAR17 experiment.

Martha's Vineyard, Massachusetts.

The Lake Superior experiment abbreviated as LS14 was conducted in the Lake Superior near the north entry of the Keweenaw Waterway on Aug. 13, 2014. The receiver
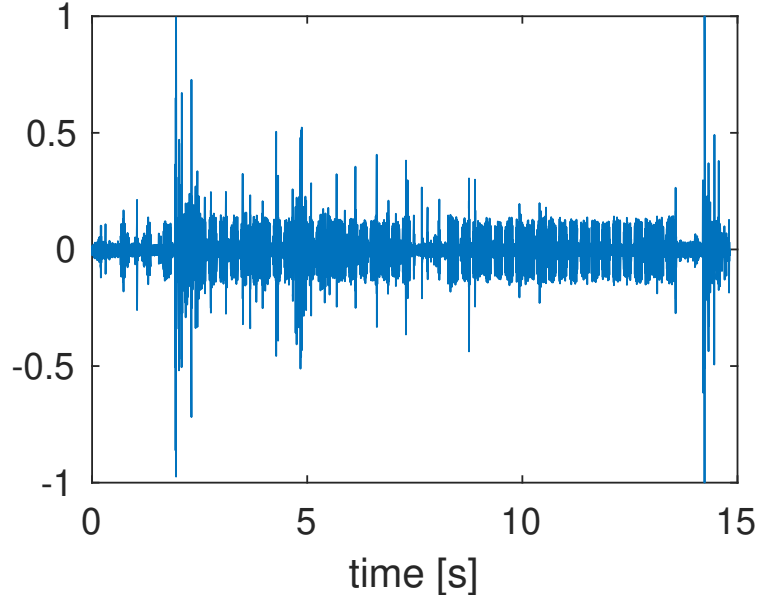
Figure 2.19: Portage-MAR17: A waveform contaminated with ice-cracking impulsive noise. The transmitter at Location 1 and the receiver at Location 2 are both 4.5 meters below the surface.The distance between Location 1 and Location 2 is 3.47 km.

(a) TX @ Location 1 @ 4.5 m

(b) RX @ Location 2
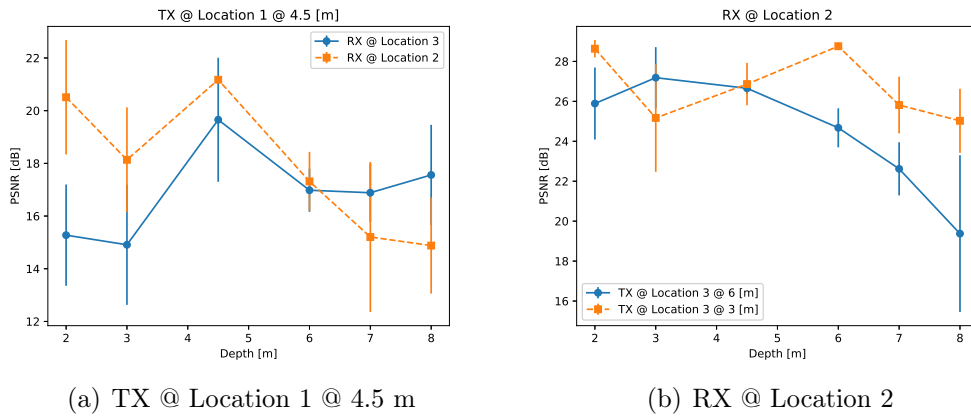
Figure 2.20: Portage-MAR17: The received SNR measurements at different depths.

was fixed on a surface buoy while the transmitter was towed towards the receiver from 750 m to 20 m at a speed around 0.86 m/s. During the towing process, the transmitter kept transmitting a channel sounding waveform that is identical to the waveform

38

used in the Keweenaw Waterway experiment and the Portage Lake experiment. In total 34 waveforms were recorded by the receiver.

The *mobile acoustic communication experiment* (MACE10) is a mobile experiment conducted in ocean environment [38]. The experiment was carried out by Mr. Lee Freitag and his team from the WHOI, off the coast of Martha's Vineyard, Massachusetts, in June, 2010. The water depth was about 95 to 100 meters. The receiver array was stationary, while the source was towed slowly away from the receiver from 500 m to 4.5 km and then towed back, at a speed around 1 m/s. Out of two tows in the experiment, we only consider the data set collected in the first tow with 31 transmissions in total and 20 OFDM blocks in each transmission. We exclude one file recorded during the turn of the source, where the received SNR is quite low. Parameters of this experiment are summarized in Table 2.1.

(a) Lake Superior experiment   (b) MACE10
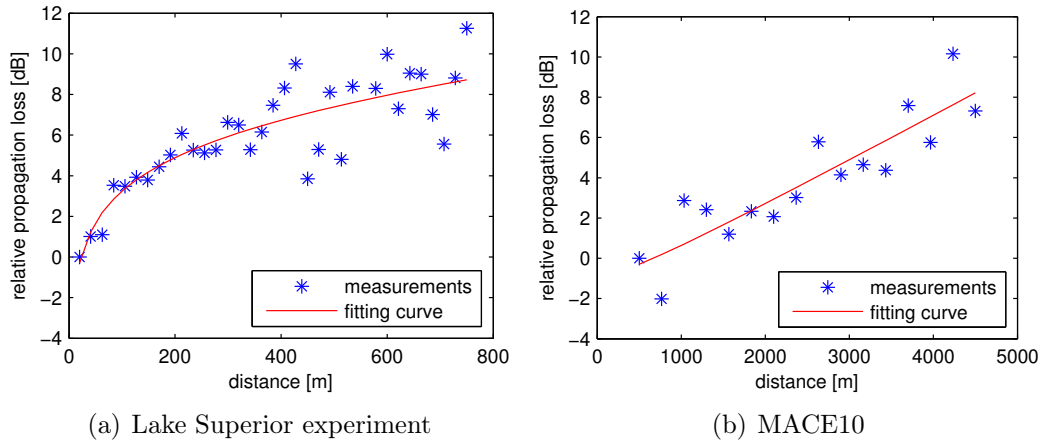
Figure 2.21: Relative propagation loss and curve fitting.

Taking a reference distance of 20 m in the Lake Superior experiment and of 500 m

39

in MACE10, Fig. 2.21 depicts the relative propagation loss computed based on the received SNRs in the two experiments (c.f. (2.19)) and the curve fitting results corresponding to the empirical propagation loss in (2.14). The estimated absorption coefficient $\alpha(f)$ during the curve fitting is 1.9 dB/km and 2.3 dB/km in the Lake Superior experiment and MACE10, respectively. The curve fitting results reveal that as the transmission distance increases, the propagation loss increases logarithmically in the Lake Superior experiment and linearly in MACE10, and the estimated absorption coefficients indicates less sound absorption loss in the Lake Superior experiment than in MACE10 due to less salty content in the lake water.

2.5.2   Doppler Effect and Mobile Channel Characteristics

Another mobile experiment (LP18) is conducted in Lily Pond, located just off of Lake Superior near Houghton, Michigan in October, 2018. The experiment consisted of four static nodes and a mobile node. As illustrated in Fig. 2.22, the four static nodes were anchored at locations A, B, E and F. The mobile node was towed by a human-operated boat at an average speed of around 1 m/s and traveled back-and-forth between Site A and Site B. The water depth of the experiment area is around 8 meters, and the distance between Site A and Site B is 765 meters. During the towing process, the mobile node transmitted a 4-second long communication waveform every 15 seconds at a power level of 0.3 Watts. The four static nodes served as receivers.
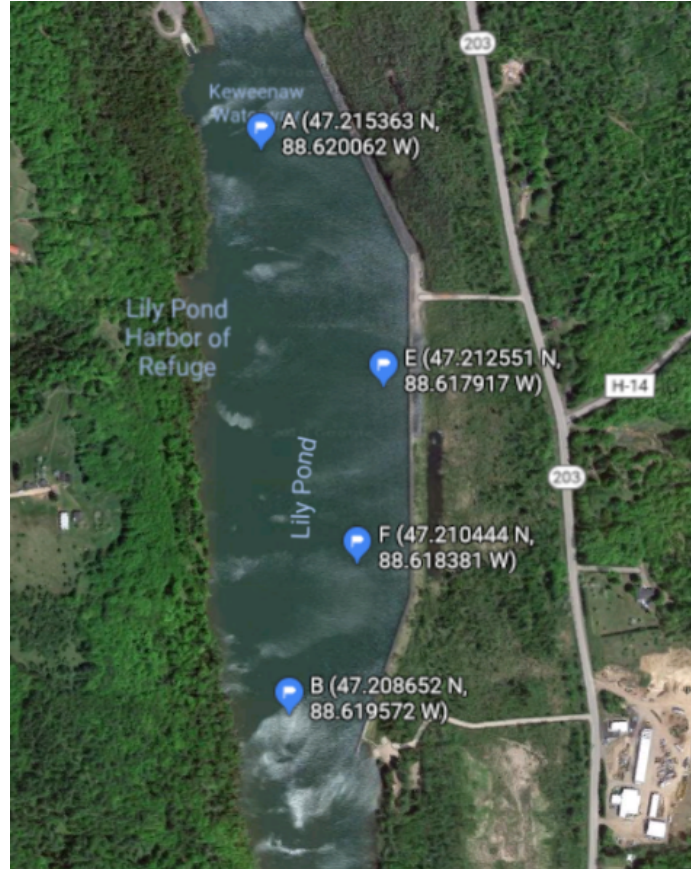
Figure 2.22: LP18: Deployment locations for Lily Pond test on satellite map.

The communication waveform has a carrier frequency of 24 kHz with a bandwidth of 6 kHz. Besides the preamble and postamble, the waveform consists of a single transmission data block modulated by the OFDM technique [39] and a rate-1/2 non-binary low-density parity-check (LDPC) code with an overall transmission rate of 2,688 bits/second. To reveal the insights of UWA mobile communications, we focus on the received waveforms at Node E when the mobile transmitter travels from Site A to Site B, and present some of the processed results.

41
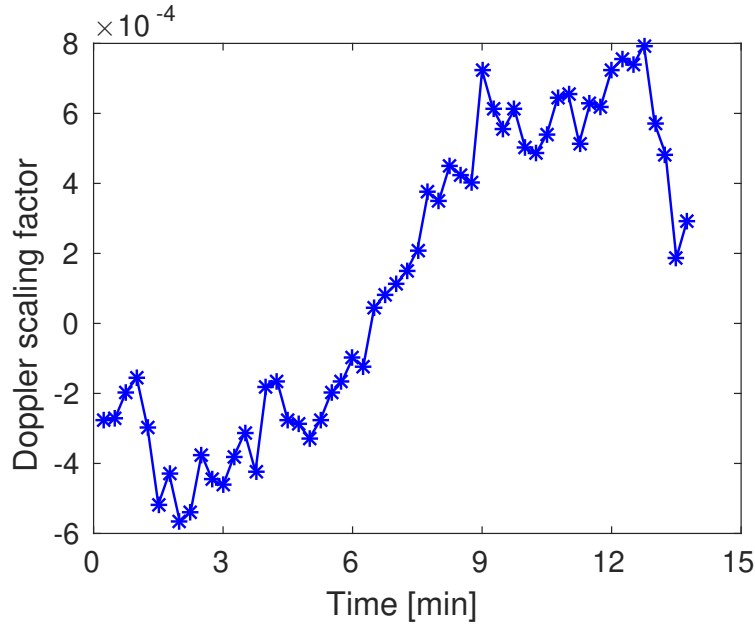
Figure 2.23: LP18: The estimated Doppler scaling factor at Node E as the transmitter moves from Site A to Site B.

Due to the low sound speed in water, the movement of the transmitter causes compression or dilation of the communication waveform. Such a Doppler effect needs to be carefully considered while processing the received data. The Doppler scaling factor a is computed as $a = v/c$, where v is the transmitter node's moving speed with respect to Node E, and $c \approx 1,450$ m/s is the sound speed in water. In this experiment, the estimated Doppler scaling factor based on the received waveforms at Node E is shown in Fig. 2.23. One can observe the change of the Doppler scaling factor when the transmitting modem gets near to Node E and then moves away from it.

For each acoustic transmission, the UWA channel impulse response (i.e., the multipath information) can be estimated via a least squares approach [39]. The evolution of the
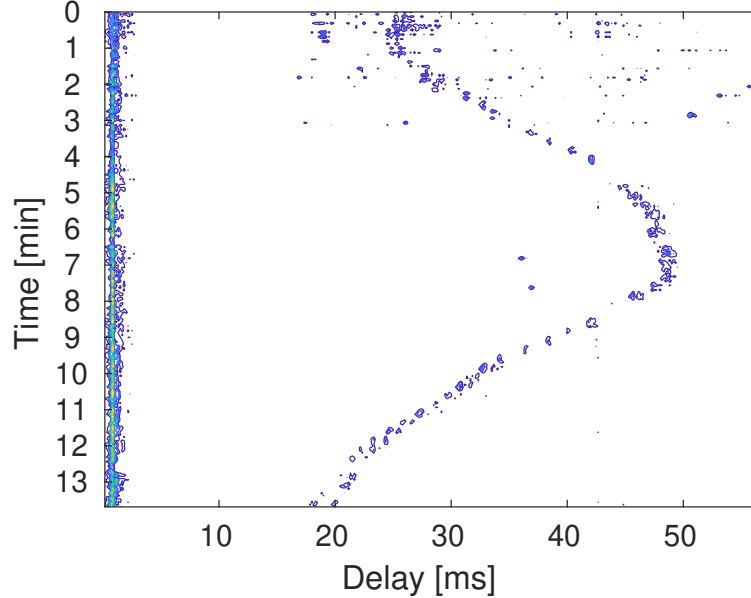
Figure 2.24: LP18: The estimated UWA channel at Node E as the transmitter moves from Site A to Site B. A horizontal slice represents the channel impulse response, where the magnitude is color coded.

UWA channel estimation as the transmitter node moves from Site A to Site B is plotted in Fig. 2.24. One can observe an interesting change of the channel multipath structure (especially the latter arrivals) at Node E.

2.6   Discussions on Transceiver Designs

The differences between freshwater river/lake channels and oceanic channels, under-ice and open-water channels dictate different transceiver designs [4]. Specifically, in the freshwater river/lake environment, the large correlation of channel taps can be exploited to reduce the dimensionality of unknowns in channel estimation, and the large channel temporal coherence can be leveraged for efficient channel tracking.

On the contrary, despite large temporal dynamics of oceanic channels, the sparsity of channel paths can be utilized to improve channel estimation accuracy via compressed sensing techniques [40]. Moreover, consider that the sound absorption loss is frequency-dependent. The low sound absorption loss in freshwater promises a large transmission distance of high-frequency signal (e.g., ~ 100 kHz), hence allows high-frequency transceiver design with a large bandwidth.

Channel analyses revealed that under-ice acoustic channels could achieve longer transmission distances than open-water channels, benefited from the SSP-induced surface-ducted sound propagation. Furthermore, with the ice layer being a rigid surface reflector, under-ice channels are more deterministic than open-water channels and have almost zero Doppler effect when both transmitter and receiver are stationary. Additionally, the ice-cracking impulsive noise should be taken into consideration in the transceiver design. Specifically, impulsive noise mitigation methods should be adopted to enhance the communication performance. For example, an analog nonlinear preprocessor can be used to mitigate the signal outliers [3].

Lastly, awareness should be brought to designers that the depth of the transmitter and receiver will affect the communication quality significantly. And potential research opportunities of mobile channel modeling could arise from the observed evolution of the mobile channel multipath structure.

Chapter 3

Online Modeling and Prediction of the Large-Scale Temporal Variation in UWA Communication Channels[1]

3.1 Introduction

Underwater acoustic (UWA) channels exhibit large temporal dynamics. Influenced by environmental conditions, such as water-air interface characteristics, the sound speed profile and the distribution of ambient acoustic sources, the impulse response

---

[1]The work in this chapter was published in "*IEEE Access*" ©2018 IEEE. Some contents in the chapter were also published in *2016 IEEE Oceans Conference*. Refer to Appendix A for granted permission letters

of an UWA channel could fluctuate on various time scales: seasonal, diurnal, tidal cycles, minutes in the presence of internal waves, and seconds with ocean swells [35, 41, 42]. Extensive research has been devoted to the statistical modeling and countermeasures of fast channel variation within a transmission that consists of one or multiple packets [43, 44, 45]. The study on the large-scale channel variation, namely, the temporal evolution of slowly-varying channel parameters over a long term, e.g., hours, days, months, or years), has been very limited. Examples of those slowly-varying parameters include the locally-averaged channel parameters within a transmission, such as the average channel-gain-to-noise-power ratio (also referred to as *channel SNR*), the average delay spread, the average Doppler spread, and the statistics of fast channel variations. Compared to the fast channel variation, the large-scale channel variation can be attributed to the large-scale change of environmental conditions [45], hence holds a great potential of being predictable.

In this Chapter, we develop a *data-driven* approach for online modeling and prediction of slowly-varying channel parameters in the real-time UWA communication system by exploiting their correlation with water environmental conditions. Prediction of those parameters will allow *proactive adaptation* of higher-level transmission strategies to the channel dynamics. In the sequel, we will first briefly describe our observations on the large-scale channel variation in two field experiments, and then summarize existing approaches to modeling the large-scale channel variation. An overview of this Chapter is presented in the end of this section.
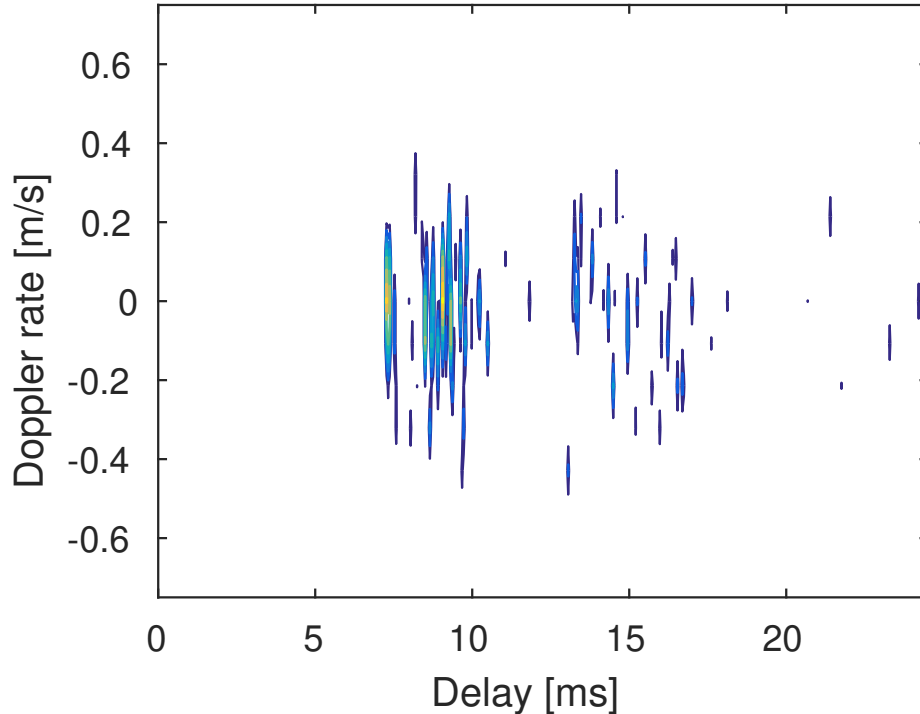
Figure 3.1: An example of the estimated channel impulse response within an OFDM block duration of 129.46 milliseconds in SPACE08. The example is the same as Fig. 2.2.

3.1.1 Observation of the Large-scale Channel Variation in Field Experiments

We introduce the results from two field experiments to illustrate the large-scale channel dynamics. The SPACE08 experiment was conducted in an oceanic environment where a waveform of 1 minute and within the frequency band $[8, 18]$ kHz was transmitted every 2 hours to a receiver which is 200 meters away. The waveform consists of 60 short blocks, and each block is modulated by the ZP-OFDM technique and has

a duration of 129.46 ms. Fig. 3.1 provides an example of the channel impulse response (CIR) which is estimated based on the received waveform of one OFDM block during a transmission. The KW-AUG14 experiment was conducted in the Keweenaw Waterway near Michigan Tech, August 2014 where a waveform of 8.83 seconds and within the frequency band $[14, 20]$ kHz was transmitted every 15 minutes to a receiver which is 312 meters away. The waveform consists of 20 ZP OFDM-modulated blocks, and each of duration 250 ms. Detailed descriptions of the two experiments can be found in Section 3.7. For each experiment, the CIR can be estimated based on each received OFDM block, and the estimated CIRs within each transmission can be used to calculate the locally-averaged channel parameters of the transmission; rigorous descriptions can be found in Section 2.2.1. In Figs. 2.4 and 2.6, we plot the evolution of several locally-averaged channel parameters throughout all transmissions in the two field experiments. For both experiments, one can observe that the average channel SNR is correlated with both the wind speed and the temperature. The Nakagami-m fading parameter in KW-AUG14 exhibits negative correlation with the wind speed and the temperature, while the correlation is not obvious in SPACE08. The average root mean square (RMS) delay spread is correlated with the wind speed negatively in SPACE08 while positively in KW-AUG14. Moreover, a diurnal pattern of the slowly-varying channel parameters can be observed in KW-AUG14. Correlations between UWA channel parameters and water environmental conditions have also been revealed in other field experiments; see, e.g., [41, 42, 46, 47, 48]. In this Chapter, following

the terminology in time series analysis, *we refer to the UWA channels with periodic dynamics (e.g., diurnal or monthly) as seasonal channels [49], where the "seasonal cycle" does not necessarily correspond to the seasons in an astronomical year.*

3.1.2 Existing Methods for Modeling the Large-scale UWA Channel Variation

Existing methods for UWA channel modeling can be grouped into three categories: the wave propagation theory-based modeling, empirical channel modeling and statistical channel modeling. Compared to the latter two approaches, the wave propagation theory-based model [50] yields the highest accuracy. However, it is a deterministic method for a fixed geometry and environmental description, hence cannot accommodate random environmental dynamics.

Using measurements in various water settings, marine engineers have built empirical models that relate the transmission loss and the ambient noise level with water environmental parameters, such as water temperature, salinity, pH, surface wind speed, rainfall rate, and sea state; see, e.g., [15, 51, 52, 53]. Consider that the acoustic propagation property and the ambient acoustic environment are site-dependent. The empirical model parameters are often computed via curve fitting based on field measurements.

In addition, statistical methods have been widely used to characterize the statistical distribution of the signal transmission loss along each path or an equivalent power loss after combining the signals propagating along multiple paths. Compared to the characterization of channel fast fading [27, 45, 54], studies on the modeling of the large-scale channel variation have been very limited. Based on field measurements, a lognormal distribution of the locally-averaged transmission loss was proposed in [45, 55], and the possibility of modeling the temporal evolution of the locally-averaged transmission loss as a first-order autoregressive (AR) process was discussed in [56].

It is worth noting that existing channel modeling methods mainly work in an offline manner. They are used either to evaluate the channel conditions before the system deployment, or to characterize the channel behaviors based on field measurements after the system is recovered.

3.1.3 Our Work

The goal of this Chapter is to develop a method for online modeling and prediction of the large-scale channel variation *during* the system deployment based on sequentially collected channel measurements and water environmental parameters. To this end, a *data-driven* perspective is adopted to exploit the inherent correlation of the large-scale channel variation and its correlation with water environmental conditions.

Specifically, for a slowly-varying channel parameter of interest, we model its temporal evolution as the summation of (i) a time-invariant component, (ii) a time-varying process that can be explicitly represented by available water environmental parameters, and (iii) a hidden Markov latent process which accounts for the contribution from unknown or unmeasurable physical mechanisms. After casting the evolution model into a state-space representation, and following the maximum likelihood (ML) principle and the expectation-maximization (EM) algorithm [57], a low-complexity algorithm is developed to *recursively* estimate the unknown model parameters based on sequentially obtained channel measurements and environmental parameters during the system operation, which then allows to predict the slowly-varying channel parameter in the near future. The proposed modeling method and the recursive algorithm are further extended to seasonal channels, where *a multiplicative seasonal AR process* [49] is introduced to model the seasonal correlation.

The effectiveness of the proposed models and recursive algorithms are evaluated via simulations and data sets from two shallow-water experiments, the SPACE08 and the KW-AUG14. The slowly-varying channel parameters that are examined using the experimental data sets include the average channel SNR, the fast fading statistics, the average RMS delay spread, and the average RMS Doppler spread. The results reveal that superior modeling and prediction performance can be achieved by exploiting the correlation between the large-scale channel variation and water environmental parameters as well as the seasonal correlation in seasonal channels.

Remark 1. The developed algorithms can be applied to real-time operating UWA communication systems. Specifically, the model parameters can be updated recursively in time step-by-step based on newly obtained channel measurements during recent acoustic transmissions as well as newly obtained environmental parameters[2]. The updated model allows the prediction of the large-scale channel variation based on the forecast of environmental conditions. The prediction could guide higher-level proactive adaptation of future transmission strategies, such as the transmission schedule, the transmission power and rate, and the modulation scheme [58]. It has been shown in an early study [59] that even with moderate channel prediction performance, proactive adaptation of the transmission schedule improves energy efficiency more than 20% than a benchmark method that transmits each packet upon its arrival with minimal transmission power that meets a predetermined SNR threshold.

The rest of the chapter is organized as follows. The data-driven modeling method is presented in Section 3.2. A recursive algorithm for the model parameter estimation is developed in Section 3.3. Extension of the proposed model and the recursive algorithm to seasonal channels is presented in Section 3.4. The model order selection for practical UWA channels is discussed in Section 3.5. Simulations and experimental data processing results are presented in Sections 3.6 and 3.7, respectively. Conclusions are drawn in Section 3.8.

---

[2]The environmental parameters can be collected by sensors equipped on the communication nodes (e.g., surface buoys and underwater nodes), or sent from a remote control center to surface buoys via radio-frequency links.

3.2 A Data-driven Method for Modeling Large-scale Channel Variations

In this section, we will develop a data-driven method to model the temporal evolution of a slowly-varying channel parameter of interest. Estimation of the model parameters will be pursued in Sections III and IV.

3.2.1 A Data-driven Model for Slowly-varying Channel Parameters

Consider the temporal evolution of a slowly-varying channel parameter of interest, which is represented by process $\{\alpha[k]\}$, with k being an integer time index. We model the process $\{\alpha[k]\}$ as the summation of a time-invariant component γ_0, a time-varying process $\{g[k]\}$ that can be explicitly represented by available and relevant water environmental parameters, and a latent process $\{x[k]\}$ that describes the contribution from unknown or unmeasurable physical mechanisms, namely,

$$\alpha[k] = \gamma_0 + g[k] + x[k], \qquad \forall k. \tag{3.1}$$

Specifically about the processes $\{g[k]\}$ and $\{x[k]\}$,

- The process $\{g[k]\}$ can be taken as a function of L types of available and relevant environmental parameters $\{\phi_\ell[k]; \ell = 1, \cdots, L\}$. Consider the potentially nonlinear relationship between the slowly-varying channel parameter and water environmental parameters [15, 51, 52, 53]. The function can be represented by the Maclaurin series expansion,

$$g[k] = \sum_{\ell=1}^{L} c_\ell \phi_\ell[k] + \sum_{\ell_1=1}^{L} \sum_{\ell_2=1}^{L} c_{\ell_1,\ell_2} \phi_{\ell_1}[k] \phi_{\ell_2}[k]$$
$$+ \sum_{\ell_1=1}^{L} \sum_{\ell_2=1}^{L} \sum_{\ell_3=1}^{L} c_{\ell_1,\ell_2,\ell_3} \phi_{\ell_1}[k] \phi_{\ell_2}[k] \phi_{\ell_3}[k] + \cdots \tag{3.2}$$

where the expansion coefficients are unknown and could be slowly time-varying. Estimation of the expansion coefficients based on channel measurements and environmental parameters is challenged by their infinite dimensionality.

To make the problem tractable, a finite number of important summands on the right side of (3.2) can be selected to approximate the function. Specifically, we include the infinite elements on the right side of (3.2) in a set $\mathcal{E}[k] := \{\phi_1[k], \cdots, \phi_L[k], \phi_1^2[k], \phi_1[k]\phi_2[k], \cdots\}$, and denote $\mathcal{I}$ as an index set of N_u important elements within $\mathcal{E}[k], \forall k$. The important elements can form a

finite set $\mathcal{U}[k] := \{u_1[k], \cdots, u_{N_u}[k]\}$, which yields the approximation,

$$g[k] \approx \sum_{n=1}^{N_u} b_n u_n[k], \tag{3.3}$$

where $\{b_n\}$ denote the coefficients of the N_u important elements.

- The latent process $\{x[k]\}$ is modeled as a Markov process with memory length of P,

$$x[k] = \sum_{p=1}^{P} a_p x[k-p] + w[k], \tag{3.4}$$

where the coefficients $\{a_p\}$ are unknown and could be slowly time-varying, and the process noise $w[k]$ follows a zero-mean Gaussian distribution with variance σ_w^2, namely, $w[k] \sim \mathcal{N}(0, \sigma_w^2)$.

The latent process order P and the index set $\mathcal{I}$ of important elements in $\mathcal{E}[k]$ can be determined via a model-order selection criterion. A detailed discussion is presented in Section 3.5.

Denote $y[k]$ as the measurement of the slowly-varying channel parameter at time k. We have

$$y[k] = \gamma_0 + x[k] + g[k] + v[k], \tag{3.5}$$

where $v[k]$ is an equivalent noise term which consists of modeling inaccuracy and the measurement noise, and is assumed $v[k] \sim \mathcal{N}(0, \sigma_v^2)$, independent from the process

noise $w[k]$ in (3.4).

Define $\mathbf{a} := [a_1, \cdots, a_P]^{\mathrm{T}}$, $\mathbf{b} := [b_1, \cdots, b_{N_u}]^{\mathrm{T}}$, $\mathbf{x}[k] := [x[k], \cdots, x[k - P + 1]]^{\mathrm{T}}$, and

$\mathbf{u}[k] := [u_1[k], \cdots, u_{N_u}[k]]^{\mathrm{T}}$. The system model can be compactly represented as

$$x[k] = \mathbf{a}^{\mathrm{T}}\mathbf{x}[k - 1] + w[k], \tag{3.6a}$$

$$y[k] = \gamma_0 + x[k] + \mathbf{b}^{\mathrm{T}}\mathbf{u}[k] + v[k]. \tag{3.6b}$$

Define $\mathbf{w}[k] := [w[k], 0, \cdots, 0]^{\mathrm{T}}$, $\mathbf{h} := [1, 0, \cdots, 0]^{\mathrm{T}}$, and

$$\mathbf{A} := \begin{bmatrix} a_1 & a_2 & \cdots & a_{P-1} & a_P \\ 1 & 0 & \cdots & 0 & 0 \\ 0 & 1 & \cdots & 0 & 0 \\ \vdots & \vdots & \ddots & \vdots & \vdots \\ 0 & 0 & \cdots & 1 & 0 \end{bmatrix}.$$

We have the state-space representation of the system model,

$$\mathbf{x}[k] = \mathbf{A}\mathbf{x}[k - 1] + \mathbf{w}[k], \tag{3.7a}$$

$$y[k] = \gamma_0 + \mathbf{h}^{\mathrm{T}}\mathbf{x}[k] + \mathbf{b}^{\mathrm{T}}\mathbf{u}[k] + v[k]. \tag{3.7b}$$

Should the parameters in the set $\boldsymbol{\Theta} := \{\gamma_0, \mathbf{a}, \mathbf{b}, \sigma_w^2, \sigma_v^2\}$ be known, the latent process

56

can be tracked via the Kalman filter [60]. In the next section, we will develop a recursive algorithm to estimate the unknown model parameters while tracking the latent process based on the measurements $\{y[k]\}$ and the environmental parameter vectors $\{\mathbf{u}[k]\}$. The estimated model parameters allow multiple-step-ahead prediction of the slowly-varying channel parameter. For notation convenience, in the sequel we use $x[k]$ and x_k, $y[k]$ and y_k, $\mathbf{x}[k]$ and $\mathbf{x}_k$ interchangeably, and denote $\mathbf{x}_{k_1}^{k_2} := \{x_{k_1}, \cdots, x_{k_2}\}$ and $\mathbf{y}_{k_1}^{k_2} := \{y_{k_1}, \cdots, y_{k_2}\}$.

3.3 A Recursive Algorithm for Channel Modeling and Prediction

Following the ML principle [60], the unknown parameters in $\boldsymbol{\Theta}$ could be estimated at each time step (e.g., time k) by maximizing the log-likelihood function of the complete data set, $L_k(\boldsymbol{\Theta}) := \ln f(\mathbf{y}_0^k, \mathbf{x}_{-1}, \mathbf{x}_0^k | \boldsymbol{\Theta})$. However, note that the latent process $\{x_{k'}\}$ is not observable. The EM algorithm [57] can be applied to estimate the unknown parameters iteratively through an expectation step and a maximization step. Specifically, at time k,

- *Expectation:* Given a parameter set estimation $\hat{\boldsymbol{\Theta}}$, the expectation of the log-likelihood function can be approximated as

$$\mathbb{E}[L_k(\boldsymbol{\Theta})|\hat{\boldsymbol{\Theta}}] = \int \int \left[\ln f(\mathbf{y}_0^k, \mathbf{x}_{-1}, \mathbf{x}_0^k|\boldsymbol{\Theta})\right] \times f(\mathbf{x}_{-1}, \mathbf{x}_0^k|\mathbf{y}_0^k, \hat{\boldsymbol{\Theta}})d\mathbf{x}_{-1}d\mathbf{x}_0^k. \quad (3.8)$$

- *Maximization:* The parameter set estimation can be updated as

$$\hat{\boldsymbol{\Theta}}^{(\text{new})} = \arg \max_{\boldsymbol{\Theta}} \mathbb{E}[L_k(\boldsymbol{\Theta})|\hat{\boldsymbol{\Theta}}]. \quad (3.9)$$

The iterative operation terminates when the number of iterations reaches a pre-determined value or the change of the parameter set estimation is less than a pre-determined threshold.

Note that (3.8) can be decomposed as

$$\mathbb{E}[L_k(\boldsymbol{\Theta})|\hat{\boldsymbol{\Theta}}] = \int [\ln f(\mathbf{x}_{-1}|\boldsymbol{\Theta})]f(\mathbf{x}_{-1}|\mathbf{y}_0^k, \hat{\boldsymbol{\Theta}})d\mathbf{x}_{-1}$$
$$+ \sum_{k'=0}^{k} \int [\ln f(x_{k'}, y_{k'}|\mathbf{x}_{k'-1}, \boldsymbol{\Theta})] \times f(x_{k'}, \mathbf{x}_{k'-1}|\mathbf{y}_0^k, \hat{\boldsymbol{\Theta}})dx_{k'}d\mathbf{x}_{k'-1}. \quad (3.10)$$

The expectation $\mathbb{E}[L_k(\boldsymbol{\Theta})|\hat{\boldsymbol{\Theta}}]$ is computed based on the probability density function (PDF) $f(x_{k'}, \mathbf{x}_{k'-1}|\mathbf{y}_0^k, \hat{\boldsymbol{\Theta}})$, $\forall k' \leq k$. For a given estimation $\hat{\boldsymbol{\Theta}}$, finding $f(x_{k'}, \mathbf{x}_{k'-1}|\mathbf{y}_0^k, \hat{\boldsymbol{\Theta}})$ requires to process all the data points. Hence, the original EM algorithm is not amenable to online implementation.

We next propose an approximation to $\mathbb{E}[L_k(\boldsymbol{\Theta})|\hat{\boldsymbol{\Theta}}]$ that enables the development of a low-complexity recursive algorithm for the model parameter estimation and channel tracking.

3.3.1 Approximation for Recursive Operation

The approximation to $\mathbb{E}[L_k(\boldsymbol{\Theta})|\hat{\boldsymbol{\Theta}}]$ is made in several steps.

First, we approximate the expectation in (3.10) by

$$
\mathbb{E}[L_k(\boldsymbol{\Theta})|\hat{\boldsymbol{\Theta}}] \approx \ln f(\mathbf{x}_{-1}|\boldsymbol{\Theta})]
$$
$$
+ \sum_{k'=0}^{k} \int [\ln f(x_{k'}, y_{k'}|\mathbf{x}_{k'-1}, \boldsymbol{\Theta})] \times f(x_{k'}, \mathbf{x}_{k'-1}|\mathbf{y}_0^{k'}, \hat{\boldsymbol{\Theta}})dx_{k'}d\mathbf{x}_{k'-1}, \quad (3.11)
$$

where the expectation of $[\ln f(x_{k'}, y_{k'}|\mathbf{x}_{k'-1}, \boldsymbol{\Theta})]$ is performed with respect to $f(x_{k'}, \mathbf{x}_{k'-1}|\mathbf{y}_0^{k'}, \hat{\boldsymbol{\Theta}})$ instead of $f(x_{k'}, \mathbf{x}_{k'-1}|\mathbf{y}_0^{k}, \hat{\boldsymbol{\Theta}})$. This removes the dependence of $\{x_{k'}, \mathbf{x}_{k'-1}\}$ on future measurements.

Secondly, denote $\hat{\boldsymbol{\Theta}}_{k'}$ as the parameter set estimation at time k'. We make a further approximation to (3.11) through replacing $f(x_{k'}, \mathbf{x}_{k'-1}|\mathbf{y}_0^{k'}, \hat{\boldsymbol{\Theta}})$ by

$f(x_{k'}, \mathbf{x}_{k'-1}|\mathbf{y}_0^{k'}, \hat{\boldsymbol{\Theta}}_{k'})$, $\forall k' < k$, namely,

$$\mathbb{E}[L_k(\boldsymbol{\Theta})|\hat{\boldsymbol{\Theta}}] \approx \ln f(\mathbf{x}_{-1}|\boldsymbol{\Theta})$$

$$+ \sum_{k'=0}^{k-1} \int [\ln f(x_{k'}, y_{k'}|\mathbf{x}_{k'-1}, \boldsymbol{\Theta})] f(x_{k'}, \mathbf{x}_{k'-1}|\mathbf{y}_0^{k'}, \hat{\boldsymbol{\Theta}}_{k'}) dx_{k'} d\mathbf{x}_{k'-1}$$

$$+ \int [\ln f(x_k, y_k|\mathbf{x}_{k-1}, \boldsymbol{\Theta})] \times f(x_k, \mathbf{x}_{k-1}|\mathbf{y}_0^k, \hat{\boldsymbol{\Theta}}) dx_k d\mathbf{x}_{k-1}. \qquad (3.12)$$

The approximations in (3.11) and (3.12) enable recursive computation of the summands on the right side of (3.12).

Thirdly, note that the joint PDF $f(x_k, \mathbf{x}_{k-1}|y_k, \mathbf{y}_0^{k-1}, \hat{\boldsymbol{\Theta}})$ can be decomposed as

$$f(x_k, \mathbf{x}_{k-1}|y_k, \mathbf{y}_0^{k-1}, \hat{\boldsymbol{\Theta}})$$

$$= f(\mathbf{x}_k, \mathbf{x}_{k-1}|y_k, \mathbf{y}_0^{k-1}, \hat{\boldsymbol{\Theta}})\delta(\mathbf{x}_k, \mathbf{x}_{k-1})$$

$$= \frac{1}{c_0} f(\mathbf{x}_k, \mathbf{x}_{k-1}, y_k|\mathbf{y}_0^{k-1}, \hat{\boldsymbol{\Theta}})\delta(\mathbf{x}_k, \mathbf{x}_{k-1})$$

$$= \frac{1}{c_0} f(y_k|\mathbf{x}_k, \hat{\boldsymbol{\Theta}}) f(\mathbf{x}_k|\mathbf{x}_{k-1}, \hat{\boldsymbol{\Theta}}) f(\mathbf{x}_{k-1}|\mathbf{y}_0^{k-1}, \hat{\boldsymbol{\Theta}})\delta(\mathbf{x}_k, \mathbf{x}_{k-1}), \qquad (3.13)$$

where c_0 is a normalization constant, and the function $\delta(\mathbf{x}_k, \mathbf{x}_{k-1})$ is introduced to constrain the equity of common elements in $\mathbf{x}_k$ and $\mathbf{x}_{k-1}$. We approximate the joint

PDF by

$$\tilde{f}(x_k, \mathbf{x}_{k-1}|y_k, \mathbf{y}_0^{k-1}, \hat{\mathbf{\Theta}}) := \frac{1}{c_0'} f(y_k|\mathbf{x}_k, \hat{\mathbf{\Theta}}) f(\mathbf{x}_k|\mathbf{x}_{k-1}, \hat{\mathbf{\Theta}}) \tilde{f}(\mathbf{x}_{k-1}|\mathbf{y}_0^{k-1}, \hat{\mathbf{\Theta}}_{k-1}) \delta(\mathbf{x}_k, \mathbf{x}_{k-1}),$$

(3.14)

where c_0' is a normalization constant, and the approximation is made through replacing $f(\mathbf{x}_{k-1}|\mathbf{y}_0^{k-1}, \hat{\mathbf{\Theta}})$ in (3.13) by $\tilde{f}(\mathbf{x}_{k-1}|\mathbf{y}_0^{k-1}, \hat{\mathbf{\Theta}}_{k-1})$ in (3.14), with $\tilde{f}(\mathbf{x}_{k'}|\mathbf{y}_0^{k'}, \hat{\mathbf{\Theta}}_{k'})$ defined as the marginalization PDF of $\mathbf{x}_{k'}$ with respect to $\tilde{f}(x_{k'}, \mathbf{x}_{k'-1}|y_{k'}, \mathbf{y}_0^{k'-1}, \hat{\mathbf{\Theta}}_{k'})$, $\forall k'$.

Finally, based on (3.12) and (3.14), the expectation $\mathbb{E}[L_k(\mathbf{\Theta})|\hat{\mathbf{\Theta}}]$ is approximated by $Q_k(\mathbf{\Theta}|\hat{\mathbf{\Theta}})$ which is recursively defined as

$$Q_k(\mathbf{\Theta}|\hat{\mathbf{\Theta}}) = \lambda Q_{k-1}(\mathbf{\Theta}|\hat{\mathbf{\Theta}}_{k-1}) + \int [\ln f(x_k, y_k|\mathbf{x}_{k-1}, \mathbf{\Theta})] \tilde{f}(x_k, \mathbf{x}_{k-1}|y_k, \mathbf{y}_0^{k-1}, \hat{\mathbf{\Theta}}) d\mathbf{x}_{k-1} dx_k,$$

(3.15)

where $\lambda \in (0, 1]$ is a forgetting factor that accounts for the temporal variation of unknown model parameters.

Based on (3.14) and (3.15), a recursive algorithm will be developed for the model parameter estimation and channel tracking, while at each time step, operations similar to the expectation and the maximization in the EM algorithm are iteratively performed.

61
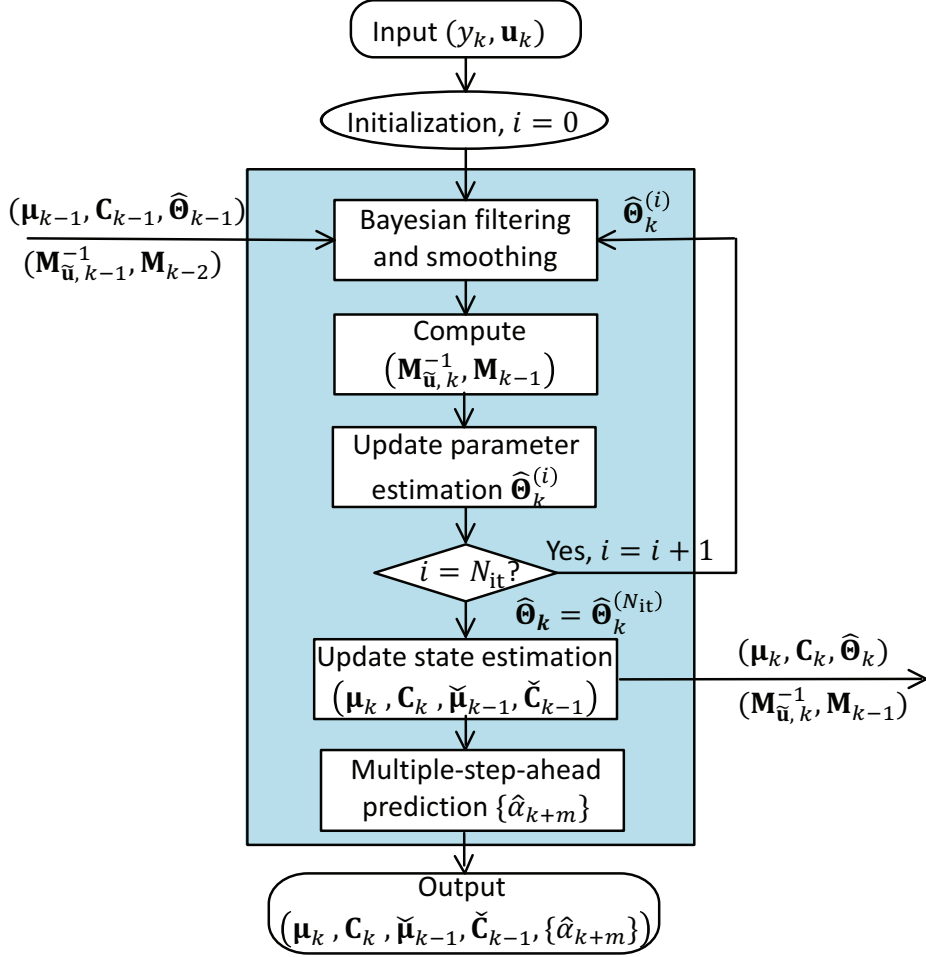
Figure 3.2: The proposed low-complexity recursive algorithm at time k.

3.3.2 A Low-complexity Recursive Algorithm

Denote $\hat{\boldsymbol{\Theta}}_k^{(i)} = \{\hat{\gamma}_{0,k}^{(i)}, \hat{\mathbf{a}}_k^{(i)}, \hat{\mathbf{b}}_k^{(i)}, \hat{\sigma}_{w,k}^{2,(i)}, \hat{\sigma}_{v,k}^{2,(i)}\}$ as the parameter set estimation in the ith iteration at time k. The function $Q_k(\boldsymbol{\Theta}|\hat{\boldsymbol{\Theta}}_k^{(i)})$ is computed through finding the expectation of $[\ln f(x_k, y_k|\mathbf{x}_{k-1}, \boldsymbol{\Theta})]$ with respect to the PDF $\tilde{f}(x_k, \mathbf{x}_{k-1}|y_k, \mathbf{y}_0^{k-1}, \hat{\boldsymbol{\Theta}}_k^{(i)})$ (c.f. (3.15)). The parameter set estimation can then be updated as $\hat{\boldsymbol{\Theta}}_k^{(i+1)} = \arg\max_{\boldsymbol{\Theta}} Q_k(\boldsymbol{\Theta}|\hat{\boldsymbol{\Theta}}_k^{(i)})$.

At the outset, the proposed low-complexity recursive algorithm is depicted in Fig. 3.2. Denote $\tilde{f}(\mathbf{x}_k|\mathbf{y}_0^k, \hat{\boldsymbol{\Theta}}_k) = \mathcal{N}(\boldsymbol{\mu}_k, \mathbf{C}_k)$ (c.f. (3.14)). At time k, the algorithm takes the PDF $\tilde{f}(\mathbf{x}_{k-1}|\mathbf{y}_0^{k-1}, \hat{\boldsymbol{\Theta}}_{k-1}) = \mathcal{N}(\boldsymbol{\mu}_{k-1}, \mathbf{C}_{k-1})$, the parameter set estimation $\hat{\boldsymbol{\Theta}}_{k-1}$, auxiliary quantities $\{\mathbf{M}_{k-2}, \mathbf{M}_{\tilde{\mathbf{u}},k-1}^{-1}\}$ (to be defined shortly; computed at time $(k-1)$), the measurement y_k and the environmental parameter vector $\mathbf{u}_k$ as input. Set $\hat{\boldsymbol{\Theta}}_k^{(0)} = \hat{\boldsymbol{\Theta}}_{k-1}$. Given the parameter set estimation $\hat{\boldsymbol{\Theta}}_k^{(i)}$, the Kalman filtering and smoothing can be performed to compute the expectations of quantities in $[\ln f(x_k, y_k|\mathbf{x}_{k-1}, \boldsymbol{\Theta})]$ with respect to the PDF $\tilde{f}(x_k, \mathbf{x}_{k-1}|y_k, \mathbf{y}_0^{k-1}, \hat{\boldsymbol{\Theta}}_k^{(i)})$, namely, the second summand in (3.15). The parameter set estimation can then be updated through maximizing $Q_k(\boldsymbol{\Theta}|\hat{\boldsymbol{\Theta}}_k^{(i)})$. The updated parameter estimation can then be used for the Kalman filtering and smoothing in the next iteration. The iterative operation terminates when the number of iterations reaches a pre-determined threshold N_{it}. We set $\hat{\boldsymbol{\Theta}}_k^{(N_{\text{it}})} = \hat{\boldsymbol{\Theta}}_k$ as the final parameter set estimation at time k. Based on $\hat{\boldsymbol{\Theta}}_k$, the PDF $\tilde{f}(\mathbf{x}_k|\mathbf{y}_0^k, \hat{\boldsymbol{\Theta}}_k) = \mathcal{N}(\boldsymbol{\mu}_k, \mathbf{C}_k)$ is computed via the Kalman filtering. The PDF $\tilde{f}(\mathbf{x}_k|\mathbf{y}_0^k, \hat{\boldsymbol{\Theta}}_k)$, the parameter set estimation $\hat{\boldsymbol{\Theta}}_k$ and $\{\mathbf{M}_{k-1}, \mathbf{M}_{\tilde{\mathbf{u}},k}^{-1}\}$ that are computed at time k, will be used for the recursive operation at time $(k+1)$. Additionally, based on the parameter set estimation $\hat{\boldsymbol{\Theta}}_k$ and the state estimation $\boldsymbol{\mu}_k$, multiple-step-ahead prediction of the slowly-varying channel parameter can be achieved.

Next, we describe in details the component of the recursive and iterative parameter estimation, the Kalman filtering and smoothing, and the multiple-step-ahead prediction.

3.3.2.1   Recursive and Iterative Parameter Estimation

The parameter estimation can be updated by maximizing $Q_k(\boldsymbol{\Theta}|\hat{\boldsymbol{\Theta}}_k^{(i)})$. Note that $f(x_k, y_k|\mathbf{x}_{k-1}, \boldsymbol{\Theta}) = f(y_k|x_k, \boldsymbol{\Theta})f(x_k|\mathbf{x}_{k-1}, \boldsymbol{\Theta})$. Substitute $f(y_k|x_k, \boldsymbol{\Theta}) = \mathcal{N}(\gamma_0 + x_k + \mathbf{b}^{\mathrm{T}}\mathbf{u}_k, \sigma_v^2)$ and $f(x_k|\mathbf{x}_{k-1}) = \mathcal{N}(\mathbf{a}^{\mathrm{T}}\mathbf{x}_{k-1}, \sigma_w^2)$ into the log-likelihood function in (3.15). Denote $\tilde{\mathbf{u}}_k := [1, \mathbf{u}_k^{\mathrm{T}}]^{\mathrm{T}}$. Set the partial derivative of $Q_k(\boldsymbol{\Theta}|\hat{\boldsymbol{\Theta}}_k^{(i)})$ with respect to each unknown parameter to zero. A set of recursive equations can be obtained; see the detailed derivation in Appendix A,

$$\hat{\mathbf{a}}_k^{(i+1)} = \hat{\mathbf{a}}_{k-1} + \mathbf{M}_{k-1}^{-1}\left(\mathbb{E}[x_k\mathbf{x}_{k-1}] - \mathbb{E}[\mathbf{x}_{k-1}\mathbf{x}_{k-1}^{\mathrm{T}}]\hat{\mathbf{a}}_{k-1}\right), \tag{3.16a}$$

$$\hat{\sigma}_{w,k}^{2,(i+1)} = \hat{\sigma}_{w,k-1}^2 + \frac{1-\lambda}{1-\lambda^k}\left\{\mathbb{E}\left[\left(x_k - \hat{\mathbf{a}}_k^{(i+1),\mathrm{T}}\mathbf{x}_{k-1}\right)^2\right] - \hat{\sigma}_{w,k-1}^2\right\}, \tag{3.16b}$$

$$\begin{bmatrix}\hat{\gamma}_{0,k}^{(i+1)} \\ \hat{\mathbf{b}}_k^{(i+1)}\end{bmatrix} = \begin{bmatrix}\hat{\gamma}_{0,k-1} \\ \hat{\mathbf{b}}_{k-1}\end{bmatrix} + \frac{\mathbf{M}_{\tilde{\mathbf{u}},k}^{-1}\tilde{\mathbf{u}}_k}{\lambda + \tilde{\mathbf{u}}_k^{\mathrm{T}}\mathbf{M}_{\tilde{\mathbf{u}},k}^{-1}\tilde{\mathbf{u}}_k}\left(y_k - \mathbb{E}[x_k] - \hat{\gamma}_{0,k-1} - \hat{\mathbf{b}}_{k-1}^{\mathrm{T}}\mathbf{u}_k\right), \tag{3.16c}$$

$$\hat{\sigma}_{v,k}^{2,(i+1)} = \hat{\sigma}_{v,k-1}^2 + \frac{1-\lambda}{1-\lambda^{k+1}}\left\{\mathbb{E}\left[(y_k - x_k - \hat{\gamma}_{0,k}^{(i+1)} - \hat{\mathbf{b}}_k^{(i+1),\mathrm{T}}\mathbf{u}_k)^2\right] - \hat{\sigma}_{v,k-1}^2\right\}, \tag{3.16d}$$

with two matrices defined as

$$\mathbf{M}_{k-1} := \lambda\mathbf{M}_{k-2} + \mathbb{E}[\mathbf{x}_{k-1}\mathbf{x}_{k-1}^{\mathrm{T}}], \tag{3.17a}$$

$$\mathbf{M}_{\tilde{\mathbf{u}},k} := \lambda\mathbf{M}_{\tilde{\mathbf{u}},k-1} + \tilde{\mathbf{u}}_k\tilde{\mathbf{u}}_k^{\mathrm{T}}. \tag{3.17b}$$

The expectations in (3.16) and (3.17) are performed with respect to $\tilde{f}(x_k, \mathbf{x}_{k-1}|y_k, \mathbf{y}_0^{k-1}, \hat{\mathbf{\Theta}}_k^{(i)})$ (c.f. (3.15)).

3.3.2.2 Kalman Filtering and Smoothing

Computation of the expectations in (3.16) and (3.17) requires the marginalization of the joint PDF $\tilde{f}(x_k, \mathbf{x}_{k-1}|y_k, \mathbf{y}_0^{k-1}, \hat{\mathbf{\Theta}}_k^{(i)})$ with respect to $\mathbf{x}_k$ and $\mathbf{x}_{k-1}$, respectively. Denote the marginal PDFs as $\tilde{f}(\mathbf{x}_k|\mathbf{y}_0^k, \hat{\mathbf{\Theta}}_k^{(i)}) = \mathcal{N}(\boldsymbol{\mu}_k^{(i)}, \mathbf{C}_k^{(i)})$ and $\breve{f}(\mathbf{x}_{k-1}|\mathbf{y}_0^k, \hat{\mathbf{\Theta}}_k^{(i)}) = \mathcal{N}(\breve{\boldsymbol{\mu}}_{k-1}^{(i)}, \breve{\mathbf{C}}_{k-1}^{(i)})$. Given the expansion of the joint PDF in (3.14), the marginalization can be performed through the Kalman filtering and smoothing [60], as detailed next.

Define $\hat{\mathbf{A}}_k^{(i)}$ and $\hat{\mathbf{C}}_{\mathbf{w},k}^{(i)}$ as the matrices corresponding to $\hat{\mathbf{a}}_k^{(i)}$ and $\hat{\sigma}_{w,k}^{2,(i)}$, respectively. Based on $\tilde{f}(\mathbf{x}_{k-1}|\mathbf{y}_0^{k-1}, \hat{\mathbf{\Theta}}_{k-1})$ and the system model in (3.7), the mean and the covariance matrix of $\mathbf{x}_k$ in the marginal PDF $\tilde{f}(\mathbf{x}_k|\mathbf{y}_0^k, \hat{\mathbf{\Theta}}_k^{(i)})$ can be formulated as

$$\boldsymbol{\mu}_k^{(i)} = \hat{\mathbf{A}}_k^{(i)} \boldsymbol{\mu}_{k-1} + \mathbf{k}_k^{(i)}(y_k - \hat{\mathbf{a}}_k^{(i),\mathrm{T}} \boldsymbol{\mu}_{k-1} - \hat{\gamma}_{0,k}^{(i)} - \hat{\mathbf{b}}_k^{(i),\mathrm{T}} \mathbf{u}_k), \qquad (3.18a)$$

$$\mathbf{C}_k^{(i)} = (\mathbf{I} - \mathbf{k}_k^{(i)} \mathbf{h}^{\mathrm{T}}) \mathbf{P}_k^{(i)}, \qquad (3.18b)$$

where the Kalman gain $\mathbf{k}_k^{(i)} = \mathbf{P}_k^{(i)} \mathbf{h}(\hat{\sigma}_{v,k}^{2,(i)} + \mathbf{h}^{\mathrm{T}} \mathbf{P}_k^{(i)} \mathbf{h})^{-1}$ and the prediction mean square error (MSE) matrix $\mathbf{P}_k^{(i)} = \hat{\mathbf{A}}_k^{(i)} \mathbf{C}_{k-1} \hat{\mathbf{A}}_k^{(i),\mathrm{T}} + \hat{\mathbf{C}}_{\mathbf{w}}^{(i)}$. We further have $\mathbb{E}[\mathbf{x}_k \mathbf{x}_k^{\mathrm{T}}|\hat{\mathbf{\Theta}}_k^{(i)}] = \mathbf{C}_k^{(i)} + \boldsymbol{\mu}_k^{(i)} \boldsymbol{\mu}_k^{(i),\mathrm{T}}$.

The marginal PDF $\breve{f}(\mathbf{x}_{k-1}|\mathbf{y}_0^k, \hat{\boldsymbol{\Theta}}_k^{(i)})$ can be obtained via the one-step backward smoothing, with the mean and the covariance matrix formulated as

$$\breve{\boldsymbol{\mu}}_{k-1}^{(i)} = \boldsymbol{\mu}_{k-1} + \mathbf{J}_{k-1}^{(i)}(\boldsymbol{\mu}_k^{(i)} - \hat{\mathbf{A}}_k^{(i)}\boldsymbol{\mu}_{k-1}), \tag{3.19a}$$

$$\breve{\mathbf{C}}_{k-1}^{(i)} = \mathbf{C}_{k-1} + \mathbf{J}_{k-1}^{(i)}(\mathbf{C}_k^{(i)} - \mathbf{P}_k^{(i)})\mathbf{J}_{k-1}^{(i),\mathrm{T}}, \tag{3.19b}$$

where the gain matrix $\mathbf{J}_{k-1}^{(i)} = \mathbf{C}_{k-1}\hat{\mathbf{A}}_k^{(i),\mathrm{T}}(\mathbf{P}_k^{(i)})^{-1}$. We further have $\mathbb{E}[\mathbf{x}_{k-1}\mathbf{x}_{k-1}^{\mathrm{T}}|\hat{\boldsymbol{\Theta}}_k^{(i)}] = \breve{\mathbf{C}}_{k-1}^{(i)} + \breve{\boldsymbol{\mu}}_{k-1}^{(i)}\breve{\boldsymbol{\mu}}_{k-1}^{(i),\mathrm{T}}$.

Based on the joint PDF $\tilde{f}(x_k, \mathbf{x}_{k-1}|y_k, \mathbf{y}_0^{k-1}, \hat{\boldsymbol{\Theta}}_k^{(i)})$, the correlation between $\mathbf{x}_k$ and $\mathbf{x}_{k-1}$ can be obtained as

$$\mathbb{E}[\mathbf{x}_k\mathbf{x}_{k-1}^{\mathrm{T}}|\hat{\boldsymbol{\Theta}}_k^{(i)}] = \mathbf{C}_k^{(i)}\mathbf{J}_{k-1}^{(i),\mathrm{T}} + \boldsymbol{\mu}_k^{(i)}\breve{\boldsymbol{\mu}}_{k-1}^{(i),\mathrm{T}}. \tag{3.20}$$

The expectations $\mathbb{E}[x_k|\hat{\boldsymbol{\Theta}}_k^{(i)}]$, $\mathbb{E}[x_k\mathbf{x}_{k-1}^{\mathrm{T}}|\hat{\boldsymbol{\Theta}}_k^{(i)}]$, and $\mathbb{E}[x_k^2|\hat{\boldsymbol{\Theta}}_k^{(i)}]$ to be used in (3.16) can be extracted from $\mathbb{E}[\mathbf{x}_k|\hat{\boldsymbol{\Theta}}_k^{(i)}] = \boldsymbol{\mu}_k^{(i)}$, $\mathbb{E}[\mathbf{x}_k\mathbf{x}_{k-1}^{\mathrm{T}}|\hat{\boldsymbol{\Theta}}_k^{(i)}]$, and $\mathbb{E}[\mathbf{x}_k\mathbf{x}_k^{\mathrm{T}}|\hat{\boldsymbol{\Theta}}_k^{(i)}]$, respectively.

3.3.2.3 Multiple-step-ahead Prediction

Based on the parameter set estimation $\hat{\boldsymbol{\Theta}}_k$ and the state estimation $\boldsymbol{\mu}_k$ (denoted next also as $\hat{\mathbf{x}}_k$), the m-step-ahead prediction of the slowly-varying channel parameter can

66

be recursively computed based on the system model in (3.6). Specifically,

$$\hat{x}_{k+m} = \hat{\mathbf{a}}_k^{\mathrm{T}} \hat{\mathbf{x}}_{k+m-1}, \tag{3.21a}$$

$$\hat{\alpha}_{k+m} = \hat{\gamma}_{0,k} + \hat{x}_{k+m} + \hat{\mathbf{b}}_k^{\mathrm{T}} \mathbf{u}_{k+m}, \tag{3.21b}$$

for $m = 1, \cdots$, where $\mathbf{u}_{k+m}$ can be obtained from meteorological forecast sources, e.g., [61].

Remark 2. Although this Chapter assumes periodic channel measurements, the proposed model and the recursive algorithm can be applied to the scenario with non-periodic channel measurements through replacing the discrete-time state-space model in (3.7) by a continuous-time state-space model (c.f. [60, Chap. 9]).

Remark 3. The proposed model and the recursive algorithm subsume a linear regression method that models the temporal evolution of the slowly-varying channel parameter only based on available environmental parameters without introducing the latent process, namely, the model in (3.5) degrades to $y_k = \gamma_0 + g_k + w_k$. The model parameters γ_0 and $\mathbf{b}$ can be recursively estimated via (3.16c).

67

3.3.2.4 Computational Complexity

The computational complexity of the proposed algorithm at each time step is analyzed in the following. At the outset, we would like to note that in practical systems, the values of P and N_u are typically very small. In Section 3.7, $N_{\text{it}} = 20$ and $N_u = 2$ are used for the experimental data processing, and the value of P varies from 1 to 4 for different channel parameters.

- *Kalman filtering and smoothing:* For (3.18), calculation of the Kalman gain vector $\mathbf{k}_k^{(i)}$ of length P has $(P^2 + 2P)$ arithmetic multiplications (AMs), $(P^2 + P + 2)$ arithmetic additions (AAs) and 1 arithmetic division (AD). Calculation of the MSE matrix $\mathbf{P}_k^{(i)}$ of size $(P \times P)$ has $(2P^3)$ AMs and $(2P^3 + 2P^2)$ AAs. Eq. (3.18a) has $(P^2 + 2P + N_u)$ AMs and $(P^2 + 3P + N_u + 4)$ AAs, and Eq. (3.18b) has $(P^3 + P^2)$ AMs and $(P^3 + 2P^2)$ AAs. The total computations associated with (3.18) include $(3P^3 + 3P^2 + 4P + N_u)$ AMs, $(3P^3 + 6P^2 + 4P + 4 + N_u)$ AAs and 1 AD. For (3.19), calculation of the gain matrix $\mathbf{J}_{k-1}^{(i)}$ of size $(P \times P)$ has $(2P^3)$ AMs and $(2P^3)$ AAs for the matrix multiplication and a complexity of $\mathcal{O}(P^3)$ for the inversion of matrix $\mathbf{P}_k^{(i)}$. Eq. (3.19a) has $(2P^2)$ AMs and $(2P^2 + 4P)$ AAs, and Eq. (3.19b) has $(2P^3)$ AMs and $(2P^3 + 4P^2)$ AAs. The total computations associated with (3.19) include $(4P^3 + 2P^2)$ AMs, $(4P^3 + 6P^2 + 4P)$ AAs and a $(P \times P)$ matrix inversion with complexity $\mathcal{O}(P^3)$. In addition, calculation

of $\mathbb{E}[\mathbf{x}_k\mathbf{x}_k^{\mathrm{T}}|\hat{\boldsymbol{\Theta}}_k^{(i)}]$ and of $\mathbb{E}[\mathbf{x}_{k-1}\mathbf{x}_{k-1}^{\mathrm{T}}|\hat{\boldsymbol{\Theta}}_k^{(i)}]$ each has (P^2) AMs and $(2P^2)$ AAs. Calculation of the correlation matrix in (3.20) has (P^3+P^2) AMs and (P^3+2P^2) AAs. Therefore, the total computations for Kalman filtering and smoothing include $(8P^3 + 8P^2 + 4P + N_u)$ AMs, $(8P^3 + 18P^2 + 8P + 6 + N_u)$ AAs, 1 AD and the inversion of a $(P \times P)$ matrix with complexity $\mathcal{O}(P^3)$.

- *Parameter estimation:* For (3.16a), calculation of the matrix $\mathbf{M}_{k-1}$ of size $(P \times P)$ in (3.17a) has (P^2) AMs and $(2P^2)$ AAs. Eq. (3.16a) has $(2P^2)$ AMs, $(2P^2+4P)$ AAs and the inversion of $\mathbf{M}_{k-1}$ with complexity $\mathcal{O}(P^3)$. Eq. (3.16b) has (P^2+3P+1) AMs and (P^2+2P+6) AAs. Eq. (3.16c) involves the calculation and the inversion of matrix $\mathbf{M}_{\tilde{\mathbf{u}},k}$ of size $(N_u + 1) \times (N_u + 1)$. Note that the Woodbury matrix identity [60] can be applied for the recursive computation of $\mathbf{M}_{\tilde{\mathbf{u}},k}^{-1}$ based on $\mathbf{M}_{\tilde{\mathbf{u}},k-1}^{-1}$. Therefore, the total computations associated with (3.16c) include $(5N_u^2 + 13N_u + 9)$ AMs, $(4N_u^2 + 12N_u + 16)$ AAs and 2 ADs. Lastly, Eq. (3.16d) has $(N_u + 4)$ AMs and $(N_u + 9)$ AAs. Therefore, the total computations to update the parameter estimations include $(3P^2 + 3P + 5N_u^2 + 14N_u + 14)$ AMs, $(3P^2 + 6P + 4N_u^2 + 13N_u + 31)$ AAs, 2 ADs and the inversion of a $(P \times P)$ matrix with complexity $\mathcal{O}(P^3)$.

- *Iterative operations:* The proposed algorithm performs N_{it} iterations of computations in (3.16) - (3.20). Therefore, the computations at each time step include $N_{\mathrm{it}}(8P^3+11P^2+7P+5N_u^2+15N_u+14)$ AMs, $N_{\mathrm{it}}(8P^3+21P^2+14P+4N_u^2+14N_u+37)$ AAs, $(3N_{\mathrm{it}})$ ADs and a complexity of $\mathcal{O}\big(2N_{\mathrm{it}}(P^3)\big)$ for matrix

69

inversion.

3.4   Modeling and Prediction in Seasonal Channels

The UWA channel could exhibit periodic variations, such as the diurnal pattern as depicted in Fig. 2.4. In this type of channels, the slowly-varying channel parameter in one cycle could be highly correlated with those in previous cycles. Following the terminology in time series analysis [49], we refer to such type of channels as *seasonal channels.*

The data-driven model in (3.5) applies to seasonal channels. However, different from non-seasonal channels, the latent process in seasonal channels will be represented by a multiplicative seasonal AR process $(AR(P) \times (P_{se})_S)$ [49], whose polynomial representation in the lag operator D is a multiplication of the polynomial of an $AR(P)$ process, $(1 - \sum_{p=1}^{P} a_p D^p)$, and the polynomial of a seasonal $AR(P_{se})$ process, $(1 - \sum_{q=1}^{P_{se}} \xi_q D^{qS})$, where $S \gg P$ denotes the seasonal cycle. The latent process in the time domain can be represented as

$$x[k] = \sum_{p=1}^{P} a_p x[k-p] + \sum_{q=1}^{P_{se}} \xi_q x[k-qS] - \sum_{p=1}^{P} \sum_{q=1}^{P_{se}} a_p \xi_q x[k-qS-p] + w[k]. \quad (3.22)$$

The proposed recursive algorithm for non-seasonal channels could be applied to seasonal channels by defining a long state vector $[x_k, x_{k-1}, \cdots, x_{k-P_{\text{se}}S-P+1}]^{\text{T}}$ of length $(P + P_{\text{se}}S)$. This, however, will incur very large computational and storage cost. In this section, we will exploit the structure of (3.22), and develop a low-cost recursive algorithm for seasonal channels. To make the exposition easier, we focus on a simple scenario with $P_{\text{se}} = 1$, namely,

$$x[k] = \sum_{p=1}^{P} a_p x[k-p] + \xi x[k-S] - \xi \sum_{p=1}^{P} a_p x[k-S-p] + w[k], \qquad (3.23)$$

while the developed algorithm can be extended to the scenario $P_{\text{se}} > 1$ with slight modification.

Based on (3.23), we introduce an auxiliary random variable,

$$z_k := x_k - \xi x_{k-S}, \qquad (3.24)$$

which according to (3.23), forms an AR process,

$$z_k = \sum_{p=1}^{P} a_p z_{k-p} + w_k. \qquad (3.25)$$

Define $\mathbf{z}_k := [z_k, \cdots, z_{k-P+1}]^{\text{T}}$. We have the state-space representation of (3.25),

$$\mathbf{z}_k = \mathbf{A}\mathbf{z}_{k-1} + \mathbf{w}_k, \qquad (3.26)$$

71

where $\mathbf{A}$ and $\mathbf{w}_k$ are defined as in (3.7). The latent process can be reformulated as

$$x_k = \mathbf{a}^{\mathrm{T}} \mathbf{z}_{k-1} + \xi x_{k-S} + w_k. \tag{3.27}$$

Note that according to the principle of orthogonality [60], x_{k-S} is independent of z_k (c.f. (3.24)) and correspondingly $(\mathbf{a}^{\mathrm{T}} \mathbf{z}_{k-1})$ (c.f. (3.25)).

3.4.1 Approximation for Recursive Operation

We redefine the unknown parameter set as $\boldsymbol{\Theta} := \{\gamma_0, \mathbf{a}, \xi, \mathbf{b}, \sigma_w^2, \sigma_v^2\}$. Based on (3.27), the log-likelihood function $[\ln f(\mathbf{y}_0^k, \mathbf{x}_{-1}, \mathbf{x}_0^k | \boldsymbol{\Theta})]$ can be decomposed as

$$L_k(\boldsymbol{\Theta}) = \sum_{k'=0}^{k} \ln f(x_{k'}, y_{k'} | \mathbf{z}_{k'-1}, x_{k'-S}, \boldsymbol{\Theta}) + \ln f(x_{-1}, \cdots, x_{-S} | \boldsymbol{\Theta}). \tag{3.28}$$

Similar to non-seasonal channels, for the development of a recursive algorithm, an approximation to $\mathbb{E}\big[L_k(\boldsymbol{\Theta}) | \hat{\boldsymbol{\Theta}}\big]$ can be made through several steps. Particularly about

the joint PDF $f(x_k, \mathbf{z}_{k-1}, x_{k-S}|\mathbf{y}_0^k, \hat{\boldsymbol{\Theta}})$, it can be decomposed and approximated as

$$f(x_k, \mathbf{z}_{k-1}, x_{k-S}|y_k, \mathbf{y}_0^{k-1}, \hat{\boldsymbol{\Theta}}) = \frac{1}{c_1} f(x_k, \mathbf{z}_{k-1}, x_{k-S}, y_k|\mathbf{y}_0^{k-1}, \hat{\boldsymbol{\Theta}}) \tag{3.29a}$$

$$= \frac{1}{c_1} f(y_k|x_k, \hat{\boldsymbol{\Theta}}) f(x_k|\mathbf{z}_{k-1}, x_{k-S}, \hat{\boldsymbol{\Theta}}) f(\mathbf{z}_{k-1}, x_{k-S}|\mathbf{y}_0^{k-1}, \hat{\boldsymbol{\Theta}}) \tag{3.29b}$$

$$\approx \frac{1}{c_1'} f(y_k|x_k, \hat{\boldsymbol{\Theta}}) f(x_k|\mathbf{z}_{k-1}, x_{k-S}, \hat{\boldsymbol{\Theta}}) f(\mathbf{z}_{k-1}|\mathbf{y}_0^{k-1}, \hat{\boldsymbol{\Theta}}) f(x_{k-S}|\mathbf{y}_0^{k-1}, \hat{\boldsymbol{\Theta}}) \tag{3.29c}$$

$$= \frac{1}{c_1'} f(y_k|x_k, \hat{\boldsymbol{\Theta}}) f(z_k|\mathbf{z}_{k-1}, \hat{\boldsymbol{\Theta}}) f(\mathbf{z}_{k-1}|\mathbf{y}_0^{k-1}, \hat{\boldsymbol{\Theta}}) f(x_{k-S}|\mathbf{y}_0^{k-1}, \hat{\boldsymbol{\Theta}}) \delta(z_k, x_k - \xi x_{k-S}) \tag{3.29d}$$

$$= \frac{1}{c_1'} f(y_k|x_k, \hat{\boldsymbol{\Theta}}) f(z_k|\mathbf{z}_{k-1}, \hat{\boldsymbol{\Theta}}) f(\mathbf{z}_{k-1}|\mathbf{y}_0^{k-1}, \hat{\boldsymbol{\Theta}}) f(x_{k-S}|\mathbf{y}_0^{k-1}, \hat{\boldsymbol{\Theta}})$$

$$\times \delta(z_k, x_k - \xi x_{k-S}) \delta(\mathbf{z}_k, \mathbf{z}_{k-1}), \tag{3.29e}$$

where c_1 and c_1' are normalization constants, $\delta(z_k, x_k - \xi x_{k-S})$ is introduced to ensure the equity in (3.24), and the approximation from (3.29b) to (3.29c) is made by assuming that $f(\mathbf{z}_{k-1}, x_{k-S}|\mathbf{y}_0^{k-1}, \hat{\boldsymbol{\Theta}}) \approx f(\mathbf{z}_{k-1}|\mathbf{y}_0^{k-1}, \hat{\boldsymbol{\Theta}}) f(x_{k-S}|\mathbf{y}_0^{k-1}, \hat{\boldsymbol{\Theta}})$. We further approximate the above PDF by

$$\tilde{f}(x_k, \mathbf{z}_{k-1}, x_{k-S}|\mathbf{y}_0^k, \hat{\boldsymbol{\Theta}}) := \frac{1}{c_1''} f(y_k|x_k, \hat{\boldsymbol{\Theta}}) f(\mathbf{z}_k|\mathbf{z}_{k-1}, \hat{\boldsymbol{\Theta}})$$

$$\times \tilde{f}(\mathbf{z}_{k-1}|\mathbf{y}_0^{k-1}, \hat{\boldsymbol{\Theta}}_{k-1}) \tilde{f}(x_{k-S}|\mathbf{y}_0^{k-S}, \hat{\boldsymbol{\Theta}}_{k-S}) \delta(z_k, x_k - \xi x_{k-S}) \delta(\mathbf{z}_k, \mathbf{z}_{k-1}), \tag{3.30}$$

where c_1'' is a normalization constant, and the approximation is made through replacing $f(\mathbf{z}_{k-1}|\mathbf{y}_0^{k-1}, \hat{\boldsymbol{\Theta}})$ and $f(x_{k-S}|\mathbf{y}_0^{k-1}, \hat{\boldsymbol{\Theta}})$ in (3.29e) by $\tilde{f}(\mathbf{z}_{k-1}|\mathbf{y}_0^{k-1}, \hat{\boldsymbol{\Theta}}_{k-1})$ and $\tilde{f}(x_{k-S}|\mathbf{y}_0^{k-S}, \hat{\boldsymbol{\Theta}}_{k-S})$, respectively, with $\tilde{f}(\mathbf{z}_{k'}|\mathbf{y}_0^{k'}, \hat{\boldsymbol{\Theta}}_{k'})$ and $\tilde{f}(x_{k'}|\mathbf{y}_0^{k'}, \hat{\boldsymbol{\Theta}}_{k'})$ defined as

the marginalization of $\tilde{f}(x_{k'}, \mathbf{z}_{k'-1}, x_{k'-S}|\mathbf{y}_0^{k'}, \hat{\mathbf{\Theta}})$ with respect to $\mathbf{z}_{k'}$ and $x_{k'}$, $\forall k'$.

Similar to the non-seasonal channel, the expectation $\mathbb{E}[L_k(\mathbf{\Theta})|\hat{\mathbf{\Theta}}]$ can be approximated by $Q_{\text{se},k}(\mathbf{\Theta}|\hat{\mathbf{\Theta}})$ which is recursively defined as

$$Q_{\text{se},k}(\mathbf{\Theta}|\hat{\mathbf{\Theta}}) = \lambda Q_{\text{se},k-1}(\mathbf{\Theta}|\hat{\mathbf{\Theta}}_{k-1})$$
$$+ \int [\ln f(x_k, y_k|\mathbf{z}_{k-1}, x_{k-S}, \mathbf{\Theta})]\tilde{f}(x_k, \mathbf{z}_{k-1}, x_{k-S}|\mathbf{y}_0^k, \hat{\mathbf{\Theta}})dx_k d\mathbf{z}_{k-1}dx_{k-S}. \quad (3.31)$$

3.4.2   A Low-complexity Recursive Algorithm

The proposed algorithm for seasonal channels operates recursively in a similar fashion as that for non-seasonal channels. Denote $\tilde{f}(x_{k-S}|\mathbf{y}_0^{k-S}, \hat{\mathbf{\Theta}}_{k-S}) = \mathcal{N}(\mu_{k-S}, \sigma_{k-S}^2)$ and $\tilde{f}(\mathbf{z}_{k-1}|\mathbf{y}_0^{k-1}, \hat{\mathbf{\Theta}}_{k-1}) = \mathcal{N}(\boldsymbol{\mu}_{\mathbf{z},k-1}, \mathbf{C}_{\mathbf{z},k-1})$. At time k, the algorithm takes $\tilde{f}(\mathbf{z}_{k-1}|\mathbf{y}_0^{k-1}, \hat{\mathbf{\Theta}}_{k-1})$, $\tilde{f}(x_{k-S}|\mathbf{y}_0^{k-S}, \hat{\mathbf{\Theta}}_{k-S})$, the parameter set estimation $\hat{\mathbf{\Theta}}_{k-1}$, auxiliary quantities $(\tilde{\mathbf{M}}_{\mathbf{a},k-2}, \tilde{m}_{\xi,k-2}, \mathbf{M}_{\tilde{\mathbf{u}},k-1}^{-1})$ (to be defined shortly; computed at time $(k-1)$), the measurement y_k and the environmental parameter vector $\mathbf{u}_k$ as input, and sets $\hat{\mathbf{\Theta}}_k^{(0)} = \hat{\mathbf{\Theta}}_{k-1}$. The parameter set estimation and the Bayesian filtering and smoothing can be performed iteratively, until the number of iterations reaches a pre-determined threshold N_{it}. The final parameter set estimation at time k is set as $\hat{\mathbf{\Theta}}_k = \hat{\mathbf{\Theta}}_k^{(N_{\text{it}})}$. Based on $\hat{\mathbf{\Theta}}_k$, the PDFs $\tilde{f}(\mathbf{z}_k|\mathbf{y}_0^k, \hat{\mathbf{\Theta}}_k) = \mathcal{N}(\boldsymbol{\mu}_{\mathbf{z},k}, \mathbf{C}_{\mathbf{z},k})$ and $\tilde{f}(x_k|\mathbf{y}_0^k, \hat{\mathbf{\Theta}}_k) = \mathcal{N}(\mu_k, \sigma_k^2)$ are computed via the Bayesian filtering. The PDF

$\tilde{f}(\mathbf{z}_k|\mathbf{y}_0^k, \hat{\boldsymbol{\Theta}}_k)$, $\hat{\boldsymbol{\Theta}}_k$ and $(\tilde{\mathbf{M}}_{\mathbf{a},k-1}, \tilde{m}_{\xi,k-1}, \mathbf{M}_{\tilde{\mathbf{u}},k}^{-1})$ that are computed at time k, will be used for the recursive operation at time $(k+1)$. The PDF $\tilde{f}(x_k|\mathbf{y}_0^k, \hat{\boldsymbol{\Theta}}_k)$ will be used for the recursive operation at time $(k+S)$. Additionally, based on the parameter set estimation $\hat{\boldsymbol{\Theta}}_k$ and the state estimation $\boldsymbol{\mu}_{\mathbf{z},k}$ and $\{\mu_{k'}; k' \leq k\}$, multiple-step-ahead prediction of the slowly-varying channel parameter can be achieved.

We next briefly describe the recursive and iterative parameter estimation and the multiple-step-ahead prediction. A detailed description of the Bayesian filtering and smoothing is presented in Section 3.4.3.

3.4.2.1 Recursive and Iterative Parameter Estimation

At time k, given the parameter set estimation in the ith iteration, $\hat{\boldsymbol{\Theta}}_k^{(i)}$, and following the same procedure as in Section 3.3.2.1, the parameter set estimation can be updated through maximizing $Q_{\mathrm{se},k}(\boldsymbol{\Theta}|\hat{\boldsymbol{\Theta}}_k^{(i)})$. Specifically, the estimations of $\{\gamma_0, \mathbf{b}_k, \sigma_v^2\}$ can be updated according to the same equations as in (3.16). The estimations of $\{\mathbf{a}, \xi, \sigma_w^2\}$ can be updated as

$$\hat{\mathbf{a}}_k^{(i+1)} = \hat{\mathbf{a}}_{k-1} + \tilde{\mathbf{M}}_{\mathbf{a},k-1}^{-1} \Big\{ \mathbb{E}\left[z_k \mathbf{z}_{k-1}\right] - \mathbb{E}\left[\mathbf{z}_{k-1}\mathbf{z}_{k-1}^{\mathrm{T}}\right] \hat{\mathbf{a}}_{k-1} \Big\}, \tag{3.32a}$$

$$\hat{\xi}_k^{(i+1)} = \hat{\xi}_{k-1} + \tilde{m}_{\xi,k-1}^{-1} \Big\{ \mathbb{E}\left[(x_k - \hat{\mathbf{a}}_k^{(i+1),\mathrm{T}}\mathbf{z}_{k-1})x_{k-S}\right] - \mathbb{E}\left[x_{k-S}^2\right] \hat{\xi}_{k-1} \Big\}, \tag{3.32b}$$

$$\hat{\sigma}_{w,k}^{2,(i+1)} = \hat{\sigma}_{w,k-1}^2 + \frac{1-\lambda}{1-\lambda^k} \left\{ \mathbb{E}\left[\left(x_k - \hat{\xi}_k^{(i+1)} x_{k-S} - \hat{\mathbf{a}}_k^{(i+1),\mathrm{T}}\mathbf{z}_{k-1}\right)^2\right] - \hat{\sigma}_{w,k-1}^2 \right\}, \tag{3.32c}$$

75

where $\tilde{\mathbf{M}}_{\mathbf{a},k-1}$ and $\tilde{m}_{\xi,k-1}$ are defined as

$$\tilde{\mathbf{M}}_{\mathbf{a},k-1} := \lambda \tilde{\mathbf{M}}_{\mathbf{a},k-2} + \mathbb{E}[\mathbf{z}_{k-1}\mathbf{z}_{k-1}^{\mathrm{T}}], \tag{3.33a}$$

$$\tilde{m}_{\xi,k-1} := \lambda \tilde{m}_{\xi,k-2} + \mathbb{E}[x_{k-S}^2]. \tag{3.33b}$$

The expectations are performed with respect to $\tilde{f}(x_k, \mathbf{z}_{k-1}, x_{k-S}|\mathbf{y}_0^k, \hat{\mathbf{\Theta}}_k^{(i)})$.

3.4.2.2   Multiple-step-ahead Prediction

Based on the parameter set estimation $\hat{\mathbf{\Theta}}_k$ and the state estimation $\boldsymbol{\mu}_{\mathbf{z},k}$ and $\{\mu_{k'}; k' \leq k\}$ (denoted next also as $\hat{\mathbf{z}}_k$ and $\{\hat{x}_{k'}; k' \leq k\}$, respectively), the m-step-ahead prediction of the latent process and the slowly-varying channel parameter can be obtained recursively as

$$\hat{z}_{k+m} = \hat{\mathbf{a}}_k^{\mathrm{T}} \hat{\mathbf{z}}_{k+m-1}, \tag{3.34a}$$

$$\hat{x}_{k+m} = \hat{z}_{k+m} + \hat{\xi}_k \hat{x}_{k+m-S}, \tag{3.34b}$$

$$\hat{\alpha}_{k+m} = \hat{\gamma}_{0,k} + \hat{x}_{k+m} + \hat{\mathbf{b}}_k^{\mathrm{T}} \mathbf{u}_{k+m}, \tag{3.34c}$$

for $m = 1, \cdots$, where $\mathbf{u}_{k+m}$ can be obtained from meteorological forecast sources, e.g., [61].

3.4.3 Bayesian Filtering and Smoothing

To find the expectations in (3.32) and (3.33), we compute the marginalization of $\tilde{f}(x_k, \mathbf{z}_{k-1}, x_{k-S}|\mathbf{y}_0^k, \hat{\boldsymbol{\Theta}}_k^{(i)})$ with respect to $x_k, \mathbf{z}_k, \mathbf{z}_{k-1}$, and x_{k-S}, respectively. Denote the marginal PDFs as

$$\tilde{f}(x_k|\mathbf{y}_0^k, \hat{\boldsymbol{\Theta}}_k^{(i)}) = \mathcal{N}(\mu_k^{(i)}, \sigma_k^{2,(i)}),$$

$$\tilde{f}(\mathbf{z}_k|\mathbf{y}_0^k, \hat{\boldsymbol{\Theta}}_k^{(i)}) = \mathcal{N}(\boldsymbol{\mu}_{\mathbf{z},k}^{(i)}, \mathbf{C}_{\mathbf{z},k}^{(i)}),$$

$$\breve{f}(\mathbf{z}_{k-1}|\mathbf{y}_0^k, \hat{\boldsymbol{\Theta}}_k^{(i)}) = \mathcal{N}(\breve{\boldsymbol{\mu}}_{\mathbf{z},k-1}^{(i)}, \breve{\mathbf{C}}_{\mathbf{z},k-1}^{(i)}),$$

$$\breve{f}(x_{k-S}|\mathbf{y}_0^k, \hat{\boldsymbol{\Theta}}_k^{(i)}) = \mathcal{N}(\breve{\mu}_{k-S}^{(i)}, \breve{\sigma}_{k-S}^{2,(i)}).$$

Based on $\tilde{f}(\mathbf{z}_{k-1}|\mathbf{y}_0^{k-1}, \hat{\boldsymbol{\Theta}}_{k-1})$, $\tilde{f}(x_{k-S}|\mathbf{y}_0^{k-S}, \hat{\boldsymbol{\Theta}}_{k-S})$, and the model in (3.27), x_k can be predicted and with the prediction MSE,

$$\mu_{k|k-1}^{(i)} = \hat{\mathbf{a}}_k^{(i),\mathrm{T}}\boldsymbol{\mu}_{\mathbf{z},k-1} + \hat{\xi}_k^{(i)}\mu_{k-S},$$

$$\sigma_{k|k-1}^{2,(i)} = \hat{\mathbf{a}}_k^{(i),\mathrm{T}}\mathbf{C}_{\mathbf{z},k-1}\hat{\mathbf{a}}_k^{(i)} + \hat{\xi}_k^{(i),2}\sigma_{k-S}^2 + \sigma_{\mathrm{w},k}^{2,(i)}.$$

Based on the measurement y_k and the measurement model in (3.6b), the mean and

the variance of x_k in the marginal PDF $\tilde{f}(x_k|\mathbf{y}_0^k, \hat{\boldsymbol{\Theta}}_k^{(i)})$ can be formulated as

$$\mu_k^{(i)} = \mu_{k|k-1}^{(i)} + \frac{\sigma_{k|k-1}^{2,(i)}}{\sigma_{\mathrm{v},k}^{2,(i)} + \sigma_{k|k-1}^{2,(i)}}$$

$$\times \left(y_k - \mu_{k|k-1}^{(i)} - \hat{\gamma}_{0,k}^{(i)} - \hat{\mathbf{b}}_k^{(i),\mathrm{T}}\mathbf{u}_k\right), \tag{3.35a}$$

$$\sigma_k^{2,(i)} = \frac{\sigma_{\mathrm{v},k}^{2,(i)}\sigma_{k|k-1}^{2,(i)}}{\sigma_{\mathrm{v},k}^{2,(i)} + \sigma_{k|k-1}^{2,(i)}}. \tag{3.35b}$$

We further have $\mathbb{E}[x_k^2|\hat{\boldsymbol{\Theta}}_k^{(i)}] = \sigma_k^{2,(i)} + (\mu_k^{(i)})^2$.

Similar operation can be applied to $\mathbf{z}_k$. Define $\hat{\mathbf{A}}_k^{(i)}$ and $\hat{\mathbf{C}}_{\mathbf{w},k}^{(i)}$ as the matrix correspond-ing to $\hat{\mathbf{a}}_k^{(i)}$ and $\hat{\sigma}_{w,k}^{2,(i)}$, respectively. Based on $\tilde{f}(\mathbf{z}_{k-1}|\mathbf{y}_0^{k-1}, \hat{\boldsymbol{\Theta}}_{k-1})$, $\mathbf{z}_k$ can be predicted as $\hat{\mathbf{A}}_k^{(i)}\boldsymbol{\mu}_{\mathbf{z},k-1}$, with the prediction MSE matrix $\mathbf{P}_{\mathbf{z},k}^{(i)} = \hat{\mathbf{A}}_k^{(i)}\mathbf{C}_{\mathbf{z},k-1}\hat{\mathbf{A}}_k^{(i),\mathrm{T}} + \hat{\mathbf{C}}_{\mathbf{w},k}^{(i)}$. Note that the measurement y_k can be represented as

$$y_k = \gamma_0 + \mathbf{h}^\mathrm{T}\mathbf{z}_k + \xi x_{k-S} + \mathbf{b}^\mathrm{T}\mathbf{u}_k + v_k.$$

Define the gain vector $\mathbf{k}_{\mathbf{z},k}^{(i)} = \mathbf{P}_{\mathbf{z},k}^{(i)}\mathbf{h}\left(\hat{\xi}_k^{(i),2}\sigma_{k-S}^2 + \hat{\sigma}_{k,v}^{(i)} + \mathbf{h}^\mathrm{T}\mathbf{P}_{\mathbf{z},k}^{(i)}\mathbf{h}\right)^{-1}$. The mean and the covariance matrix of $\mathbf{z}_k$ in the marginal PDF $\tilde{f}(\mathbf{z}_k|\mathbf{y}_0^k, \hat{\boldsymbol{\Theta}}_k^{(i)})$ can be formulated as

$$\boldsymbol{\mu}_{\mathbf{z},k}^{(i)} = \hat{\mathbf{A}}_k^{(i)}\boldsymbol{\mu}_{\mathbf{z},k-1} + \mathbf{k}_{\mathbf{z},k}^{(i)}$$

$$\times \left(y_k - \hat{\mathbf{a}}_k^{(i),\mathrm{T}}\boldsymbol{\mu}_{\mathbf{z},k-1} - \hat{\xi}_k^{(i)}\mu_{k-S} - \hat{\gamma}_{0,k}^{(i)} - \hat{\mathbf{b}}_k^{(i),\mathrm{T}}\mathbf{u}_k\right), \tag{3.36a}$$

$$\mathbf{C}_{\mathbf{z},k}^{(i)} = (\mathbf{I} - \mathbf{k}_{\mathbf{z},k}^{(i)}\mathbf{h}^\mathrm{T})\mathbf{P}_{\mathbf{z},k}^{(i)}. \tag{3.36b}$$

We further have $\mathbb{E}[\mathbf{z}_k \mathbf{z}_k^{\mathrm{T}} | \hat{\boldsymbol{\Theta}}_k^{(i)}] = \mathbf{C}_{\mathbf{z},k}^{(i)} + \boldsymbol{\mu}_{\mathbf{z},k}^{(i)} \boldsymbol{\mu}_{\mathbf{z},k}^{(i),\mathrm{T}}$.

Furthermore, the marginal PDF $\breve{f}(\mathbf{z}_{k-1} | \mathbf{y}_0^k, \hat{\boldsymbol{\Theta}}_k^{(i)})$ can be obtained via the one-step backward smoothing. Denote the gain matrix $\mathbf{J}_{\mathbf{z},k-1}^{(i)} = \mathbf{C}_{\mathbf{z},k-1} \hat{\mathbf{A}}_k^{(i),\mathrm{T}} (\mathbf{P}_{\mathbf{z},k}^{(i)})^{-1}$. The mean and the covariance matrix of $\mathbf{z}_{k-1}$ in the marginal PDF can be formulated as

$$\breve{\boldsymbol{\mu}}_{\mathbf{z},k-1}^{(i)} = \boldsymbol{\mu}_{\mathbf{z},k-1} + \mathbf{J}_{\mathbf{z},k-1}^{(i)} (\boldsymbol{\mu}_{\mathbf{z},k}^{(i)} - \hat{\mathbf{A}}_k^{(i)} \boldsymbol{\mu}_{\mathbf{z},k-1}), \tag{3.37a}$$

$$\breve{\mathbf{C}}_{\mathbf{z},k-1}^{(i)} = \mathbf{C}_{\mathbf{z},k-1} + \mathbf{J}_{\mathbf{z},k-1}^{(i)} (\mathbf{C}_{\mathbf{z},k}^{(i)} - \mathbf{P}_{\mathbf{z},k}^{(i)}) \mathbf{J}_{\mathbf{z},k-1}^{(i),\mathrm{T}}. \tag{3.37b}$$

We further have $\mathbb{E}[\mathbf{z}_{k-1} \mathbf{z}_{k-1}^{\mathrm{T}} | \hat{\boldsymbol{\Theta}}_k^{(i)}] = \breve{\mathbf{C}}_{\mathbf{z},k-1}^{(i)} + \breve{\boldsymbol{\mu}}_{\mathbf{z},k-1}^{(i)} \breve{\boldsymbol{\mu}}_{\mathbf{z},k-1}^{(i),\mathrm{T}}$. Based on the joint PDF $\tilde{f}(x_k, \mathbf{z}_{k-1}, x_{k-S} | \mathbf{y}_0^k, \hat{\boldsymbol{\Theta}}_k^{(i)})$, we also have $\mathbb{E}[\mathbf{z}_k \mathbf{z}_{k-1}^{\mathrm{T}} | \hat{\boldsymbol{\Theta}}_k^{(i)}] = \mathbf{C}_{\mathbf{z},k}^{(i)} \mathbf{J}_{\mathbf{z},k-1}^{(i),\mathrm{T}} + \boldsymbol{\mu}_{\mathbf{z},k}^{(i)} \breve{\boldsymbol{\mu}}_{\mathbf{z},k-1}^{(i),\mathrm{T}}$.

Given $\tilde{f}(x_{k-S} | \mathbf{y}_0^{k-S}, \hat{\boldsymbol{\Theta}}_{k-S})$, $\tilde{f}(\mathbf{z}_{k-1} | \mathbf{y}_0^{k-1}, \hat{\boldsymbol{\Theta}}_{k-1})$, and the measurement representation,

$$y_k = \gamma_0 + \mathbf{a}^{\mathrm{T}} \mathbf{z}_{k-1} + \xi x_{k-S} + \mathbf{b}^{\mathrm{T}} \mathbf{u}_k + w_k + v_k,$$

the mean and the variance in the marginalized PDF $\breve{f}(x_{k-S} | \mathbf{y}_0^k, \hat{\boldsymbol{\Theta}}_k^{(i)})$, can be formulated as

$$\breve{\mu}_{k-S}^{(i)} = \mu_{k-S} + \frac{\hat{\xi}_k^{(i)} \sigma_{k-S}^2 \left(y_k - \hat{\mathbf{a}}_k^{(i),\mathrm{T}} \boldsymbol{\mu}_{\mathbf{z},k-1} - \hat{\xi}_k^{(i)} \mu_{k-S} - \hat{\gamma}_{0,k}^{(i)} - \hat{\mathbf{b}}_k^{(i),\mathrm{T}} \mathbf{u}_k \right)}{\hat{\mathbf{a}}_k^{(i),\mathrm{T}} \mathbf{C}_{\mathbf{z},k-1} \hat{\mathbf{a}}_k^{(i)} + \sigma_{\mathrm{w},k}^{2,(i)} + \sigma_{\mathrm{v},k}^{2,(i)} + \hat{\xi}_k^{2,(i)} \sigma_{k-S}^2}, \tag{3.38a}$$

$$\breve{\sigma}_{k-S}^{2,(i)} = \frac{(\hat{\mathbf{a}}_k^{(i),\mathrm{T}} \mathbf{C}_{\mathbf{z},k-1} \hat{\mathbf{a}}_k^{(i)} + \sigma_{\mathrm{w},k}^{2,(i)} + \sigma_{\mathrm{v},k}^{2,(i)}) \sigma_{k-S}^2}{\hat{\mathbf{a}}_k^{(i),\mathrm{T}} \mathbf{C}_{\mathbf{z},k-1} \hat{\mathbf{a}}_k^{(i)} + \sigma_{\mathrm{w},k}^{2,(i)} + \sigma_{\mathrm{v},k}^{2,(i)} + \hat{\xi}_k^{2,(i)} \sigma_{k-S}^2}. \tag{3.38b}$$

We further have $\mathbb{E}[x_{k-S}^2|\hat{\boldsymbol{\Theta}}_k^{(i)}] = \check{\sigma}_{k-S}^{2,(i)} + (\check{\mu}_{k-S}^{(i)})^2$.

The expectations to be used in (3.32) and (3.33) can be directly extracted from the above results. In particular, given (3.24), the expectation $\mathbb{E}[x_k x_{k-S}|\hat{\boldsymbol{\Theta}}_k^{(i)}]$ can be computed based on $\mathbb{E}[z_k^2|\hat{\boldsymbol{\Theta}}_k^{(i)}]$, $\mathbb{E}[x_k^2|\hat{\boldsymbol{\Theta}}_k^{(i)}]$ and $\mathbb{E}[x_{k-S}^2|\hat{\boldsymbol{\Theta}}_k^{(i)}]$. Note that x_{k-S} and $(\mathbf{a}^{\mathrm{T}}\mathbf{z}_{k-1})$ are independent. We have $\mathbb{E}[x_{k-S}(\mathbf{a}_k^{(i),\mathrm{T}}\mathbf{z}_{k-1})|\hat{\boldsymbol{\Theta}}_k^{(i)}] = \check{\mu}_{k-S}^{(i)}(\mathbf{a}_k^{(i),\mathrm{T}}\check{\boldsymbol{\mu}}_{\mathbf{z},k-1}^{(i)})$.

3.5 Model Order Selection

The non-seasonal latent process in (3.4) can be regarded as a degraded seasonal latent process in (3.22) with a seasonal order of zero. The orders (P, P_{se}) and the index set $\mathcal{I}$ of N_u important elements within $\mathcal{E}[k], \forall k$ for the process $\{g_k\}$, can be determined via the the minimum description length (MDL) criterion [62], as described in the following.

We stack the channel measurements $\{y[k]\}$ into a long vector $\mathbf{y}$ of length K. Stack the coefficients of the seasonal $\mathrm{AR}(P_{\mathrm{se}})$ process into a vector $\boldsymbol{\xi} := [\xi_1, \cdots, \xi_{P_{\mathrm{se}}}]^{\mathrm{T}}$ (c.f. (3.22)). Define a long vector $\boldsymbol{\theta} := \left([1 \ \mathbf{a}^{\mathrm{T}}] \otimes [1 \ \boldsymbol{\xi}^{\mathrm{T}}]\right)^{\mathrm{T}}$ of length $(P+1) \times (P_{\mathrm{se}}+1)$ and with $\otimes$ denoting the Kronecker product.
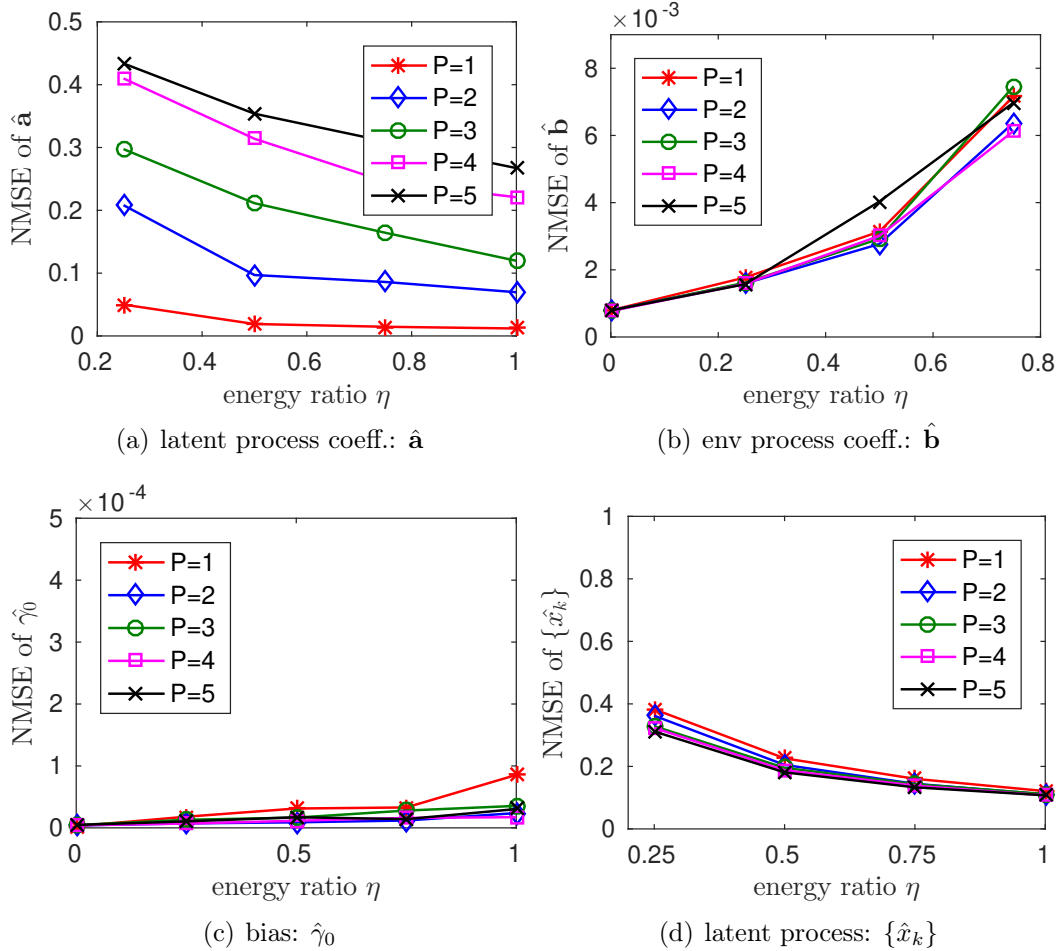
Figure 3.3: Non-seasonal channels: Normalized mean square estimation error of the model parameters and the latent process.

Based on (3.5) and (3.22), we have

$$\mathbf{y} = \mathbf{H}(\gamma_0, \mathbf{b})\boldsymbol{\theta} + \mathbf{n}, \qquad (3.39)$$

where $\mathbf{H}(\gamma_0, \mathbf{b})$ is a matrix containing unknown parameters, and its kth row is formed by γ_0, $\{y[k']; k' < k\}$ according to (P, P_{se}), and by the elements in $\{\mathcal{E}[k']; k' \leq k\}$ that are indexed by $\mathcal{I}$ and weighed by $\mathbf{b}$, and $\mathbf{n}$ is a noise vector, with $n[k] \sim \mathcal{N}(0, \sigma_n^2)$.
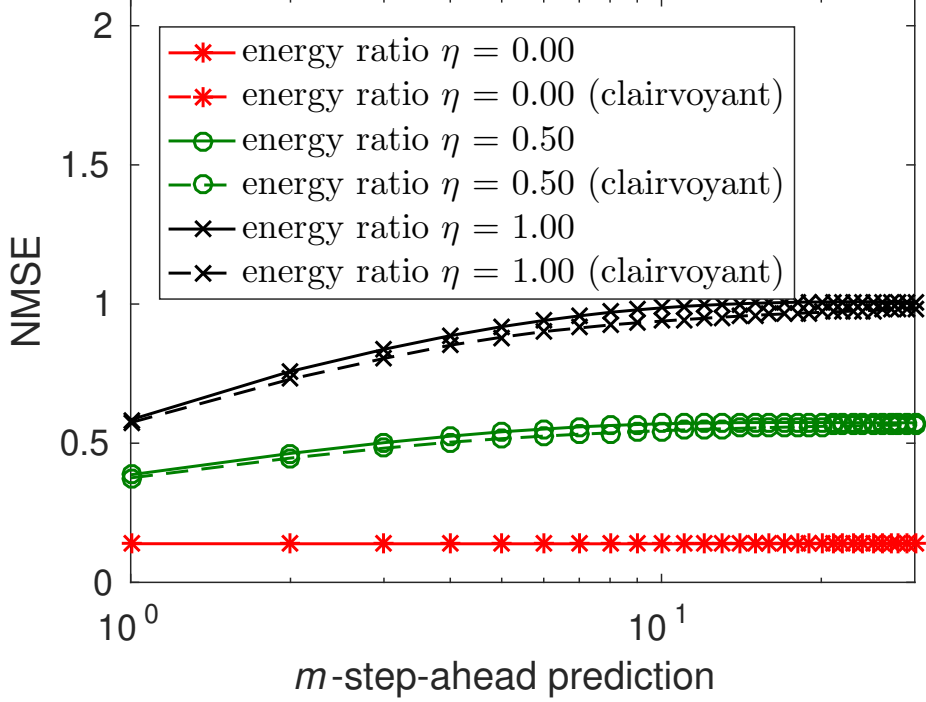
Figure 3.4: Non-seasonal channels: Prediction performance with the channel generation knowledge. Clairvoyant: the Kalman filter performance with perfect knowledge of model parameters.

The optimal values of (P, P_{se}) and the index set $\mathcal{I}$ can be determined according to the MDL criterion [62],

$$\min_{(P, P_{\text{se}}, \mathcal{I})} \quad \frac{K}{2} \ln \hat{\sigma}_n^2 + \frac{1}{2}(P + P_{\text{se}} + N_u) \ln K, \tag{3.40}$$

where $\hat{\sigma}_n^2 = \frac{1}{K}\mathbf{y}^{\text{T}}\mathbf{P}^{\perp}(\hat{\gamma}_0, \hat{\mathbf{b}})\mathbf{y}$ is the ML estimation of the noise variance, with $\mathbf{P}^{\perp}(\hat{\gamma}_0, \hat{\mathbf{b}}) := \mathbf{I} - \mathbf{H}(\hat{\gamma}_0, \hat{\mathbf{b}})(\mathbf{H}^{\text{T}}(\hat{\gamma}_0, \hat{\mathbf{b}})\mathbf{H}(\hat{\gamma}_0, \hat{\mathbf{b}}))^{-1}\mathbf{H}^{\text{T}}(\hat{\gamma}_0, \hat{\mathbf{b}})$, and $(P + P_{\text{se}} + N_u)$ is the number of model parameters. The ML estimation $\hat{\gamma}_0$ and $\hat{\mathbf{b}}$ can be found based on (3.39) by iterative computational methods. In real applications, consider that the large-scale phenomena of water environments change very slowly. The model order

selection can be carried out once in a while by a central processing station, after it collects the measured slowly-varying channel parameters from underwater nodes. Given small values of (P, P_{se}) and limited types of environmental parameters, the optimization problem in (3.40) can be solved via exhaustive search.

3.6 Simulation Results

The proposed recursive algorithms are evaluated via Monte Carlo simulations. In each simulation setting, we consider 400 Monte Carlo runs, and each run contains a time series of a slowly-varying channel parameter of 3000 samples. The time series is generated according to the model specified in (3.6). In each Monte Carlo run, the time-invariant component γ_0 is randomly selected uniformly from $[3, 30]$. The latent processes in non-seasonal channels are generated as $\mathrm{AR}(P)$ processes according to (3.4), while the latent processes in seasonal channels are generated as multiplicative seasonal AR processes $(\mathrm{AR}(P) \times (1)_{96})$ according to (3.23), with the seasonal coefficient ξ randomly selected uniformly from $[-1, 1]$. Two types of environmental parameters are considered. The time sequences of environmental parameters are generated independently as $\mathrm{AR}(P)$ processes. The AR coefficients of each process are obtained based on a minimum-phase polynomial whose roots are randomly chosen within the unit circle in the complex plane. The process $\{g_k\}$ is generated as a linear combination of the time sequences of the two types of environmental parameters

(a) energy ratio $\eta = 0$ (b) energy ratio $\eta = 0.5$ (c) energy ratio $\eta = 1$
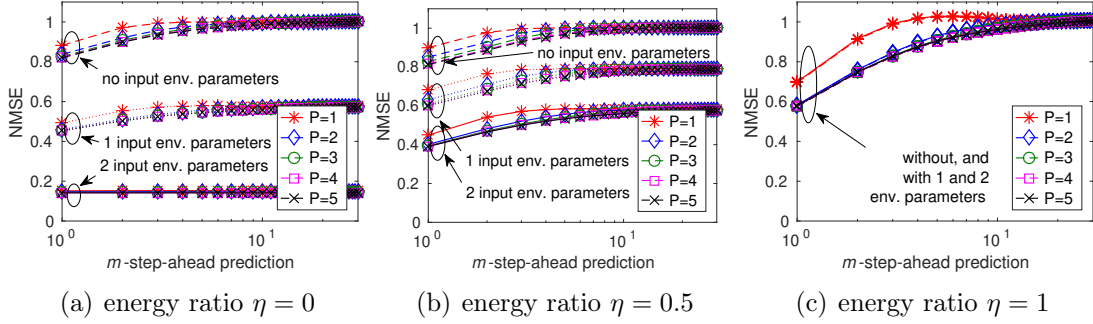
Figure 3.5: Non-seasonal channels: Prediction performance without the channel generation knowledge. $P = 2$.

$\phi_i[k]$,

$$g[k] = \sum_{l=1}^{L=2} b_l \phi_l[k]. \tag{3.41}$$

The combinational coefficients in $\mathbf{b} = [b_1, b_2]^{\mathrm{T}}$ are randomly selected according to a uniform distribution over $[0.2, 1] \times \zeta$, where ζ is a scalar for controlling the energy ratio between the process $\{g_k\}$ and the latent process $\{x_k\}$. Specifically, we define the energy ratio

$$\eta := \frac{\sum_{k=1}^{K} x_k^2}{\sum_{k=1}^{K} (x_k^2 + g_k^2)}, \tag{3.42}$$

to control the contribution of the latent process $\{x_k\}$ and the contribution of the process $\{g_k\}$ in the generated time series $\{\alpha_k\}$, with $K = 3000$. When $\eta = 1$, the sequence $\{\alpha_k\}$ only consists of γ_0 and the latent process. When $\eta = 0$, the sequence $\{\alpha_k\}$ only consists of γ_0 and the process $\{g_k\}$. The value of ζ can be computed based on a pre-selected value of η. The energy ratio between the summed process $\{x_k + g_k\}$ and the measurement noise is set to a moderate value of 8 dB.

The normalized mean square error (NMSE) is taken as the performance metric, which

84
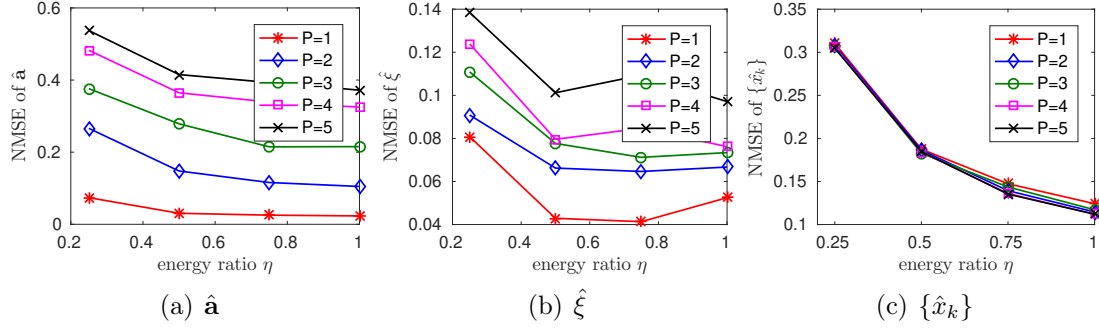
Figure 3.6: Seasonal channels: Normalized mean square estimation error of the model parameters and the latent process.

is computed after the convergence of the model parameter estimation. Specifically, for vector $\mathbf{a}$, the estimation NMSE is computed as

$$\frac{1}{N} \sum_{k=k_0}^{K} \frac{\|\mathbf{a} - \hat{\mathbf{a}}_k\|_2^2}{\|\mathbf{a}\|_2^2}, \tag{3.43}$$

where $\hat{\mathbf{a}}_k$ is the estimation at time k, k_0 is the time index when the estimation converges, $N := (K - k_0 + 1)$, and $\|\cdot\|_2$ denotes the ℓ_2 norm. The estimation NMSE of other model parameters can be similarly computed. The estimation NMSE of the latent process is computed as

$$\frac{\frac{1}{N} \sum_{k=k_0}^{K} (x_k - \hat{x}_k)^2}{\frac{1}{N} \sum_{k=k_0}^{K} x_k^2}. \tag{3.44}$$

The NMSE of the m-step-ahead prediction of the slowly-varying channel parameter is computed as

$$\frac{\frac{1}{N-m} \sum_{k=k_0}^{K-m} (\alpha_{k+m} - \hat{\alpha}_{k+m})^2}{\frac{1}{N} \sum_{k=k_0}^{K} (\alpha_k - \bar{\alpha})^2}, \tag{3.45}$$

85

with $\bar{\alpha}$ being the average of the sequence $\{\alpha_k\}$. In the proposed algorithm for non-seasonal channels and for seasonal channels, the forgetting factor is set as $\lambda = 0.99$. The proposed algorithms in all the simulation settings converge within about $k_0 = 800$ time steps.

3.6.1 Non-seasonal Channels

The recursive algorithm for non-seasonal channels will be evaluated in two scenarios. The first scenario assumes perfect prior knowledge of the latent process order P and has access to both types of environmental parameters, while the second scenario does not assume the prior knowledge of the latent process order and may not have access to all the environmental parameters. The second scenario is closer to real world applications.

3.6.1.1 Modeling and Prediction with Channel Generation Knowledge

The proposed recursive algorithm is evaluated using the sequences of $\{\alpha_k\}$ that are generated according to different latent process orders and different values of the energy ratio η. The estimation NMSEs of $\mathbf{a}$, $\mathbf{b}$, γ_0 and the latent process are depicted in Fig. 3.3. One can see that as the energy ratio η increases, the estimation NMSE of $\mathbf{a}$ and of the latent process decreases, while the estimation NMSE of $\mathbf{b}$ increases. In

addition, as the latent process order P increases, the estimation NMSE of $\mathbf{a}$ increases drastically, whereas the estimation NMSEs of $\mathbf{b}$, γ_0 and the latent process are less sensitive to the order change. The vector $\mathbf{b}$ and the time-invariant component γ_0 can be accurately estimated with the NMSE less than 10^{-2} and 10^{-4}, respectively.

Corresponding to the latent process order $P = 2$ and different values of the energy ratio η, Fig. 3.4 depicts the m-step-ahead prediction performance of the proposed algorithm. As a performance upper bound, the m-step-ahead prediction NMSE of the Kalman filter with perfect knowledge of the model parameters is also plotted. One can observe that the proposed algorithm achieves a performance very close to the performance upper bound. Additionally, the prediction accuracy improves as the contribution of the latent process decreases (i.e., as η decreases). In other words, the channel can be more accurately modeled and predicted when it has less contribution from unknown physical mechanisms or unavailable environmental parameters.

3.6.1.2   Modeling and Prediction without Channel Generation Knowledge

We generate the sequences of $\{\alpha_k\}$ according to the latent process order $P = 2$ and different values of the energy ratio η. Without the knowledge of $P = 2$ and potentially in lack of one or both types of environment parameters, the m-step-ahead prediction performance of the proposed algorithm is shown in Fig. 3.5, where different orders of the latent process are examined for channel modeling and prediction. One can see
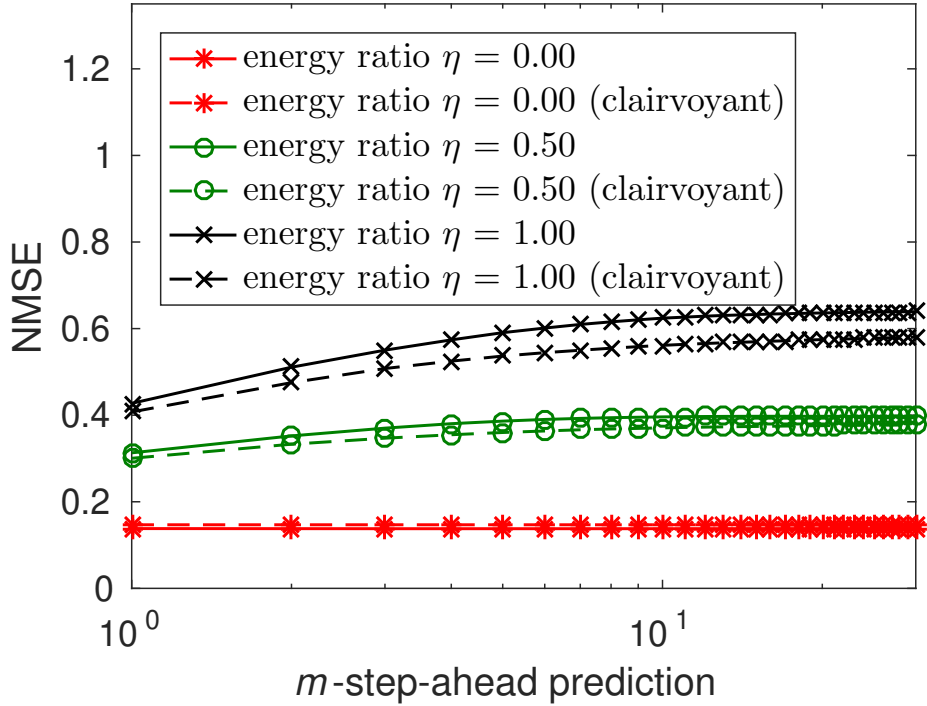
Figure 3.7: Seasonal channels: Prediction performance with the channel generation knowledge. Clairvoyant: the Kalman filter performance with perfect knowledge of model parameters.

(a) energy ratio $\eta = 0$

(b) energy ratio $\eta = 0.5$

(c) energy ratio $\eta = 1$
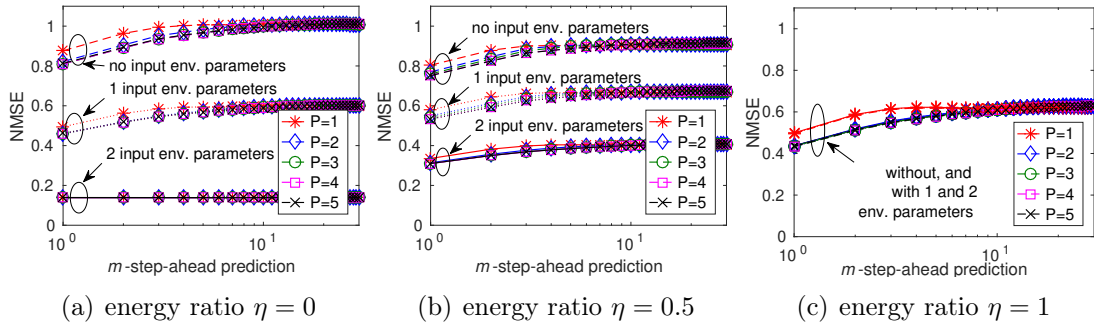
Figure 3.8: Seasonal channels: Prediction performance without the channel generation knowledge. $P = 2$.

that the prediction performance improves when more environmental parameters are incorporated and when the contribution of the latent process decreases. Furthermore, for each energy ratio, performance improvement can be observed when the order of the latent process increases from 1 to the true value of 2, while the improvement

is less obvious for further increase. Additionally, when the energy ratio equals to one, namely, the sequence $\{\alpha_k\}$ only consists of the time-invariant component γ_0 and the latent process, incorporation of the environmental parameters into the channel modeling does not lead to obvious performance degradation.

3.6.2 Seasonal Channels

Following the seasonality in the KW-AUG14 experiment, we consider a seasonal cycle of $S = 96$. We next evaluate the proposed algorithm for seasonal channels with and without the channel generation knowledge.

3.6.2.1 Modeling and Prediction with Channel Generation Knowledge

For the sequences of $\{\alpha_k\}$ with different values of P and different values of η, the estimation NMSEs of $\mathbf{a}$, ξ and the latent process are depicted in Fig. 3.6. The estimation NMSEs of $\mathbf{b}$, γ_0 are almost identical to those in Fig. 3.3 for non-seasonal channels. Comparing the NMSEs in Figs. 3.3 and 3.6, one can see that the estimation NMSE of $\mathbf{a}$ in seasonal channels is larger than that in non-seasonal channels, primarily because of the nonlinear relationship between $\mathbf{a}$ and ξ. Furthermore, the estimation NMSE of the latent process in seasonal channels is less than that in non-seasonal channels, thanks to the seasonal correlation of the latent process.

(a) average channel SNR

(b) Nakagami-m fading parameter

(c) average RMS delay spread

(d) average RMS Doppler spread
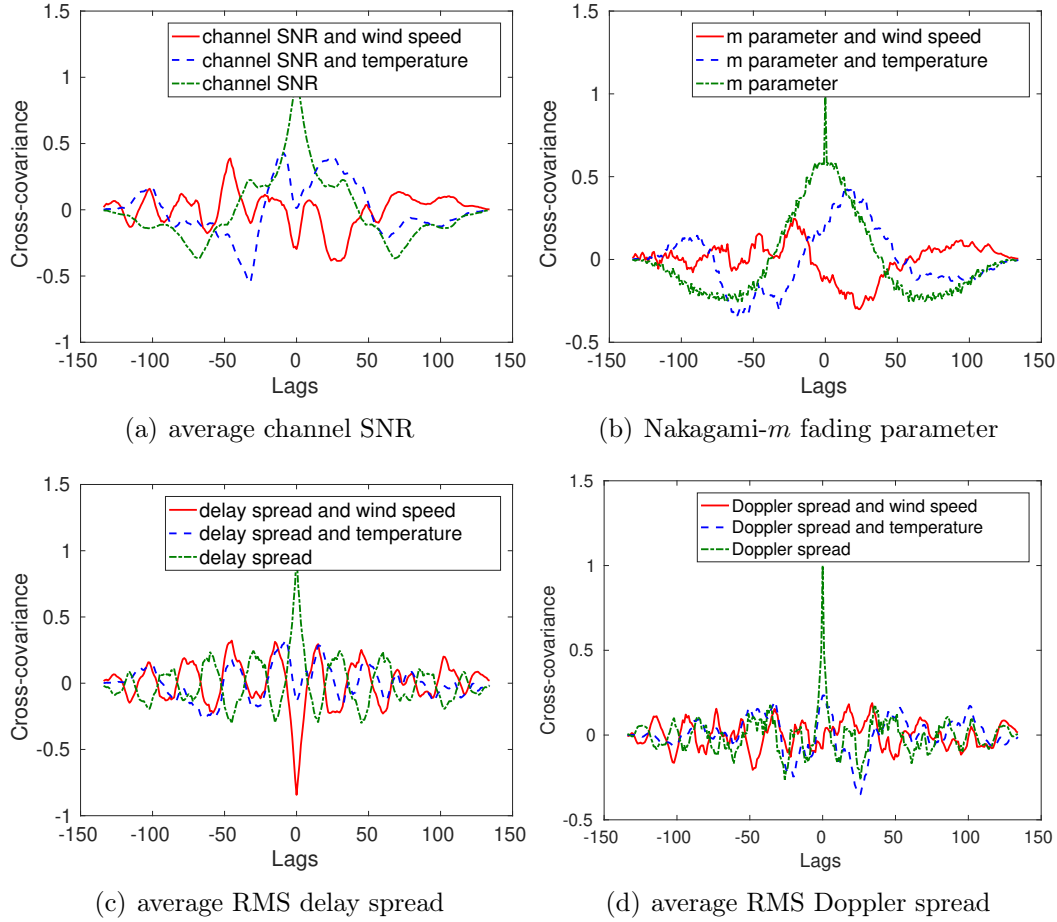
Figure 3.9: SPACE08: Autocorrelation of slowly-varying channel parameters and their correlation with environmental measurements.

Corresponding to $P = 2$ and different values of the energy ratio η, Fig. 3.7 shows the m-step-ahead prediction performance of the proposed algorithm. As a performance upper bound, the m-step-ahead prediction NMSE of the Kalman filter with perfect knowledge of the model parameters is also plotted. One can obtain similar observations as those in non-seasonal channels. However, compared to the simulation results in Fig. 3.4, less NMSE can be achieved in the seasonal channel, benefiting from the seasonal correlation of the latent process.

3.6.2.2   Modeling and Prediction without Channel Generation Knowledge

We generate the sequences of $\{\alpha_k\}$ in seasonal channels with $P = 2$ and different values of the energy ratio η. Without the knowledge of $P = 2$ and potentially in the lack of one or both types of environmental parameters, the m-step-ahead prediction performance of the proposed algorithm is shown in Fig. 3.8, where different values of P are examined. Compared to Fig. 3.5, similar observations can be obtained, while as the energy ratio η increases, higher prediction accuracy can be achieved in the seasonal channel, benefiting from the seasonal correlation of the latent process.

3.7   Experimental Data Processing

The proposed models and algorithms are evaluated using measurements from two shallow-water field experiments: one is the Surface Processes and Acoustic Communication Experiment (SPACE08) conducted from Oct. 14 to Nov. 1, 2008 near the coast of Martha's Vineyard, MA, and the other was conducted in the Keweenaw Waterway, MI in Aug. 2014, abbreviated as KW-AUG14. In SPACE08, a waveform of 1 minute and within the frequency band $[8, 18]$ kHz was transmitted every 2 hours at a fixed power level. The waveform consists of 60 ZP OFDM-modulated blocks with parameters specified in Table 2.1. In KW-AUG14, a waveform of 8.83 seconds

and within the frequency band $[14, 20]$ kHz was transmitted every 15 minutes at a fixed power level. The waveform consists of 20 ZP OFDM-modulated blocks with parameters specified in Table 2.1. The CIR is estimated per OFDM block based on measurements at pilot subcarriers using a sparse channel estimator which exploits the multipath sparsity in the delay and the Doppler domain [25]. Four types of slowly-varying channel parameters derived from the estimated CIRs are examined in this section, including the average channel SNR, the Nakagami-m fading parameter, the average RMS delay spread, and the average RMS Doppler spread (c.f. Section 2.2.1). While many environmental parameters have impact on UWA channels, the wind speed and temperature are chosen in this Chapter to evaluate the proposed algorithms based on their availability and low acquisition cost. In addition, noticing that the water condition in KW-AUG14 was calm with negligible Doppler effect, we skip the analysis of the average RMS Doppler spread in this experiment.

For performance comparison, we introduce a recursive linear regression (LR) method where the time sequence of a slowly-varying channel parameter is modeled as the summation of a time-invariant component γ_0 and a process $\{g_k\}$ described by environmental measurements defined as in (3.41); see *Remark 3* in Section 3.3.2.

(a) average channel SNR

(b) Nakagami-m fading parameter

(c) average RMS delay spread

(d) average RMS Doppler spread
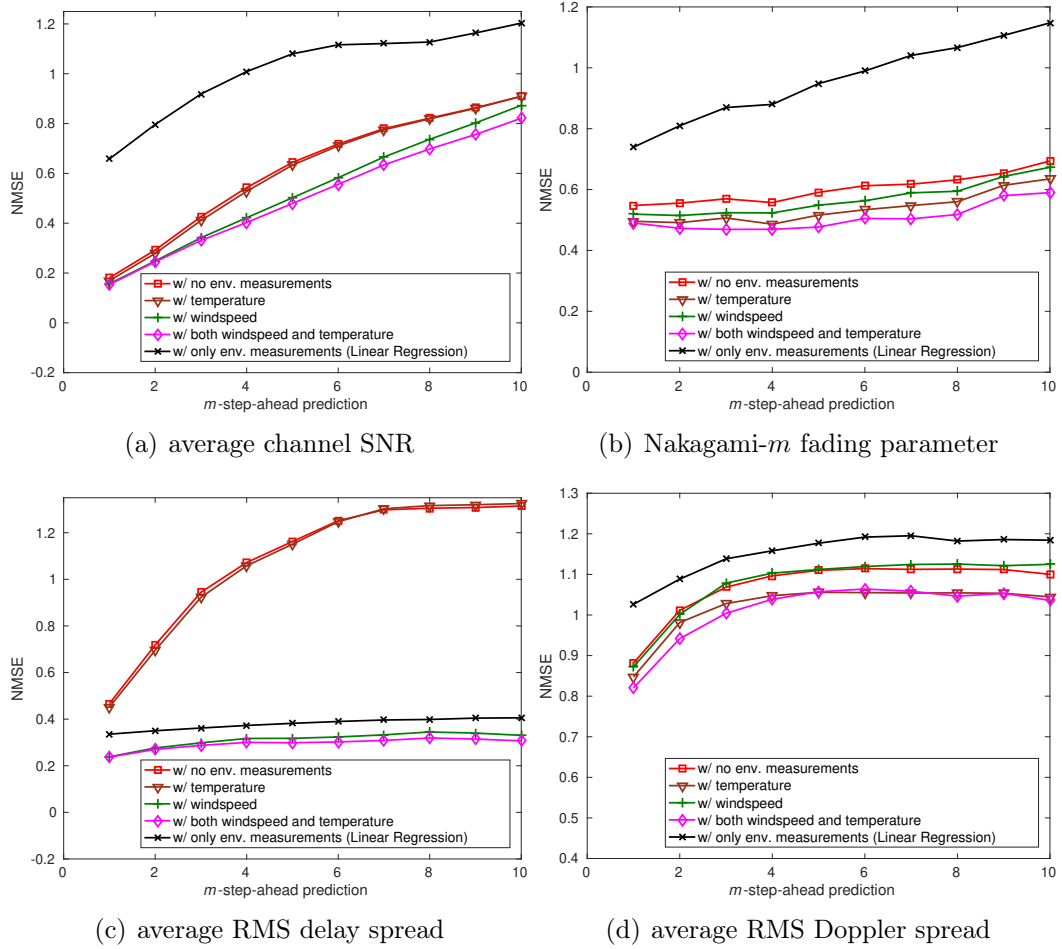
Figure 3.10: SPACE08: Prediction performance of the proposed algorithm and the recursive LR in non-seasonal channels.

3.7.1 SPACE08 with Non-seasonal Channel Variations

In SPACE08, we consider the signals received by a 12-element hydrophone array, which was vertically mounted on a fixed tripod 200 meters away from the source. The adjacent elements have a 12 cm spacing and the top element is 3.25 meters above the sea floor. The water depth is about 15 meters. The source transducer was

Table 3.1
The estimated model parameters.

Slowly-varying channel parameter	$\hat{\mathbf{a}}$	$\hat{\xi}$	$\hat{\mathbf{b}}$ ([wind speed, temperature])	$\hat{\gamma}_0$	η
SPACE08: Channel SNR	0.967	-	[-1.189, -0.206]	12.503	0.828
SPACE08: m fading parameter	[0.153,0.197,0.251,0.189]	-	[-0.0004, 0.0005]	7.99	0.989
SPACE08: RMS delay spread	0.759	-	[-0.411, -0.039]	2.204	0.235
SPACE08: RMS Doppler spread	[0.267,0.130]	-	[0.010, 0.013]	0.748	0.952
KW-AUG14: Channel SNR	0.908	0.068	[-0.098, -0.145]	23.486	0.513
KW-AUG14: m fading parameter	[0.593,0.148,0.145]	-0.013	[-0.193, -0.142]	5.96	0.391
KW-AUG14: RMS delay spread	[0.259,0.224]	0.061	[0.006, 0.006]	1.296	0.976

mounted 4 meters above the bottom. The average channel SNR scaled by the transmission power, the Nakagami-m fading parameter, the average RMS delay spread, and the average RMS Doppler spread within each transmission and over the 12 hydrophones are shown in Fig. 2.6, along with the mean wind speed and the mean air temperature measurements measured respectively by a 3-axis sonic anemometer and a VaiPTU located at 12.5 meters above the mean sea level on the meteorological mast of the Martha's Vineyard Coastal Observatory (MVCO) [63]. The autocorrelation of the slowly-varying channel parameters and their correlation with environmental measurements are depicted in Fig. 3.9. One can see that the average channel SNR and the average RMS delay spread are negatively correlated with the wind speed and their correlation with the temperature are not obvious. The Nakagami-m fading parameter exhibits high inherent temporal correlation, and slight positive correlation with the temperature and slight negative correlation with the wind speed. The average RMS Doppler spread shows slight positive correlation with the temperature and negligible correlation with the wind speed.

In the proposed algorithm, we set the forgetting factor $\lambda = 0.96$ for the average

(a) average channel SNR   (b) Nakagami-m fading parameter   (c) average RMS delay spread
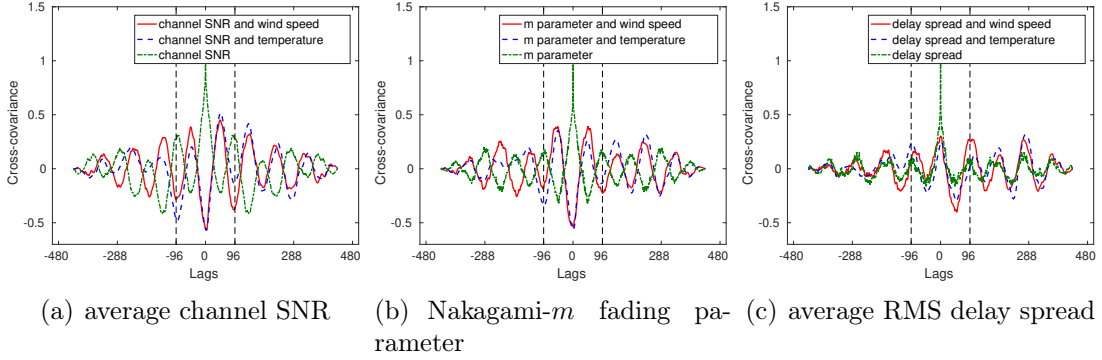
Figure 3.11: KW-AUG14: Autocorrelation of slowly-varying channel parameters and their correlation with environmental measurements.

channel SNR sequence, $\lambda = 0.92$ for the Nakagami-m parameter sequence, and $\lambda = 1$ for the sequences of other slowly-varying channel parameters. According to the MDL criterion in (3.40), the optimal order of the latent process is chosen as $P = 1$ for the sequences of the average channel SNR and the average RMS delay spread, $P = 2$ for the sequence of the average RMS Doppler spread, and $P = 4$ for the sequence of the Nakagami-m fading parameter. In addition, the sequences of the wind speed and the temperature are normalized individually to have a unit power, and a linear combination of the two types of environmental parameters will be used for modeling the process $\{g_k\}$ (c.f. (3.2)). With the incorporation of both types of environmental measurements into the modeling, the model parameters estimated by the proposed algorithm are listed in Table 3.1. The estimated coefficients in $\hat{\mathbf{b}}$ indicate the amount of contribution from each type of environmental parameters, and the value of η reveals the energy ratio between the estimated latent process $\{\hat{x}_k\}$ and the summed process $\{\hat{x}_k + \hat{g}_k\}$.

(a) average channel SNR (b) Nakagami-m fading parameter (c) average RMS delay spread

Figure 3.12: KW-AUG14: Prediction performance of several algorithms in seasonal channels.

The prediction performance of the proposed algorithm and the recursive LR are shown in Fig. 3.10. Specifically, the proposed algorithm with the incorporation of both types of environmental measurements achieves the best performance for all the four types of slowly-varying channel parameters. For the average channel SNR and the Nakagami-m fading parameter, the proposed algorithm outperforms considerably the recursive LR by introducing the latent process to model the temporal variation caused by unknown physical mechanisms. About the average RMS delay spread, thanks to its high correlation with the wind speed, the recursive LR achieves a good performance and outperforms the proposed algorithm without the incorporation of environmental measurements. About the average RMS Doppler spread, due to its fast decaying autocorrelation and limited correlation with environmental measurements, its prediction performance is not as good as the other three types of channel parameters.

3.7.2 KW-AUG14 with Seasonal Channel Variations

In KW-AUG14, the transmission waveform was received by an acoustic modem located 312 meters away from the source. The acoustic modem has 4 hydrophones which are fixed at the vertexes of a horizontal square with 7 cm side length. The water depth of the experimental area varies from 3 to 6 meters. The average channel SNR scaled by the transmission power, the Nakagami-m fading parameter, and the average RMS delay spread within each transmission and over 4 hydrophones are depicted in Fig. 2.4, along with the wind speed and the temperature measurement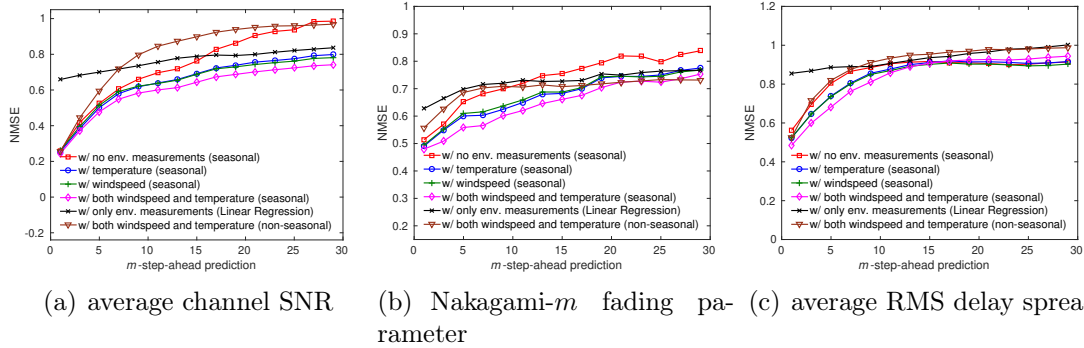s obtained from the Weather Underground [61]. The autocorrelation of those slowly-varying channel parameters and their correlation with environmental measurements are shown in Fig. 3.11. It can be seen that both the average channel SNR and the Nakagami-m fading parameter have high negative correlation with both the wind speed and the temperature, while the average RMS delay spread exhibits positive correlation with both types of environmental measurements. In addition, the sequences of all the three types of slowly-varying channel parameters exhibit a seasonal cycle of 96 (24 hours).

In the proposed algorithm, we set the forgetting factor $\lambda = 1$ for all the three types of slowly-varying channel parameters. According to the MDL criterion in (3.40), the optimal orders of the latent process are chosen as $P = 1$ and $P_{\mathrm{se}} = 1$ for the average

channel SNR and the Nakagami-m fading parameter, and $P = 2$ and $P_\mathrm{se} = 1$ for the average RMS delay spread. In addition, the sequences of the wind speed and the temperature are normalized individually to have a unit power, and a linear combination of the two types of environmental parameters will be used for modeling the process $\{g_k\}$ (c.f. (3.2)). With the incorporation of both types of environmental measurements into the modeling, the estimated model parameters are listed in Table 3.1.

The prediction performance of the average channel SNR, the Nakagami-m fading parameter, and the average RMS delay spread are shown in Fig. 3.12. For comparison, the algorithm proposed for non-seasonal channels is also evaluated, where the latent process is modeled as an $\mathrm{AR}(P)$ process without considering the seasonality. It can be observed that the proposed algorithm for seasonal channels achieves the best performance when both types of environmental measurements are incorporated. Additionally, as the wind speed and the temperature have similar cross-correlation with the sequences of the three slowly-varying channel parameters (c.f. Fig. 3.11), similar performances are obtained when either type of the environmental measurements is incorporated into the modeling. Furthermore, compared to the model and the algorithm proposed for non-seasonal channels, the proposed model and algorithm for seasonal channels achieve superior performance by explicitly modeling the channel seasonality and correspondingly exploiting the seasonality for prediction.

3.8 Summary

This Chapter studied the online modeling and prediction of slowly-varying locally-averaged channel parameters over a long term, by exploiting their inherent temporal correlation and correlation with environmental conditions. From a data-driven perspective, the temporal evolution of a slowly-varying channel parameter of interest was modeled as the summation of a time-invariant component, a process that can be explicitly represented by available and relevant environmental parameters, and a Markov latent process that describes the contribution from unknown or unmeasurable physical mechanisms. A recursive algorithm was developed to estimate the unknown model parameters based on sequentially collected channel measurements and environmental parameters during real-time system operations. The updated model allows multiple-step-ahead prediction of the slowly-varying channel parameter, which could then guide higher-level proactive adaptation of communication strategies to the channel dynamics. The proposed model and the recursive algorithm were extended to seasonal channels by introducing a multiplicative seasonal AR process to model the channel seasonal correlation. Simulations and data sets from two shallow-water experiments were used to validate the effectiveness of the proposed models and algorithms. The experimental data processing revealed that the average channel SNR, the Nakagami-m fading parameter, and the average RMS delay spread can be reasonably well predicted. In addition, superior modeling and prediction performance

can be achieved by exploiting the seasonal correlation in seasonal channels. With the predicted short-term channel quality, the algorithm can be applied in applications of transmission planning. Readers are referred to [64] for details of an application of this algorithm in a reinforcement learning-based adaptive point-to-point transmission scheduling scheme.

Chapter 4

Distributed AUV Tracking and Sound Speed Estimation in Mobile Acoustic Networks with Sound Stratification[1]

4.1   Introduction

Autonomous underwater vehicles (AUVs) have been extensively used for ocean and inland lake exploration, oil and gas drilling, and environment monitoring [65], particularly in deep sea and ice-covered regions. Due to the large attenuation of radio signals

---

[1]The work in this chapter has been submitted to "*IEEE Open Journal of the Communication Society*" ©2019 IEEE.

in water, acoustics are typically used for underwater wireless information transfer and AUV navigation control. The water medium can be inhomogeneous and the sound speed varies depending on environmental parameters, e.g., the temperature, pressure and salinity, particularly in deep water and under-ice environments. Figure 2.12 illustrates obvious spatial variation of the sound speed in the Lake Superior [2]. The sound stratification effect causes refraction of acoustic waves, leading to non-straight line sound propagation and the convergence of acoustic energy in some regions while shadowing in other regions.

The knowledge of sound speed in the area of interest is critical for AUVs to make informative navigational decisions and choose appropriate acoustic communication strategies. In this Chapter, a distributed algorithm is developed for joint sound speed estimation and AUV tracking, based on acoustic measurements collected by AUVs as they maneuver underwater[2]. The acoustic measurements used in this Chapter are the time-of-flight (TOF) of acoustic signals between two AUVs. Given the impact of varying sound speed on the acoustic propagation, the sound speed estimation cannot be separated from AUV localization and tracking. The sound speed estimation requires AUV locations, and AUV localization and tracking requires the sound speed information to convert the TOF measurements into distance measures.

---

[2]It is often inefficient for an AUV to measure the sound speed field online, as it needs to derail from the pre-defined routes and navigate through the whole water column, which consumes significant amount of time and energy.

Traditional treatment for sound speed inversion belongs to the field of ocean tomography, where matched field processing (MFP) techniques dominate [66, 67]. Usually, MFP requires a "forward" acoustic propagation model, e.g. normal mode model, to synthesize the acoustic field or other acoustic features with tentative sound speed parameter and/or other parameters of interest such as source location. The parameters of interest are tuned to match the resulting acoustic features with observations, which are usually obtained through vertically aligned array (VLA). The work in [68] models the sound speed profile with empirical orthogonal functions (EOFs), and estimates the sound speed coefficients by MFP technique. Field pressure and sound speed measurement observations from a hydrophone array are used by [69], and takes the modes and sound speed profile as the state. This information is used to identify the condition for observability of the system and to estimate the sound speed in a simulated environment assuming the observable conditions are met. The work in [70] tracks the sound speed EOF coefficients with sequential measurements, where the unscented Kalman filter (UKF) is adopted and a vertical aligned hydrophone array is set to measure the sound pressure field generated from a fixed source. An inversion method for a range-dependent sound speed field is proposed in [71]. The sound speed field is modeled as horizontally tracked piece-wise sound speed profiles, which is a linear combination of the EOFs. Ensemble Kalman filtering (EnKF) algorithm is adopted to track the sound speed field. The works in [72] and [73] parameterize the sound speed with basis expansion methods and estimate the coefficients of the sound

speed basis functions through minimizing the difference between multipath arrival time observations and theoretical computations. Accuracy of these methods depends on the resolution of the multipath arrival time, however, satisfying resolutions are hard to achieve in reality. Moreover, strong prior knowledge of the sound speed parameters or source locations should be used to initiate the algorithm. Achieving certain level of success, MFP based methods require accurate geometrical knowledge of the transmission environment and complex field measurements to work. In addition, the forward model is computationally hungry. Therefore, these methods are only suitable for offline processing.

Besides MFP based methods, some of the recent efforts for sound speed estimation include [74] which estimates the sound speed profiles with artificial neural networks (ANN). The inputs to the network are physical surface measurements such as heat flux and surface wind stress, and even sound speed measurements at several depths. Even though the estimated SSP is accurate, the used features are too costly to obtain for sensor nodes in an underwater network. A compressive sensing framework is used by [75] to formulate the sound speed estimation problem. In other words, the perturbation of the sound speed profile is a sparse combination of a large number of EOFs, while majority of the coefficients are zero. The method also adopts the hydrophone array measurement setup. A layered approach is used by [76], which discretizes the sound speed profile with layers and estimates the sound speeds in each layer by matching the computed reflection time with the measurements. Similarly,

Ref. [77] approximates the propagation trace within each layer by a second order polynomial, and estimates the sound speed profile using the gradient of the polynomial. The sound speed measurements are collected at the layer boundaries. A method to simultaneously estimate the uniform sound speed and the locations of floats based on low resolution propagation delay measurements is proposed by [78]. However, the computations are in a centralized fashion. In addition, the multi-floats are not treated as a network, rather they communicate with anchors independently. The work in [79] estimates the sound speed with several randomly deployed anchor nodes based on the TOF between anchor nodes and the ray theory. The proposed approach requires the collection of all the TOF measurements at a processing center. After obtaining the estimated sound speed profile, a target node can be localized according to ray theory.

Dead reckoning-based AUV localization and tracking methods utilize measurements from sensors, e.g. the Doppler Velocity Logger (DVL), and previously estimated location to update the current estimation. Those methods are known to accumulate errors and require frequent re-calibration [80]. Range-based or angle-based underwater localization methods usually do not take the heterogeneity of the sound speed into consideration and assume the propagation trace being a straight line. Then, tri-lateration or triangulation is used to locate the targets depending on the measurement type. The concept of using mobile anchor nodes to track targets is explored in [81]. In this method, range measurements are used to update locations while depth

is assumed known. The large propagation delay for the range measurement is addressed. A cooperative algorithm to track the AUVs in a fully mobile network has been proposed in [82]. Noisy depth information is assumed available from pressure sensors, thus a 3D space is mapped to a 2D plane. And the approach requires the AUVs having ranging capability, where straight line propagation is assumed implicitly. A simultaneous localization and mapping (SLAM) method in [83] proposes an approach to track the AUV and simultaneously survey the baseline transponders. A uniform sound speed is assumed to convert TOF information to range measurements. The whole trajectory of the AUV is obtained by solving a constrained optimization problem. A method to track a target with a UWSN, using particle filtering techniques, has been proposed in [84]. The underwater sensor network is static and the locations of the nodes are known. The sound pressure is the measurement and modeled as inversely proportional to the square of the distance. Another work in [85] proposes a method to localize a mobile target with a static UWSN using range or angle measurements. The mobile node only passively listens to the broadcast message from the anchor nodes and obtains the range measurements. Trajectory of the target can be estimated and improved when new measurement is obtained. The work in [86] proposes to track a target with a network using derived distances from TOF and tri-lateration. It also proposes a scheme to activate a subset of nodes to save energy.

While the majority of underwater localization works assume a constant sound speed

106

and straight line propagation, efforts have been spent on localization with more realistic sound speed assumptions. A localization and tracking algorithm in an isogradient sound speed profile is proposed in [87]. The analytic relationship between locations of the transmitting and receiving nodes and the TOF is obtained. The gradient of the TOF with respect to the locations is also obtained and used to linearize the nolinear TOF model. The results enable the tracking algorithm based on the extended Kalman filtering (EKF). The approximated sound speed profile is valid in deep water and under-ice environment. The work in [88] considers a range-independent sound speed profile and uses ray tracing to find a contour whose points have the same TOF to the anchor node. With more TOF observations, more TOF contours have to be computed. The final location of the target is obtained by minimizing the summation of the distances to all the contours. This approach is not computationally efficient and does not scale well with the number of TOF measurements. This work is extended in [89] to convert the distance information to a location vector by adopting the multidimensional scaling algorithm [90] and the stochastic proximity embedding algorithm [91]. The algorithms is operated on a computing node where computing resources are not a constraint. Similarly, [92] reduces the number of ray tracing computations by taking advantage of the fact that the rays close to each other exhibit similar pattern. However, the algorithm still requires to use the ray tracing engine, which is computationally complex and consumes large amount of energy. Therefore, it is not suitable for real time applications.

In this Chapter, we propose a Gaussian message passing (GMP)-based method to iteratively estimate the location-dependent sound speed and track the nodes in an AUV network. Several sound speed models are proposed and parameterized to capture the spatial and temporal variations. The propagation of acoustic waves in some models are derived according to the ray theory. Extensive simulations are conducted to investigate the performance of the proposed algorithm in different sound speed environments.

The major contributions of this Chapter are as follows.

- The proposed algorithm specifically considers the inhomogeneity of the sound speed field, and simultaneously solves the tracking of the AUV network and the estimation of the sound speed field. The awareness of the sound speed stratification effect makes the algorithm outperform those that simply assume a uniform sound speed [81, 82, 83, 85].

- The proposed approach enables online and distributed tracking of the spatially and temporally-varying sound speed field with a mobile AUV network, while existing sound speed inversion approaches either only work offline or need significant empirical knowledge of the sound speed field [69, 74, 75, 76].

- The spatial and temporal correlation of the sound speed field is utilized to predict the sound speed by using Gaussian process regression with truncated

observations. Therefore, the proposed underwater sound speed model is suitable for the Gaussian message passing-based framework.

The rest of the paper is organized as follows. The sound speed field models are presented in Section 4.2. The system model and the joint AUV and sound speed tracking problem are stated in Section 4.3. A factor graph-based distributed algorithm is developed for sound speed models with temporal variations in Section 4.4. The algorithm is extended to incorporate the spatial-temporal variations of the sound speed field in Section 4.5. The proposed algorithms are evaluated in Section 4.6 via simulations. Conclusions are drawn in Section 3.8.

4.2   Sound Speed Field Modeling

The sound speed in water often varies in space and time. Appropriate modeling of the sound speed field is essential to capture the sound propagation characteristics in water. Depending on the spatial and temporal variation of the sound speed field, several models can be used.

Denote the sound speed at location $[x, y, z]$ and time t by $c(x, y, z, t)$. Two simplified sound speed models include,

- Uniform sound speed model: The sound speed is assumed constant in time and

space, namely,

$$c(x, y, z, t) = c, , \qquad \forall x, y, z, t \tag{4.1}$$

which yields the straight line propagation of acoustic waves.

- Isogradient sound speed model: The sound speed is assumed only depth-dependent and invariant in time, namely,

$$c(x, y, z, t) = b + az, \qquad \forall x, y, t \tag{4.2}$$

where b is the sound speed at the water surface, and a is the changing rate of the sound speed with depth. For this model analytic solutions to the acoustic propagation have been derived in [87].

To incorporate the temporal variation of the sound speed field, the coefficients in (4.1) and (4.2) can be modeled as the first-order auto-regressive (AR1) processes. Specifically,

- Uniform sound speed with time variation:

$$c(x, y, z, t) = \bar{c} + \tilde{c}(t), \tag{4.3}$$

where $\bar{c}$ is assumed as a known constant, and $\tilde{c}(t)$ is an AR1 process,

$$\tilde{c}(t) = \tilde{c}(t-1) + w_c(t), \tag{4.4}$$

with $w_c(t) \sim \mathcal{N}(0, \sigma_c^2)$ being a zero-mean white Gaussian noise.

- Isogradient sound speed with time-varying coefficients:

$$c(x, y, z, t) = \left(\bar{b} + \tilde{b}(t)\right) + \left(\bar{a} + \tilde{a}(t)\right)z, \tag{4.5}$$

where $\bar{b}$ and $\bar{a}$ are constants usually known from empirical observations ($\bar{a} \approx 0.05$ in the Munk profile [93] and in Fig. 2.12 and $\bar{a} = 0.1$ reported in [87]), and $\tilde{b}(t)$ and $\tilde{a}(t)$ are independent AR1 processes,

$$\tilde{b}(t) = \tilde{b}(t-1) + w_b(t), \tag{4.6}$$

$$\tilde{a}(t) = \tilde{a}(t-1) + w_a(t), \tag{4.7}$$

with $w_b(t)$ and $w_a(t)$ being independent zero-mean white Gaussian noise having variance σ_b^2 and σ_a^2, respectively.

This model can closely approximate the SSP in certain water environments, such as under-ice environment and deep sea environment [94]. A more sophisticated sound speed profile could be segmented vertically and each segment can be approximated by this model [95].

To further characterize the spatial and temporal variation of the sound speed field, it can be statistically modeled as a Gaussian random field (a.k.a., Gaussian process) in space and time. Specifically,

- Spatiotemporal Gaussian process model:

$$c(\mathbf{s}) \sim \mathcal{GP}\big(\bar{m}_c(\mathbf{s}), \mathcal{K}_c(\mathbf{s}, \mathbf{s}')\big). \tag{4.8}$$

where $\mathbf{s} := [x, y, z, t]^{\mathrm{T}}$ is the coordinates in space and time, $\bar{m}_c(\mathbf{s})$ is the mean of $c(\mathbf{s})$, and $\mathcal{K}(\mathbf{s}, \mathbf{s}')$ is the covariance between $c(\mathbf{s})$ and $c(\mathbf{s}')$. In this Chapter a squared exponential covariance function is adopted,

$$\mathcal{K}(\mathbf{s}, \mathbf{s}') = \sigma_f^2 \exp\left(-\frac{(x - x')^2 + (y - y')^2 + (z - z')^2}{2l^2}\right)$$
$$\times \exp\left(-\frac{(t - t')^2}{2l_t^2}\right), \tag{4.9}$$

where σ_f^2 is the variance of $c(\mathbf{s}), \forall \mathbf{s}$, l is the distance scale that determines the field spatial correlation at locations $[x, y, z]$ and $[x', y', z']$, and l_t is the distance scale that determines the field spatial correlation at time t and t'. The three parameters, σ_f^2, l, l_t are referred to as hyper-parameters[96] and are assumed known *a priori* based on past observations.

4.3 Problem Statement

4.3.1 System Model

The system under consideration consists of M AUVs and N surface gateways deployed in an underwater area of interest $\mathcal{X}_{\text{area}} \in \mathbb{R}^3$. The AUVs maneuver underwater for a pre-defined mission, and the gateways are spatially distributed at fixed locations. The AUVs and gateways are equipped with acoustic communication units, and therefore can acoustically exchange messages underwater. In addition, surface gateways can get access to the Global Positioning System (GPS) for precise location information, and can serve as reference nodes for underwater AUV positioning. The sound speed field $c(\mathcal{X}_{\text{area}})$ in the area of interest $\mathcal{X}_{\text{area}}$ may change in space and time depending on environmental parameters, such as temperature, salinity and pressure. Time is slotted for the system operation. At the beginning of each time slot, acoustic measurements (specifically the TOF measurements between any two neighboring nodes) are collected. Within each time slot the AUVs cooperate with each other through acoustic communications for distributed AUV tracking and sound speed estimation.

Let us denote the time slot index by k, the AUV index set by $\mathcal{M} = \{1, 2, \cdots, M\}$. Let $\mathcal{N}_{\rightarrow i,k}$ denote the set of nodes that can transmit to the i-th AUV in the kth time

slot and $\mathcal{N}_{i \to ,k}$ denote the set of nodes that can receive from the i-th AUV in the kth time slot. The location of the i-th AUV at the beginning of the kth time slot is denoted by $\mathbf{x}_{i,k} := [x_{i,k}, y_{i,k}, z_{i,k}]^{\mathrm{T}} \in \mathcal{X}_{\mathrm{area}}$. For parameterization of the sound speed field $c(\mathcal{X}_{\mathrm{area}})$ in the kth time slot, $\boldsymbol{\eta}_k$ is used to denote the parameter vector. For the transmission from node i to node $j \in \mathcal{N}_{i \to ,k}$, the acoustic signal propagation delay is a function of $\mathbf{x}_{i,k}$, $\mathbf{x}_{j,k}$ and $\boldsymbol{\eta}_k$.

4.3.2 Measurement Collection

At the beginning of time slot k, node $i \in \mathcal{M}$ collects TOF measurements $\{\tau_{j \to i,k}\}$ from nodes $\{j \in \mathcal{N}_{\to i,k}\}$. When the AUV network is synchronized, the TOF can be measured from a one-way transmission, where the transmitted time stamp t_{t} is sent to node i, the TOF is simply the difference between the two time stamps, i.e. $\tau_{j \to i,k} = t_{\mathrm{r}} - t_{\mathrm{t}}$. When the AUV network is not synchronized, the TOF can be computed through the round-trip TOF. To be specific, node i sends out its transmission time $t_{i,\mathrm{t}}$ to node j. Once node j receives the information, it responds with a similar message after a time interval t_{wait}, which can be a common configuration in all the sensor nodes. Assuming the replied message is received by node i at $t_{i,\mathrm{r}}$, the TOF can be obtained as $\tau_{j \leftarrow i,k} = (t_{i,\mathrm{r}} - t_{i,\mathrm{t}} - t_{\mathrm{wait}})/2$. Note that this method assumes that the reciprocal channels are symmetric [1]. When the frequency offset of the crystals is considered, the method in [97] can be used to obtained the TOF.

The measurement of the sound propagation delay, $\tau_{j \to i,k}$, can be expressed as

$$\tau_{j \to i,k} = f_\tau(\mathbf{x}_{i,k}, \mathbf{x}_{j,k}, \boldsymbol{\eta}_k) + n_{j \to i,k}, \tag{4.10}$$

where function $f_\tau(\cdot)$ represents the nonlinear mapping of the node locations to the propagation delay in a sound speed field parameterized by $\boldsymbol{\eta}_k$, and $n_{j \to i,k} \sim \mathcal{N}(0, \sigma_{\tau,j \to i}^2)$ is the measurement noise which is assumed following a Gaussian distribution. Note that in real systems the delay measurement $\tau_{j \to i,k}$ is estimated based on the received signal at node i whose SNR decreases as the distance between the transmitter and the receiver increases. Therefore the noise variance $\sigma_{\tau,j \to i}^2$ may change with the distance between node i and node j.

4.3.3 AUV Mobility Model

We assume that all the AUVs can move independently. For the i-th AUV, its mobility can be modeled as

$$\mathbf{x}_{i,k+1} = \mathbf{x}_{i,k} + \mathbf{v}_{i,k}\Delta t + \mathbf{w}_{i,k}, \tag{4.11}$$

where $\mathbf{v}_i := [v_{x_{i,k}}, v_{y_{i,k}}, v_{z_{i,k}}]^\mathrm{T}$ is the speed vector of the i-th AUV which is available from the AUV's pitometer sensor, Δt is the time increment of one time step, and $\mathbf{w}_{i,k}$ is the model inaccuracy which is assumed following Gaussian distribution $\mathbf{w}_{i,k} \sim \mathcal{N}(\mathbf{0}_{3 \times 1}, \sigma_i^2 \mathbf{I}_3)$. For anchors, we have $\mathbf{v}_{i,k} = \mathbf{0}_{3 \times 1}$ and $\sigma_i^2 \approx 0$. From the probabilistic

perspective, the mobility model can be expressed as

$$p(\mathbf{x}_{i,k+1}|\mathbf{x}_{i,k}) \sim \mathcal{N}(\mathbf{x}_{i,k} + \mathbf{v}_{i,k}\Delta t, \sigma_i^2 \mathbf{I}_3). \tag{4.12}$$

4.3.4 Problem Formulation for Joint AUV Tracking and Sound Speed Estimation

Let us denote the locations of all the AUVs in time slot k by $\mathbf{x}_{\text{all,k}}$, all the measurements in time slot k by $\tau_{\text{all,k}}$, the locations of all the AUVs up to time slot k, by $\mathbf{x}_{\text{all}}^{(0:k)}$, and the sound speed field parameters up to time k, by $\boldsymbol{\eta}^{(0:k)}$. Similarly, we use $\tau_{\text{all}}^{(0:k)}$ to denote all the measurements up to time k.

In this Chapter, we adopt a Bayesian framework for joint sound speed estimation and AUV tracking. A recursive algorithm is designed to update the sound speed estimation and AUV locations at every time step when new measurements are available. Specifically, at time k, the sound speed and AUV locations can be estimated based on the posterior distribution $p(\mathbf{x}_{\text{all,k}}, \boldsymbol{\eta}_k | \tau_{\text{all}}^{(0:k)})$. Consider the Markovian property of the time sequences $\mathbf{x}_{\text{all}}^{(0:k)}$, $\boldsymbol{\eta}^{(0:k)}$ and $\tau_{\text{all}}^{(0:k)}$, namely, $p(\mathbf{x}_{i,k}|\mathbf{x}_i^{(0:k-1)}) = p(\mathbf{x}_{i,k}|\mathbf{x}_{i,k-1})$ (c.f. (4.12)), $p(\boldsymbol{\eta}_k|\boldsymbol{\eta}^{(0:k-1)}) = p(\boldsymbol{\eta}_k|\boldsymbol{\eta}_{k-1})$ (c.f. (4.4) and (4.6)), and $p(\tau_{\text{all,k}}|\mathbf{x}_{\text{all}}^{(0:k)}) = p(\tau_{\text{all,k}}|\mathbf{x}_{\text{all,k}})$ (c.f. (4.10)). The posteriori distribution $p(\mathbf{x}_{\text{all,k}}, \boldsymbol{\eta}_k | \tau_{\text{all}}^{(0:k)})$ can be recursively computed via message passing based on the factor-graph (FG) representation

116

of the joint posterior distribution,

$$p\big(\mathbf{x}_{\text{all}}^{(0:k)}, \boldsymbol{\eta}^{(0:k)} | \tau_{\text{all}}^{(0:k)}\big), \tag{4.13}$$

using the sum-product algorithm (SPA) [98, 99].

In Section 4.4, we first focus on the algorithm design corresponding to the sound speed environment modeled by (4.3) or (4.5). Then in Section 4.5, we extend the algorithm to sound speed models with spatiotemporal variations modeled by (4.8).

4.4 Factor Graph-based Distributed AUV Tracking and Sound Speed Estimation

In this section, we develop a distributed algorithm for joint AUV tracking and sound speed estimation through Gaussian message passing (GMP), over a factor graph (FG) representation of the posterior PDF $p\big(\mathbf{x}_{\text{all,k}}, \boldsymbol{\eta}_k | \tau_{\text{all}}^{(0:k)}\big)$, when the sound speed environment is modeled as (4.3) or (4.5). Although the non-parametric belief propagation (NBP) method [100] is applicable, it requires a significant amount of samples to achieve adequate accuracy, thus causing considerable communications overhead

within the resource-limited sensor network. The parametric GMP reduces the communication overhead through only passing the PDF parameters. Note that the measurement model in (4.10) is nonlinear and the message passing through the measurement model is non-Gaussian. We first tackle this problem by linearizing the measurement model. A factor graph representation of the joint PDF is then presented, followed by the GMP algorithm over the FG, for distributed and recursive AUV tracking and sound speed estimation.

4.4.1   Linearization of the Measurement Model

Defining $\check{\mathbf{x}}_{i,k} := [\mathbf{x}_{i,k}^{\mathrm{T}}, \mathbf{x}_{j,k}^{\mathrm{T}}, \boldsymbol{\eta}_{i,k}]^{\mathrm{T}}$, the measurement model can be rewritten as $\tau_{j\to i,k} = f_\tau(\check{\mathbf{x}}_{i,k}) + n_{j\to i,k}$. The nonlinear function $f_\tau(\check{\mathbf{x}}_{i,k})$ can be approximated by the first-order Taylor series expansion around the estimated values, $\check{\mathbf{x}}_{i,k-1}$,

$$f_\tau(\check{\mathbf{x}}_{i,k}) \approx f_\tau(\check{\mathbf{x}}_{i,k-1}) + \nabla f_\tau(\check{\mathbf{x}})|_{\check{\mathbf{x}}=\check{\mathbf{x}}_{i,k-1}}(\check{\mathbf{x}}_{i,k} - \check{\mathbf{x}}_{i,k-1}),$$

$$= D_{j\to i,k} + \mathbf{C}_{j\to i,k}^{\mathrm{T}}\mathbf{x}_{i,k} + \mathbf{E}_{j\to i,k}^{\mathrm{T}}\mathbf{x}_{j,k} + \mathbf{A}_{j\to i,k}^{\mathrm{T}}\boldsymbol{\eta}_{i,k}, \tag{4.14}$$

where we define $D_{j\to i,k} := f_\tau(\check{\mathbf{x}}_{i,k-1}) - \nabla f_\tau(\check{\mathbf{x}})|_{\check{\mathbf{x}}=\check{\mathbf{x}}_{i,k-1}}\check{\mathbf{x}}_{i,k-1}$, $\mathbf{C}_{j\to i,k} := \nabla_{\mathbf{x}_i} f_\tau(\check{\mathbf{x}})|_{\check{\mathbf{x}}=\check{\mathbf{x}}_{i,k-1}}$, $\mathbf{E}_{j\to i,k} := \nabla_{\mathbf{x}_j} f_\tau(\check{\mathbf{x}})|_{\check{\mathbf{x}}=\check{\mathbf{x}}_{i,k-1}}$, $\mathbf{A}_{j\to i,k} := \nabla_{\eta_i} f_\tau(\check{\mathbf{x}})|_{\check{\mathbf{x}}=\check{\mathbf{x}}_{i,k-1}}$. The partial derivatives of the propagation delay in uniform and isogradient sound speed environments are derived in Appendix A and can be directly incorporated here.

118

4.4.2 Factor Graph Representation of the Joint Posterior PDF in (4.13)

Factor graph along with the sum-product algorithm as an efficient tool is widely used for probabilistic marginalization in machine learning, coding, signal processing, and cooperative localization [98, 99, 101]. According to the assumptions in Section 4.3, the posterior PDF in (4.13) can be factorized as

$$
p(\mathbf{x}_{\text{all}}^{(0:k)}, \boldsymbol{\eta}^{(0:k)} | \tau_{\text{all}}^{(0:k)}) \propto p(\mathbf{x}_{\text{all}}^{(0:k)}, \boldsymbol{\eta}^{(0:k)}, \tau_{\text{all}}^{(0:k)})
$$

$$
\propto p(\mathbf{x}_{\text{all},k}, \boldsymbol{\eta}_k, \tau_{\text{all},k} | \mathbf{x}_{\text{all},k-1}, \boldsymbol{\eta}_{k-1}) p(\mathbf{x}_{\text{all}}^{(0:k-1)}, \boldsymbol{\eta}^{(0:k-1)}, \tau_{\text{all}}^{(0:k-1)})
$$

$$
\propto p(\tau_{\text{all},k} | \mathbf{x}_{\text{all},k}, \boldsymbol{\eta}_k) p(\mathbf{x}_{\text{all},k} | \mathbf{x}_{\text{all},k-1}) p(\boldsymbol{\eta}_k | \boldsymbol{\eta}_{k-1}) p(\mathbf{x}_{\text{all}}^{(0:k-1)}, \boldsymbol{\eta}^{(0:k-1)}, \tau_{\text{all}}^{(0:k-1)})
$$

$$
= \left[\prod_{k'=1}^{k} p(\tau_{\text{all},k'} | \mathbf{x}_{\text{all},k'}, \boldsymbol{\eta}_{k'}) p(\mathbf{x}_{\text{all},k'} | \mathbf{x}_{\text{all},k'-1}) p(\boldsymbol{\eta}_{k'} | \boldsymbol{\eta}_{k-1}) \right] p(\mathbf{x}_{\text{all},0}) p(\boldsymbol{\eta}_0) \tag{4.15}
$$

$$
= \prod_{k'=1}^{k} \left\{ \prod_{i \in \mathcal{M}} \left[\prod_{j \in \mathcal{N}_{\to i,k'}} p(\tau_{j \to i,k'} | \mathbf{x}_{i,k'}, \mathbf{x}_{j,k'}, \boldsymbol{\eta}_{k'}) \right] \right.
$$

$$
\left. \times p(\mathbf{x}_{i,k'} | \mathbf{x}_{i,k'-1}) \right\} p(\boldsymbol{\eta}_{k'} | \boldsymbol{\eta}_{k'-1}) \times \prod_{i \in \mathcal{M}} p(\mathbf{x}_{i,0}) p(\boldsymbol{\eta}_0) \tag{4.16}
$$

where $p(\boldsymbol{\eta}_0)$ denotes the prior PDF of the sound speed parameters following independent Gaussian distributions, i.e. $\mathcal{N}(\bar{\boldsymbol{\eta}}_0, \boldsymbol{\Sigma}_{\eta_0})$, where $\boldsymbol{\Sigma}_{\eta_0}$ is a diagonal matrix and $[\boldsymbol{\Sigma}_{\eta_0}]_{i,i} = \sigma_{\eta_i}^2$. $p(\mathbf{x}_{\text{all},0})$ denotes the prior knowledge of node locations. Here the prior

119

knowledge of node locations are assumed following independent Gaussian distributions, with $p(\mathbf{x}_{i,0}) = \mathcal{N}(\mathbf{m}_{i,0}, \sigma_{i,0}^2 \mathbf{I}_3)$ in which $\mathbf{m}_{i,0}$ is the *a priori* location of the i-th node and $\sigma_{i,0}^2 \mathbf{I}_3$ is the covariance matrix of the prior location.

Note that the sound speed coefficient $\boldsymbol{\eta}_k$ affects all the propagation delay measurements. For distributed implementation of the algorithm, we introduce a set of auxiliary variables, namely, an auxiliary local variable $\eta_{i,k}$ for node i, $\forall i \in \mathcal{M}$, and enforce the local variables at each time step to be identical to a global value (η_k). The joint PDF in (4.16) can be reformulated as

$$
\prod_{k'=1}^{k} \prod_{i \in \mathcal{M}} \Bigg\{ \prod_{j \in \mathcal{N}_{\to i,k'}} \underbrace{p(\mathbf{x}_{i,k'}|\mathbf{x}_{i,k'-1})p(\boldsymbol{\eta}_{i,k'}|\boldsymbol{\eta}_{i,k'-1})}_{:=h_{i,k'-1}}
$$
$$
\times \underbrace{\left[p(\tau_{j \to i,k'}|\mathbf{x}_{i,k'}, \mathbf{x}_{j,k'}, \boldsymbol{\eta}_{i,k'}, \boldsymbol{\eta}_{j,k'}) p_=(\boldsymbol{\eta}_{i,k'}, \boldsymbol{\eta}_{j,k'}) \right]}_{:=\phi_{j \to i,k'}} \Bigg\}
$$
$$
\times \prod_{i \in \mathcal{M}} \left\{ p(\mathbf{x}_{i,0}) \times p(\boldsymbol{\eta}_{i,0}) \prod_{j \in \mathcal{M}} p_=(\boldsymbol{\eta}_{i,0}, \boldsymbol{\eta}_{j,0}) \right\} \tag{4.17}
$$

where $p_=(\boldsymbol{\eta}_{i,k'}, \boldsymbol{\eta}_{j,k'}) := \delta(\boldsymbol{\eta}_{i,k'} - \boldsymbol{\eta}_{j,k'})$ is the Dirac delta function, representing the equality constraint on auxiliary variables.

We adopt the Forney-style factor graph [102] to represent the distribution in (4.17), where edges and vertexes denote the variables and factors in (4.17), respectively. To simplify the factor graph representation, we stack the two independent variables into a vector $\boldsymbol{\pi}_{i,k'} := [\mathbf{x}_{i,k'}^{\mathrm{T}}, \boldsymbol{\eta}_{i,k'}^{\mathrm{T}}]^{\mathrm{T}}$. Group the two transition probability factors
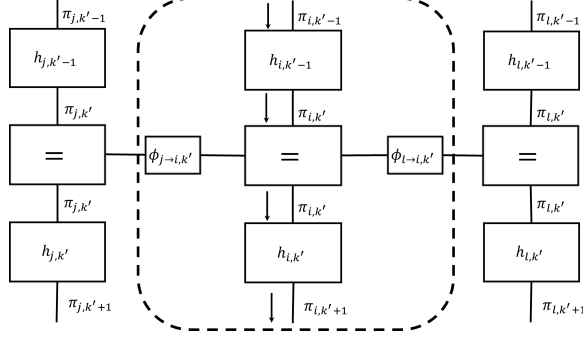
Figure 4.1: Factor graph representation of the joint posterior PDF (4.17). The black arrows show the temporal direction of message flow. The red dashed arrows represent the outgoing message through acoustic communication, and the blue arrows are the correction message. The factors within the square are maintained by node i.

Figure 4.2: Elementary linear operations in factor graph.

$p(\mathbf{x}_{i,k'}|\mathbf{x}_{i,k'-1})p(\boldsymbol{\eta}_{i,k'}|\boldsymbol{\eta}_{i,k'-1})$ into one factor denoted by $h(\boldsymbol{\pi}_{i,k'}, \boldsymbol{\pi}_{i,k'-1})$ (abbreviated as $h_{i,k'-1}$ in the FG). Group the two factors $p(\tau_{j\to i,k'}|\mathbf{x}_{i,k'}, \mathbf{x}_{j,k'}, \boldsymbol{\eta}_{i,k'}, \boldsymbol{\eta}_{j,k'})p_=(\boldsymbol{\eta}_{i,k'}, \boldsymbol{\eta}_{j,k'})$ into another factor denoted by $\phi_{j\to i,k'}(\boldsymbol{\pi}_{i,k'}, \boldsymbol{\pi}_{j,k'})$ (abbreviated as $\phi_{j\to i,k'}$ in the FG). Fig. 4.1 depicts the FG, where the i-th node and two nominal neighboring nodes $j, \ell \in \mathcal{N}_{\to i,k'}$ are taken as an example for illustration.

121

Remark 4. For the special cases of the static sound speed models, e.g. (4.1) and (4.2), the sound speed evolution model degrades to

$$p(\boldsymbol{\eta}_{i,k'}|\boldsymbol{\eta}_{i,k'-1}) = p_=(\boldsymbol{\eta}_{i,k'}, \boldsymbol{\eta}_{i,k'-1}). \tag{4.18}$$

4.4.3 Gaussian Message Propagation

A Gaussian message from edge π to vertex h in the factor graph is denoted as $\mu_{\pi \to h}(\cdot) = \mathcal{N}(\mathbf{m}_{\pi \to}, \mathbf{V}_{\pi \to h})$, where $\mathbf{m}_{\pi \to h}$ and $\mathbf{V}_{\pi \to h}$ are the mean and covariance matrix, respectively. Occasionally, the precision matrix is used instead of the covariance matrix for numerical stability, $\boldsymbol{\Sigma}_{\pi \to h} = \mathbf{V}_{\pi \to h}^{\dagger}$. Additionally, the belief of a variable π is denoted as $b_{\pi}(\cdot)$ with similar parameterization. After the linearization in Section 4.4.1, the factor graph is composed of typical vertices representing the linear operations preserving Gaussianity of input messages. The transformation of the messages going through those nodes is well known and can be found in [99]. For the sake of completeness, we list the results of related operations in Fig. 4.2, based on which we calculate the Gaussian messages propagating in the factor graph.
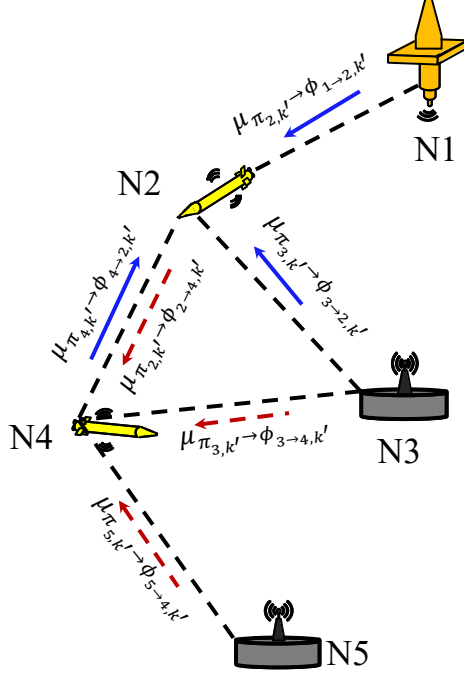
Figure 4.3: Illustration of the message transmissions in a simple network with two AUVs and three gateway nodes. The messages sent from AUV to the anchor nodes are not shown for brevity.

4.4.3.1 Message schedule

The GMP algorithm contains several typical operations, namely, prediction operation, correction operation and belief or outgoing message computation. The message flow schedule is illustrated in Fig. 4.1. At the beginning of time k', the message from the prediction operation $\mu_{h_{i,k'-1}\to\pi_{i,k'}}(\cdot)$ is computed first, which is then used to initiate the outgoing message of $\pi_{i,k'}$, $\mu_{\pi_{i,k'}\to\phi_{j\to i,k'}}(\cdot)$. The red dashed arrow in Fig. 4.1 represents the outgoing messages sent to its neighbours through acoustic communications. After receiving all the outgoing messages from neighbours, the correction operation

is performed to obtain the correction message, i.e. $\mu_{\phi_{j \to i,k'} \to \pi_{i,k'}}(\cdot)$, $\forall j \in \mathcal{N}_{\to i,k'}$, indicated by the blue arrows in Fig. 4.1. Based on the correction messages, the outgoing message or the belief message is updated for the next iteration depending on whether a broadcast scheme is used (see Remark 3 for details). After a pre-defined N_{iter} iterations are finished, the algorithm moves to the next time step and uses the belief message as the prior for the prediction operation. Fig. 4.3 illustrates the message exchange in a simple network with two AUVs and three gateway nodes. The messages sent from AUV to the anchor nodes are not shown for brevity. The algorithm with the broadcast scheme is summarized in Algorithm 1. The details of the typical operations are as follows.

4.4.3.1.1 Prediction Operation At time slot k, the prediction operation models the AUV mobility and sound speed evolution to obtain $\mu_{h_{i,k'-1} \to \pi_{i,k'}}(\cdot)$. Due to the independence of the two evolution models, this is equivalent to predicting $\mu_{h_{i,k'-1} \to \mathbf{x}_{i,k'}}(\cdot)$ and $\mu_{h_{i,k'-1} \to \eta_{i,k'}}(\cdot)$ independently.

Given $\mu_{\pi_{i,k'-1} \to h_{i,k'-1}}(\cdot)$, the *a posteriori* message from previous time step $k' - 1$, and the mobility model in (4.12), the predicted mean and covariance matrix related to
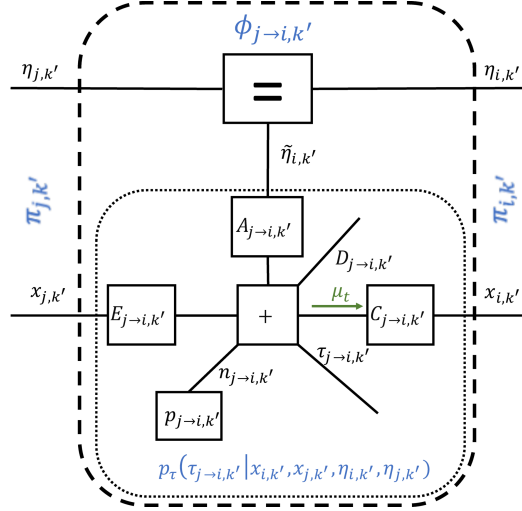
Figure 4.4: Extended factor graph of $\phi_{j\to i,k'}$ after linearization. The blue notations correspond to the variable or function names in the factor graph Fig. 4.1.

the node location are

$$\mathbf{m}_{h_{i,k'-1}\to\mathbf{x}_{i,k'}} = \mathbf{m}_{x_{i,k'-1}\to h_{i,k'-1}} + \mathbf{v}_{i,k'}\Delta t, \tag{4.19}$$

$$\mathbf{V}_{h_{i,k'-1}\to\mathbf{x}_{i,k'}} = \mathbf{V}_{x_{i,k'-1}\to h_{i,k'-1}} + \sigma_i^2\mathbf{I}_3. \tag{4.20}$$

With the assumption that the sound speed parameters evolve as a random walk process, prediction of the sound speed parameters can be obtained as

$$\mathbf{m}_{h_{i,k'-1}\to\eta_{i,k'}} = \mathbf{m}_{\eta_{i,k'-1}\to h_{i,k'-1}}, \tag{4.21}$$

$$\mathbf{V}_{h_{i,k'-1}\to\eta_{i,k'}} = \mathbf{V}_{\eta_{i,k'-1}\to h_{i,k'-1}} + \mathbf{V}_{\eta_{k'}}. \tag{4.22}$$

125

4.4.3.1.2 Correction Operation The correction operation incorporates the measurements to update the location and the sound speed parameters. The resulting message denoted as $\mu_{\phi_{j\rightarrow i,k'}\rightarrow\pi_{i,k'}}(\cdot)$ can be decomposed as $\mu_{\phi_{j\rightarrow i,k'}\rightarrow\mathbf{x}_{i,k'}}(\cdot)$ and $\mu_{\phi_{j\rightarrow i,k'}\rightarrow\eta_{i,k'}}(\cdot)$, which are treated separately.

As presented in Section 4.4.1, the node $\phi_{j\rightarrow i,k'}$ depicts the nonlinear measurement model and can be linearized to preserve the Gaussianity of the transformations. The linearized vertex of $\phi_{j\rightarrow i,k'}$ is illustrated in Fig. 4.4. To perform the correction operation at agent i, the messages $\mu_{\pi_{j,k}\rightarrow i,k'}(\cdot)\ \forall j\in\mathcal{N}_{\rightarrow i,k'}$ are first collected from its neighbours through acoustic communications, as indicated by the red arrows in Fig. 4.4. Meanwhile, the message $\mu_{\pi_{i,k'}\rightarrow\phi_{j\rightarrow i,k'}}(\cdot)$ is available locally at node i. Let us denote the intermittent message from the "summation" node to $\mathbf{C}_{j\rightarrow i,k'}$ by μ_t. Following the result from Fig. 4.2, we can obtain,

$$\mathbf{m}_t = \tau_{j\rightarrow i,k'} - (D_{j\rightarrow i,k'} + \mathbf{E}_{j\rightarrow i,k'}\mathbf{m}_{\mathbf{x}_{j,k'}\rightarrow\mathbf{E}_{j\rightarrow i,k'}} + \mathbf{A}_{j\rightarrow i,k'}\mathbf{m}_{\tilde{\eta}_{i,k'}\rightarrow A_{j\rightarrow i,k'}}), \qquad (4.23)$$

$$\mathbf{V}_t = \sigma^2_{j\rightarrow i,k'} + \mathbf{A}_{j\rightarrow i,k'}\mathbf{V}_{\tilde{\eta}_{i,k'}\rightarrow A_{j\rightarrow i,k'}}\mathbf{A}^{\mathrm{T}}_{j\rightarrow i,k'} + \mathbf{E}_{j\rightarrow i,k'}\mathbf{V}_{\mathbf{x}_{j,k'}\rightarrow\mathbf{E}_{j\rightarrow i,k'}}\mathbf{E}^{\mathrm{T}}_{j\rightarrow i,k'}, \qquad (4.24)$$

where $\mathbf{m}_{\tilde{\eta}_{i,k'}\rightarrow A_{j\rightarrow i,k'}}$ and $\mathbf{V}_{\tilde{\eta}_{i,k,k'}\rightarrow A_{j\rightarrow i,k'}}$ are extracted locally from $\mu_{\pi_{i,k'}\rightarrow\phi_{j\rightarrow i,k'}}(\cdot)$. The message $\mu_{\phi_{j\rightarrow i,k'}\rightarrow\mathbf{x}_{i,k'}}(\cdot)$ is a result of the transformation by vertex $\mathbf{C}_{j\rightarrow i,k'}$ on the

intermittent message $\mu_t(\cdot)$, thus

$$\mathbf{m}_{\phi_{j\to i,k'}\to\mathbf{x}_{i,k'}} = (\mathbf{C}_{j\to i,k'}^{\mathrm{T}}\mathbf{V}_t^\dagger\mathbf{C}_{j\to i,k'})^\dagger\mathbf{C}_{j\to i,k'}^{\mathrm{T}}\mathbf{V}_t^\dagger\mathbf{m}_t, \qquad (4.25)$$

$$\mathbf{V}_{\phi_{j\to i,k'}\to\mathbf{x}_{i,k'}} = (\mathbf{C}_{j\to i,k'}^{\mathrm{T}}\mathbf{V}_t^\dagger\mathbf{C}_{j\to i,k'})^\dagger. \qquad (4.26)$$

The intermittent correction message for the sound speed parameters, $\mu_{\mathbf{A}_{j\to i,k'}\to\tilde{\eta}_{i,k'}}(\cdot)$, can be obtained following the same procedures. Incorporating the message $\mu_{\eta_{j,k'}\to\phi_{j\to i,k'}}(\cdot)$, the final correction message for the sound speed is obtained as,

$$\mu_{\phi_{j\to i,k'}\to\eta_{i,k'}}(\cdot) = \mu_{\mathbf{A}_{j\to i,k'}\to\tilde{\eta}_{i,k'}}(\cdot) \times \mu_{\eta_{j,k'}\to\phi_{j\to i,k'}}(\cdot). \qquad (4.27)$$

The product of two or multiple Gaussian messages is equivalent to the "equality" transformation in Fig. 4.2, where the results can be used to compute the mean and the precision matrix of $\mu_{\phi_{j\to i,k'}\to\eta_{i,k'}}(\cdot)$.

Remark 5. If $\mu_{\eta_{j,k'}\to\phi_{j\to i,k'}}(\cdot)$ is not transmitted by agent j, $\mu_{\phi_{j\to i,k'}\to\tilde{\eta}_{i,k'}}(\cdot)$ can be treated as $\mu_{\phi_{j\to i,k'}\to\eta_{i,k'}}(\cdot)$ with slight performance degradation. Additionally, consensus of the network estimation on the sound speed parameters might not reach.

4.4.3.1.3 Outgoing Message and Belief Message During the correction operation, the outgoing message $\mu_{\pi_{i,k'}\to\phi_{j\to i,k'}}(\cdot)$ is required and can be computed at

---
Algorithm 1 Joint UWSN and Sound Speed Tracking in Uniform or Isogradient Sound Speed

---
Input: Prior message $\mu_{\pi_{i,0} \to h_{i,0}}(\cdot) \; \forall i \in \mathcal{M}$, number of iterations N_{iter}
Output: Beliefs of sensor locations and sound speed

1: **for** $k = 1, \cdots$ **do** (# time step index)
2:     Compute the prediction $\mu_{h_{i,k-1} \to \pi_{i,k}}(\cdot)$ according to Eqs. (4.19) to (4.22) **in parallel** $\forall i \in \mathcal{M}$
3:     Initialize beliefs $b^{(0)}_{\pi_{i,k}}(\cdot) = \mu_{h_{i,k-1} \to \pi_{i,k}}(\cdot)$ **in parallel** $\forall i \in \mathcal{M}$
4:     **for** $l = 1, 2, \cdots, N_{\text{iter}}$ **do** (# iteration index)
5:        Broadcast $b^{(l-1)}_{\pi_{i,k}}(\cdot)$ **in parallel** $\forall i \in \mathcal{M}$
6:        Receive $\mu_{\pi_j \to \phi_{j \to i}} = b^{(l-1)}_{\pi_{j,k}}(\cdot) \; \forall j \in \mathcal{N}_{\to i,k}$ **in parallel** $\forall i \in \mathcal{M}$
7:        Compute the correction messages $\mu_{\phi_{j \to i,k} \to \pi_{i,k}}(\cdot) \; \forall j \in \mathcal{N}_{\to i,k}$ according to Eqs. (4.23) to (4.27) **in parallel** $\forall i \in \mathcal{M}$
8:        Update the belief $b^{(l)}_{\pi_{i,k}}(\cdot)$ according to (4.29) **in parallel** $\forall i \in \mathcal{M}$.
9:     **end for**
10:    Assign posterior message $\mu_{\pi_{i,k} \to h_{i,k}}(\cdot) = b^{(N_{\text{iter}})}_{\pi_{i,k}}(\cdot)$ **in parallel** $\forall i \in \mathcal{M}$
11: **end for**

---

agent i. Although we treat the location variable $\mathbf{x}_{i,k'}$ and the sound speed parameters $\boldsymbol{\eta}_{i,k'}$ as a whole, the corresponding formulae can be applied independently for each variable. Assuming that all the correction messages are available, *i.e.* $\mu_{\phi_{j' \to i,k'} \to \pi_{i,k'}}(\cdot) \; \forall j' \in \mathcal{N}_{\to i,k'}, j' \neq j$, the outgoing message can be computed as

$$\mu_{\pi_{i,k'} \to \phi_{j \to i,k'}}(\cdot) = \mu_{h_{i,k'-1} \to \pi_{i,k'}}(\cdot) \prod_{j' \in \mathcal{N}_{\to i,k'}, j' \neq j} \mu_{\phi_{j' \to i,k'} \to \pi_{i,k'}}(\cdot). \tag{4.28}$$

As the summary of a variable, the belief message can be similarly computed as

$$b_{\pi_{i,k'}}(\cdot) = \mu_{h_{i,k'-1} \to \pi_{i,k'}}(\cdot) \prod_{j' \in \mathcal{N}_{\to i,k'}} \mu_{\phi_{j' \to i,k'} \to \pi_{i,k'}}(\cdot). \tag{4.29}$$

Again, the product of multiple Gaussian messages can be obtained from the results in Fig. 4.2. Note that the only difference between the belief message $b_{\pi_{i,k'}}$ and

the outgoing message $\mu_{\pi_{i,k'} \to \phi_{j \to i,k'}}(\cdot)$ is the incorporation of the correction message $\mu_{\phi_{j \to i,k'} \to \pi_{i,k'}}(\cdot)$.

Remark 6. Each outgoing message needs to be transferred to its corresponding neighbor, for example, $\mu_{\pi_{i,k'} \to \phi_{j \to i,k'}}(\cdot)$ is needed at agent j. Thus, the communication overhead is formidable. In reality, the agents can broadcast the belief message to all the neighbours in place of the target specific messages. Thus, the communication overhead is significantly reduced.

4.5 Extension to Spatially and Temporally Varying Sound Speed Field

In this section, we extend the proposed algorithm to the sound speed environment with spatiotemporal variations modeled as a Gaussian random field as in (4.8). In the previous time-varying sound speed models, the sound speed parameter only depends on the value at the previous time step. On the contrary, in a spatiotemporal GP sound speed model, all the current and historical sound speed observations at different locations are correlated. This brings challenges for a distributed and memory efficient algorithm. To alleviate the obstacle, we ignore the less correlated observations in the Gaussian process, and only focus on the most relevant observations. Following the

same procedures, we first factorize the joint posterior PDF in (4.13). Then based on the factorization, the factor graph and GMP algorithm are developed.

4.5.1 Factorization of the Joint Posterior PDF (4.13)

The posterior PDF can be reformulated as

$$p(\mathbf{x}_{\text{all}}^{(0:k)}, c(\mathbf{x}_{\text{all}}^{(0:k)}), \tau_{\text{all}}^{(0:k)}) \propto p(\tau_{\text{all},k}|\mathbf{x}_{\text{all},k}, c(\mathbf{x}_{\text{all},k}))$$

$$\times p(\mathbf{x}_{\text{all},k}, c(\mathbf{x}_{\text{all},k})|\mathbf{x}_{\text{all}}^{(0:k-1)}, c(\mathbf{x}_{\text{all}}^{(0:k-1)}))p(\mathbf{x}_{\text{all}}^{(0:k-1)}, c(\mathbf{x}_{\text{all}}^{(0:k-1)}), \tau_{\text{all}}^{(0:k-1)}). \quad (4.30)$$

For distributed and recursive estimation of AUV locations and the sound speed field, several approximations are made in the following. Firstly,

- AS1) The sound propagation delay from node j to node i depends on the sound speed field $c(\mathcal{X}_{\text{area}})$. Here the measurement model is approximated as

$$\tau_{j\to i,k} = \frac{\|\mathbf{x}_{i,k} - \mathbf{x}_{j,k}\|}{(c(\mathbf{x}_{i,k}) + c(\mathbf{x}_{j,k}))/2} + n_{j\to i,k}, \quad (4.31)$$

where $\|\mathbf{x}_{i,k} - \mathbf{x}_{j,k}\|$ is the Euclidean distance between the two agents.

Therefore, the likelihood function can be factorized as

$$p(\tau_{\mathrm{all},k}|\mathbf{x}_{\mathrm{all},k}, c(\mathbf{x}_{\mathrm{all},k}))$$

$$= \prod_{i\in\mathcal{M}} \prod_{j\in\mathcal{N}_{\rightarrow i,k}} p(\tau_{j\rightarrow i,k}|\mathbf{x}_{i,k}, \mathbf{x}_{j,k}, c(\mathbf{x}_{i,k}), c(\mathbf{x}_{j,k})). \qquad (4.32)$$

Secondly, the conditional PDF $p(\mathbf{x}_{\mathrm{all},k}, c(\mathbf{x}_{\mathrm{all},k})|\mathbf{x}_{\mathrm{all}}^{(0:k-1)}, c(\mathbf{x}_{\mathrm{all}}^{(0:k-1)}))$ can be approximated as,

$$p(\mathbf{x}_{\mathrm{all},k}, c(\mathbf{x}_{\mathrm{all},k})|\mathbf{x}_{\mathrm{all}}^{(0:k-1)}, c(\mathbf{x}_{\mathrm{all}}^{(0:k-1)})),$$

$$= p(c(\mathbf{x}_{\mathrm{all},k})|\mathbf{x}_{\mathrm{all},k}, \mathbf{x}_{\mathrm{all}}^{(0:k-1)}, c(\mathbf{x}_{\mathrm{all}}^{(0:k-1)}))p(\mathbf{x}_{\mathrm{all},k}|\mathbf{x}_{\mathrm{all}}^{(0:k-1)}),$$

$$\overset{\mathrm{AS2)}}{\approx} p(c(\mathbf{x}_{\mathrm{all},k})|\mathbf{x}_{\mathrm{all},k}, \mathbf{x}_{\mathrm{all},k-1}, c(\mathbf{x}_{\mathrm{all},k-1}))p(\mathbf{x}_{\mathrm{all},k}|\mathbf{x}_{\mathrm{all}}^{(0:k-1)}), \qquad (4.33)$$

$$\overset{\mathrm{AS3)}}{\approx} \prod_{i\in\mathcal{M}} p(c(\mathbf{x}_{i,k})|\mathbf{x}_{i,k}, \mathbf{x}_{\mathrm{all},k-1}, c(\mathbf{x}_{\mathrm{all},k-1}))p(\mathbf{x}_{\mathrm{all},k}|\mathbf{x}_{\mathrm{all}}^{(0:k-1)}), \qquad (4.34)$$

$$\overset{\mathrm{AS4)}}{\approx} \prod_{i\in\mathcal{M}} p(c(\mathbf{x}_{i,k})|\mathbf{x}_{i,k}, \mathbf{x}_{i,k-1}, \{\mathbf{x}_{j,k-1}\}_{j\in\mathcal{N}_{\rightarrow i,k-1}}$$

$$, c(\mathbf{x}_{i,k-1}), \{c(\mathbf{x}_{j,k-1})\}_{j\in\mathcal{N}_{\rightarrow i,k-1}}) \prod_{i\in\mathcal{M}} p(\mathbf{x}_{i,k}|\mathbf{x}_{i,k-1}),$$

$$= \prod_{i\in\mathcal{M}} p(c(\mathbf{x}_{i,k}), \mathbf{x}_{i,k}|\mathbf{x}_{i,k-1}, \{\mathbf{x}_{j,k-1}\}_{j\in\mathcal{N}_{\rightarrow i,k-1}}, c(\mathbf{x}_{i,k-1}), \{c(\mathbf{x}_{j,k-1})\}_{j\in\mathcal{N}_{\rightarrow i,k-1}}). \quad (4.35)$$

- AS2): As a Gaussian process, the sound speed samples at the current locations $c(x_{\mathrm{all},k})$ are correlated to all the historical sound speed samples $c(x_{\mathrm{all}}^{(0:k-1)})$. Together they follow a Gaussian distribution. We remove the dependence of $c(x_{\mathrm{all},k})$ on the historical samples except those in the last time step, i.e.

$c(x_{\mathrm{all},k-1})$. The temporal truncation enables the memory efficient algorithm design since only the latest sound speed samples are maintained in memory.

- AS3): Conditioned on the sound speed samples in the previous time step $c(\mathbf{x}_{\mathrm{all},k-1})$, the sound speed sample at one location $c(\mathbf{x}_{i,k})$ is independent of the sound speed sample at other locations at time k, thus the joint PDF of the sound speed samples at time k is approximated as the product of the independent PDF of each sound speed samples.

- AS4): From the covariance function in (4.9), the covariance between two sound speed variables decreases with the distance between the sample locations. We assume the covariance becomes negligible when the distance is greater than the communication distance. In other word, the sound speed sample $c(\mathbf{x}_{i,k})$ is assumed to be independent of the samples whose locations are not in its communication range.

Remark 7. AS2) and AS4) temporally and spatially truncate the correlated observations of a Gaussian process. While the assumptions reflect the temporal and spatial constraints of the mobile network, the impact of observation truncation on Gaussian process regression is analyzed in [103].

Let us define $\boldsymbol{\pi}_{i,t,k} := [\mathbf{x}_{i,k}^{\mathrm{T}}, c(\mathbf{x}_{i,k})]^{\mathrm{T}}$. The joint posterior PDF can be approximated

132
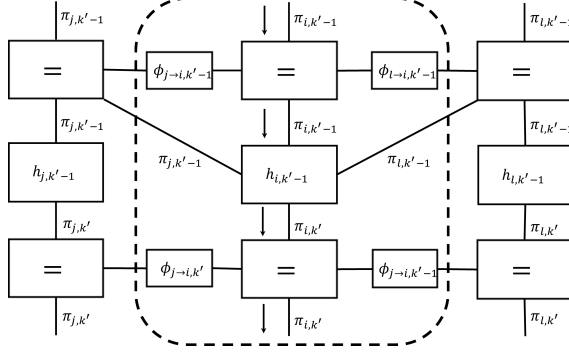
Figure 4.5: Factor graph for the joint UWSN and sound speed tracking problem in a location-dependent sound speed. The black arrows show the temporal direction of message flow. The red dashed arrows represent the outgoing message through acoustic communication, and the blue arrows are the correction message.
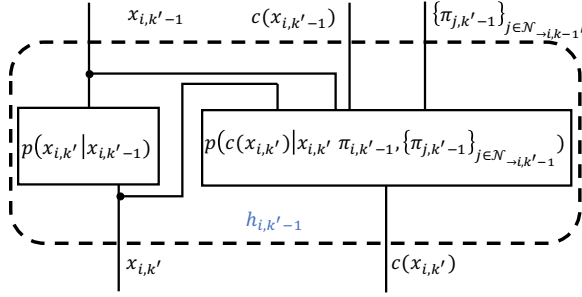
Figure 4.6: Extended graph of the prediction operation, $h_{i,k'-1}$, in the FG with spatiotemporal variations.

as,

$$\prod_{k'=1}^{k}\prod_{i\in\mathcal{M}}\left\{\prod_{j\in\mathcal{N}_{\rightarrow i,k'}}[p(\tau_{j\rightarrow i,k'}|\boldsymbol{\pi}_{i,k'},\boldsymbol{\pi}_{j,k'})]p(\boldsymbol{\pi}_{i,k'}|\boldsymbol{\pi}_{i,k'-1},\{\boldsymbol{\pi}_{j,k'-1}\}_{j\in\mathcal{N}_{\rightarrow i,k'-1}})\right\}\prod_{i\in\mathcal{M}}p(\boldsymbol{\pi}_{i,0}).$$

(4.36)

with $p(\boldsymbol{\pi}_{i,0}) = p(\mathbf{x}_{i,0})p(c(\mathbf{x}_{i,0}))$. Let us denote $p(\boldsymbol{\pi}_{i,k'}|\boldsymbol{\pi}_{i,k'-1},\{\boldsymbol{\pi}_{j,k'-1}\}_{j\in\mathcal{N}_{\rightarrow i,k'-1}})$ by $h_{i,k'-1}$ and $p(\tau_{j\rightarrow i,k'}|\boldsymbol{\pi}_{i,k'},\boldsymbol{\pi}_{j,k'})$ by $\phi_{j\rightarrow i,k'}$ for brevity, the corresponding factor graph is depicted in Fig. 4.5.

133

4.5.2 Gaussian Message Propagation

The message schedule for the extended GMP algorithm is similar to the original one in Section 4.4.3.1, except that the final beliefs from each agent's neighbours, e.g. $b_{\pi_{j,k'-1}}(\cdot)$, $\forall j \in \mathcal{N}_{\to i,k'-1}$, are stored in memory and used in the prediction operation at time k. Note that the communication overhead is not increased because the belief message $b_{\pi_{j,k'-1}}(\cdot)$ has already been collected at time $k'-1$ for the correction operation. Thus, the extended algorithm for sound speed filed with spatiotemporal variations can also be summarized in Algorithm 1, except that the prediction and correction operations should be modified to accommodate the factor graph change.

4.5.2.1 Prediction Operation

The structure of the factor graph in Fig. 4.5 for the extended sound speed model is different from Fig. 4.1 only in the connections from $\pi_{j,k'-1}$ to $h_{i,k'-1}$. These additional connections lead to a different prediction operation. The corresponding vertex $h_{i,k'-1}$ is expanded in Fig. 4.6. It can be observed that the AUV mobility model is the same, i.e. modeled by $p(\mathbf{x}_{i,k'}|\mathbf{x}_{i,k'-1})$. On the contrary, the evolution of the sound speed at one location is no longer independent of the other locations as indicated by $p(c(\mathbf{x}_{i,k'})|c(\mathbf{x}_{i,k'-1}), \{\pi_{j,k'-1}\}_{j\in\mathcal{N}_{\to i,k'-1}})$. Considering the belief messages $b_{\pi_{i,k'-1}}(\cdot)$ and

$b_{\pi_{j,k'-1}}(\cdot)$ flowing into $h_{j,k'-1}$ as the noisy observation of the true Gaussian process at $\mathbf{x}_{i,k'-1}$ and $\mathbf{x}_{j,k'-1}$, respectively, the Gaussian process regression (GPR) algorithm can be utilized to compute the prediction message of the sound speed $\mu_{h_{j,k'-1}\to\pi_{j,k'}}(\cdot)$.

Let us define $\mathbf{m}_{c_{i,k'-1}} := [m_{c_{i,k'-1}}, m_{c_{j_1,k'-1}}, \cdots, m_{c_{j_{N_i},k'-1}}]^{\mathrm{T}}$ and a diagonal covariance matrix $\mathbf{V}_{c_{i,k'-1}} := \mathrm{diag}([\sigma^2_{c_{i,k'-1}}, \sigma^2_{c_{j_1,k'-1}}, \cdots, \sigma^2_{c_{j_{N_i},k'-1}}]^{\mathrm{T}})$, where $j_{N_i} \in \mathcal{N}_{\to i,k'-1}$ and N_i is the number of elements in $\mathcal{N}_{\to i,k'-1}$, the mean and variance of the sound speed are extracted from $b_{\pi_{j,k'-1}}(\cdot)$. We denote the coordinate in space and time by $\mathbf{s}_{i,k'} = [\mathbf{x}^{\mathrm{T}}_{i,k'}, k']^{\mathrm{T}}$ and stack the coordinates of the observations into $\mathbf{S} :=$ $[\mathbf{s}_{i,k'-1}, \mathbf{s}_{j,k'-1}, \cdots, \mathbf{s}_{j_{N_i},k'-1}]$. We also define a matrix $\mathbf{K}_c$ as a $(N_i+1)\times(N_i+1)$ matrix, the elements are the covariances of the observation pairs $[\mathbf{K}_c]_{i_1,i_2} := \mathcal{K}(\mathbf{s}_{i_1}, \mathbf{s}_{i_2})$, which is the squared exponential function defined in (4.9) and $[\mathbf{S}]_{i_1}$ is the i_1^{th} coordinate in $\mathbf{S}$. Similarly, we define a covariance vector $\mathbf{k}_c$ whose elements is $[\mathbf{k}_c]_{i_1} := \mathcal{K}(\mathbf{s}_{i,k'}, [\mathbf{S}]_{i_1})$. and a scalar $k_c := \mathcal{K}(\mathbf{s}_{i,k'}, \mathbf{s}_{i,k'})$, where $\mathbf{s}_{i,k'} = [\mathbf{x}^{\mathrm{T}}_{i,k'}, k']^{\mathrm{T}}$ is the coordinate of the target.

According to the GPR algorithm in Appendix B, the prediction message $\mu_{h_{j,k'-1}\to c(\mathbf{x}_{i,k'})}(\cdot)$ can be computed as

$$\sigma^2_{h_{j,k'-1}\to c(\mathbf{x}_{i,k'})} = k_c - \mathbf{k}_c(\mathbf{K}_c + \mathbf{V}_{c_{i,k'-1}})^{\dagger}\mathbf{k}^{\mathrm{T}}_c, \tag{4.37}$$

$$m_{h_{j,k'-1}\to c(\mathbf{x}_{i,k'})} = \bar{m}_{c_{i,k'}} + \mathbf{k}_c(\mathbf{K}_c + \mathbf{V}_{c_{i,k'-1}})^{\dagger}(\mathbf{m}_{c_{i,k'-1}} - \bar{\mathbf{m}}_{c_{i,k'-1}}), \tag{4.38}$$

where $\bar{m}_{c_{i,k'}} = \bar{m}(\mathbf{s}_{i,k'})$ is the mean of the sound speed parameters at the target

location, and $\bar{\mathbf{m}}_{c_{i,k'-1}}$ is the vector of the mean sound speed at the locations of observations.

Remark 8. The unknown hyperparameters in the covariance function (4.9), i.e. $\{\sigma_f^2, l, l_t\}$, can be estimated by maximizing the marginal likelihood function [96], detailed results can be found in Appendix B.

4.5.2.2 Correction Operation

The extended factor graph for the correction operation $\phi_{j \to i,k'}$ is similar to Fig. 4.4. A major difference is that the two sound speeds are summed together and used in the measurement model, and the node $A_{j \to i,k'}$ absorbs the constant $1/2$. Similar to the procedures in (4.25) and (4.26), the correction message $\mu_{\phi_{j \to i,k'} \to \mathbf{x}_{i,k'}}(\cdot)$ and $\mu_{\mathbf{A}_{j \to i,k'} \to \tilde{c}(\mathbf{x}_{i,k'})}(\cdot)$ can be computed. Incorporating the results in Fig. 4.2 and the message $\mu_{c(\mathbf{x}_{j,k'}) \to \phi_{j \to i,k'}}(\cdot)$, the final correction message $\mu_{\phi_{j \to i,k'} \to \tilde{c}(\mathbf{x}_{i,k'})}(\cdot)$ for the sound speed can be obtained.

Remark 9. If the sound speed can be measured by an AUV at its location, for example, $\tilde{c}(\mathbf{x}_{i,k}) = c(\mathbf{x}_{i,k}) + n_{c_{i,k}}$, where $n_{c_{i,k}}$ is assumed to be a Guassian noise. The independent measurements at all the AUVs can be easily fused together with estimated sound speed field in our problem setup. The factorization in (4.36) can be

modified as

$$\prod_{k'=1}^{k} \prod_{i \in \mathcal{M}} \left\{ \prod_{j \in \mathcal{N}_{\to i,k'}} [p(\tau_{j \to i,k'} | \boldsymbol{\pi}_{i,k'}, \boldsymbol{\pi}_{j,k'})] p(\boldsymbol{\pi}_{i,k'} | \boldsymbol{\pi}_{i,k'-1}, \{\boldsymbol{\pi}_{j,k'-1}\}_{j \in \mathcal{N}_{\to i,k'-1}}) \right.$$

$$\left. \times p(\tilde{c}(\mathbf{x}_{i,k}) | c(\mathbf{x}_{i,k})) \right\} \prod_{i \in \mathcal{M}} p(\boldsymbol{\pi}_{i,0}). \tag{4.39}$$

With this factorization, the factor graph and the corresponding Gaussian message propagation algorithm can be modified slightly. Specifically, the correction operation and the belief message computation procedures should be changed accordingly.

The belief and outgoing message computations, and the message schedule are the same as the original algorithm. Thus Algorithm 1 can also be used for the spatially and temporally varying sound speed with modification of the prediction and correction procedures.

4.6 Simulation Results

In this section, we evaluate the proposed algorithm through Monte Carlo simulations. In the simulations, we target a rectangular region of $d_{\max} \times d_{\max}$. $N = 9$ anchors are fixed at locations whose coordinates along each dimension equal $[0, 0.5, 1] \times d_{\max}$, and $M = 100$ mobile agents are randomly distributed in the region initially following

(a) Initialization   (b) Time step 1
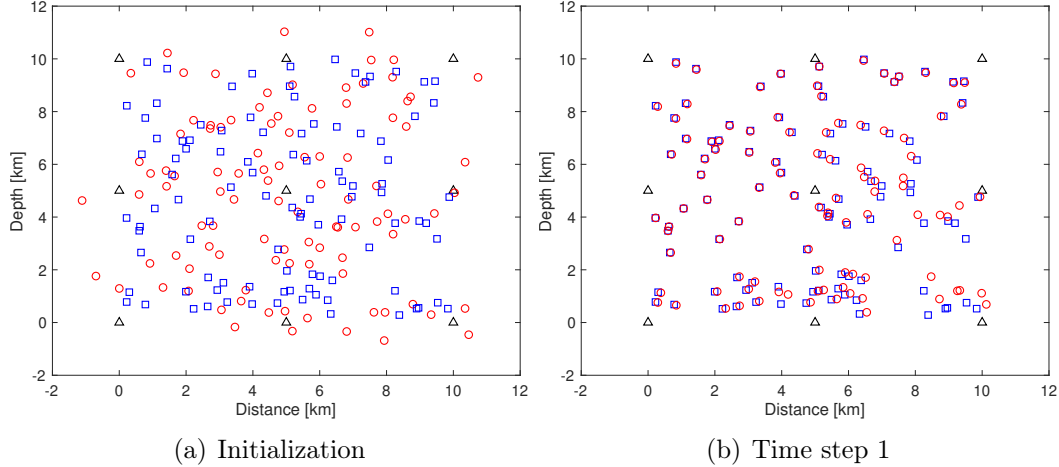
Figure 4.7: Estimation results of the network at different time steps. The black triangles are the anchor nodes, the blue squares are the mobile agents, and the red circles are the estimated locations of the mobile agents. $N_{\text{iter}} = 10$ iterations are performed within each time step.

uniform distribution. The initial guess of the ith agent's location is randomly generated around the true location as $\hat{\mathbf{x}}_{i,0} = \mathbf{x}_{i,0} + \mathbf{e}$, where $\mathbf{e} \sim \mathcal{N}(\mathbf{0}, \sigma_e^2 \mathbf{I})$. For anchor nodes, $\sigma_e = 10^{-4} \times d_{\text{max}}$ reflecting a strong prior knowledge, and for the mobile nodes $\sigma_{\mathbf{e}} = 0.1 \times d_{\text{max}}$ reflecting a weak prior knowledge. The maximum communication distance of the mobile agents and anchors is a portion of the length of the region, i.e. $d_{\text{comm}} = r_c \times d_{\text{max}}$. For all the simulations, a total number of $K = 30$ time steps is investigated. N_{iter} iterations are computed within each time step. The algorithm is assumed to use the broadcast scheme if not specified otherwise. The mobile agents move according to the model in (4.12), where the sound speed $\mathbf{v}_i$ along each direction is randomly generated following uniform distribution in the interval $[-3, 3]$ m/s at each time step, and the standard deviation of the movement noise is $\sigma_i = 20$ m. The interval of each time step is $\Delta t = 10$ s. Because the propagation delay is

138

estimated from the received signal, the accuracy depends on the SNR of the signal. Thus, the standard deviation of the observation noise is assumed to be proportional to the nominal propagation delay between node i and node j in the mean sound speed $\bar{c} = 1500$ m/s, i.e. $\sigma_{ij} \sim \mathcal{N}(0, r_o d_{ij}/\bar{c})$, where r_o is a scaling constant. We use the root mean square error (RMSE) as the metric for localization and sound speed estimation performance,

$$\text{RMSE}[k] = \sqrt{\frac{1}{M} \sum_{i}^{M} \|\mathbf{x}_{i,k} - \hat{\mathbf{x}}_{i,k}\|^2}, \tag{4.40}$$

where $\hat{\mathbf{x}}_{i,k}$ is the estimated location of node i at time k and $\| \cdot \|$ is the l_2-norm.

Due to the similarity of the sound speed models, the algorithm is investigated in the following typical sound speed models: a) time-varying uniform sound speed model in (4.3); b) time-varying isogradient sound speed in (4.5); c) spatiotemporal Gaussian process sound speed model in (4.8).

4.6.1 Time-varying Homogeneous Sound Speed

First, we investigate the algorithm performance in a time-varying homogeneous sound speed field. The length of the area is $d_{\text{max}} = 10$ km. The sound speed evolves as the random walk process defined in (4.4), and the noise standard deviation $\sigma_c = 5$ m/s.

Fig. 4.7 illustrates the cooperative localization performance from a realization. The

algorithm is initialized as in Fig. 4.7(a), The black triangles are the anchor nodes, the blue squares are the mobile agents, and the red circles are the estimated locations of the mobile agents. The number of iterations at each time step is $N_{\text{iter}} = 10$, and the communication distance scale is $r_c = 0.3$. Fig. 4.7(b) is the estimation of the network after time step 1. As we can observe, the network is able to localize majority of the mobile agents after the first time step.

Fig. 4.8 shows how the observation noise affects the tracking performance. The AUVs can either send target specific messages about the location and sound speed estimation or broadcast the message to all neighbours. Obviously, the broadcast scheme reduces communication load significantly. Fig. 4.8 compares the performance of the two message transmission schemes with different observation noise level. $N_{\text{iter}} = 3$ iterations are conducted in each time step, and the communication distance scale is $r_c = 0.3$. The tested observation noise scales are $r_o = [0.02, 0.04, 0.06]$. It can be observed that the two schemes have very close performance, with the target-specific scheme slightly better than the broadcast scheme. The same results can be observed in simulations of the time-varying isogradient sound speed model and spatiotemporal Gaussian process model.

(a) Network	(b) Sound speed
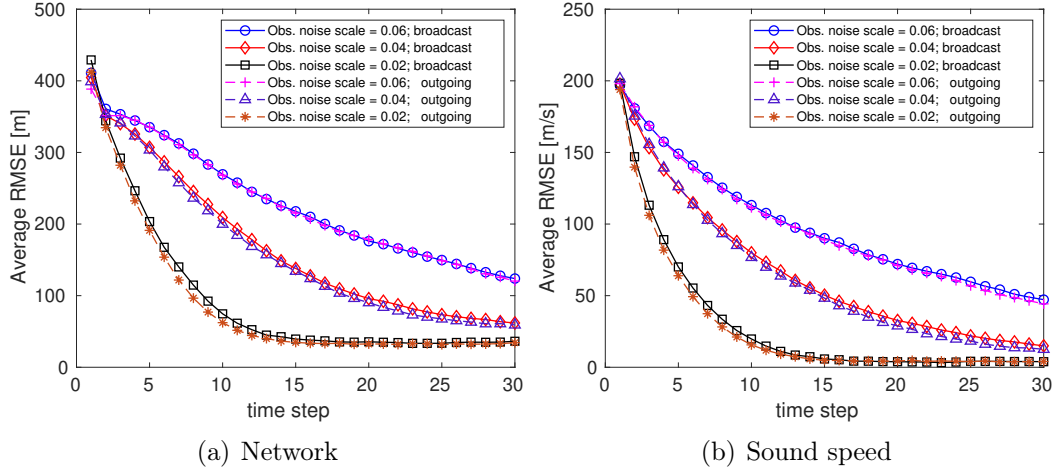
Figure 4.8: Comparison of the broadcast scheme and target specific message scheme.

4.6.2 Time-varying Isogradient Sound Speed Model

In this section, we investigate the algorithm performance in a time-varying isogradient sound speed. The length of the area of interest is $d_{\max} = 2$ km, and 100 mobile agents are randomly scattered in the area. The parameters of the sound speed model in $\boldsymbol{\eta}$ are modeled as independent random walk processes as in (4.6) with $\bar{b} = 1500$ m/s, and $\bar{a} = 0.1$. The standard deviations of the evolution noises are $\sigma_a = 0.01$ and $\sigma_b = 25$ m/s, respectively. 200 Monte Carlo realizations are simulated to obtain the following average results.

The performance metric for b is the RMSE similarly as defined in (4.40). Since a is usually less than 1, using RMSE as performance metric will not provide much insight.

Thus, we define the normalized absolute error (NAE) as the metric for a,

$$\text{NAE}_a[k] = \frac{1}{M} \sum_i^M |\hat{a}_{i,k} - a_k|/|a_k|, \tag{4.41}$$

where $\hat{a}_{i,k}$ is the estimated sound speed model parameter at the estimated location $\hat{\mathbf{x}}_i$, and a_k is the true parameter at time k.
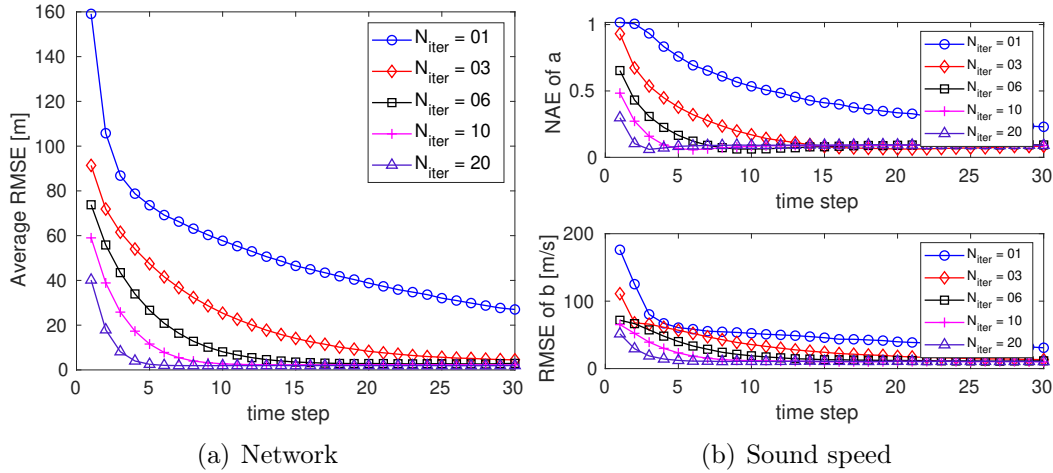
Figure 4.9: Average tracking performance of the network and the isogradient, time-varying sound speed with different iterations N_{iter}.

Fig. 4.9 shows the tracking performance of the proposed algorithm with different number of iterations at each time step. The communication scale and observation noise scale are $r_d = 0.4$ and $r_o = 0.01$, respectively. It can be observed that the proposed algorithm takes longer time to converge with a smaller number of iterations at each time step. However, as the time step increases, the results with different iteration setups converge to the same accuracy asymptotically. Since more iterations require more energy-consuming communications, a balanced choice would be some

142

value between $3 - 6$, beyond which the performance improvement is not significant. Similar results can be observed in simulations of the time-varying uniform sound speed model and spatiotemporal Gaussian process model.

4.6.3   Spatiotemporal Gaussian Process Sound Speed

To investigate the algorithm performance in a GP sound speed model in (4.8), we set $d_{\mathrm{max}} = 10$ km and 100 mobile nodes are randomly deployed in the area. The spatiotemporal sound speed is generated following Gaussian process, the signal standard deviation is $\sigma_f = 20$ m/s, the length scale is $l = 300$ m, and the time scale is $l_t = 1$ s. the observation noise scale is $r_o = 0.01$. $N_{\mathrm{iter}} = 3$ iterations are conducted at each time step. Fig. 4.10 demonstrates how the accuracy changes with the maximum communication distances, under different tested communication scales $r_c = [0.2, 0.3, 0.4, 0.5]$. It can be observed that both the accuracy of the network location and the sound speed can be improved with a longer communication distance. Because as the communication distance increases, more and more sensor nodes are in the neighborhood for message exchange and measurement collections. Additionally, one can draw the conclusion that the maximum communication distance should exceed certain value depending on the number of nodes in the network in order to make the algorithm converge. In other words, the algorithm converges when the number of

143

neighbors for each node is large enough. Once the algorithm converges, the performance will be similar eventually as time goes on. This conclusion is also supported by simulation results with different sound speed models.
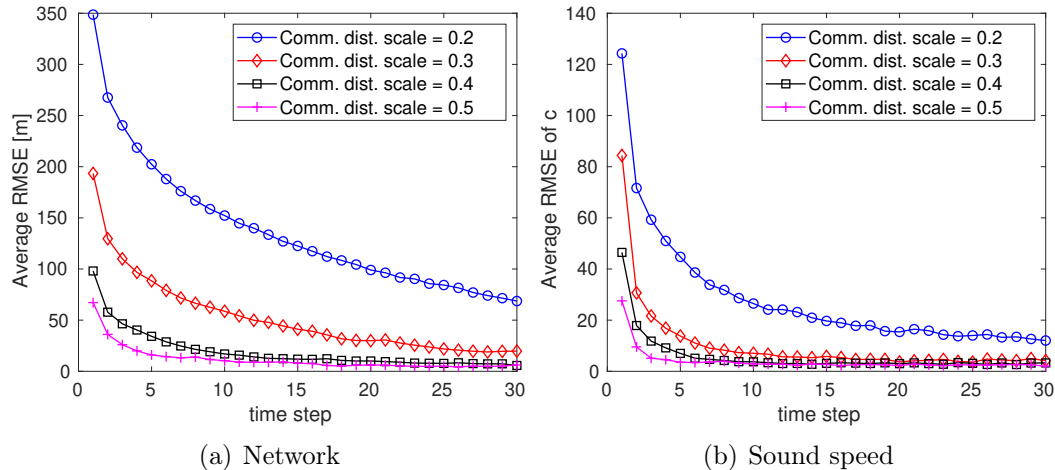
Figure 4.10: Average tracking performance in spatiotemporal GP sound speed model with different communication distances.

4.6.4 Performance Improvement of the Sound Speed-aware Algorithm

In this section, we conduct an extra experiment to understand how much gain can be achieved by the proposed algorithm in an isogradient sound speed field against the algorithm that assumes a homogeneous sound speed field. The communication scale is set as $r_d = 0.4$, the number of iterations at each time step is $N_{\text{iter}} = 10$. The results are averaged over 200 runs. At each run, the sound speed is set as time-varying

144
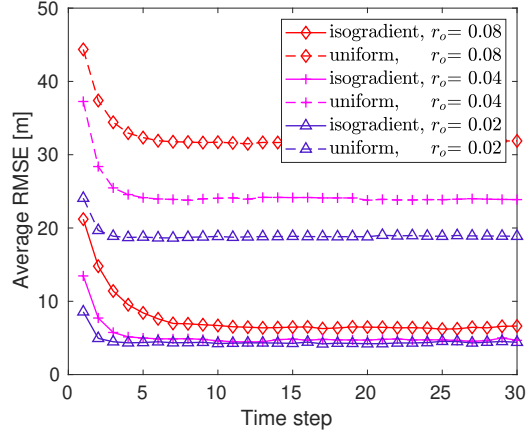
Figure 4.11: Comparison of the tracking performance between isogradient and uniform sound speed.

isogradient model. Both the algorithm with isogradient sound speed model and the algorithm with uniform sound speed are run in the same simulated environment. The other simulation parameters are the same as the setup for isogradient sound speed model. Fig. 4.11 compares the performance of the two algorithms with different observation noise variances. It shows that the proposed algorithm for isogradient model achieves a significant gain as compared to the one assuming the sound speed as homogeneous. Depending on the noise level, the gain could be as much as 25 meters in terms of average RMSE localization errors.

4.7 Summary

This Chapter studied the estimation of spatially and temporally varying sound speed and tracking of AUVs in a mobile network. Several sound speed models are used to

emphasise the different spatial-temporal variations. A distributed Gaussian message passing algorithm is proposed to recursively estimated the time-varying isogradient sound speed and the locations of the AUVs. The algorithm is extended to capitalize on the spatial correlation of the sound speed. Extensive simulations are conducted to evaluate the proposed algorithms. Results reveal that the AUV network and the sound speed parameters can be well tracked. Moreover, significant improvement of localization performance is achieved when the sound speed stratification effect is taken into consideration.

Chapter 5

Conclusions

This dissertation treats the UWA channel variations from different perspectives and emphasizes applications with sequential measurements in UWA networks.

The insights of temporal and spatial variations are obtained from substantial experimental data. Comparisons of mobile and stationary channels, open-water and under-ice channels are presented. Transceivers will gain communication margin if the environment specific channel properties are taken into consideration. The experimental observations inspire two research topics related to the channel variations.

The large-scale, slowly time-varying channels statistics are modeled and predicted from a date-driven perspective. By passing the intricate physical interaction between acoustic waves and the underwater environment, statistical correlation is utilized to

capture the dependence of the temporal channel variation on the environment. As a general signal processing approach, the proposed dynamical model and recursive algorithms can be used for the prediction of a broad range of channel parameters.

As it is impossible to model all the environment factors to understand the channel variations from a physical perspective, the most relevant one - sound speed distribution is singled out and studied. Leveraging the Bayesian framework, the joint PDF of variables of interest is represented by normal factor graph. Considering the temporal causal constraint and the connectivity constraint of the mobile AUV network, an iterative algorithm is adopted to simultaneously track the agent location (a local variable to the agent) and the sound speed parameters (a global variable). Without collecting and processing in a computing center, the proposed approach distribute the computation load to the network with certain communication cost.

Still, many problems need to be worked on in the future. With prosperity of UWA networks, correlation between different communication links could be capitalized on to predict the link status of the complete network. Moreover, the reincarnation of neural networks in the artificial intelligence community makes it very promising to explore the sequential models, such as recurrent neural network (RNN), to solve the complex channel variation problems.

References

[1] Sun, W.; Wang, Z.-H.; Jamalabdollahi, M.; Reza Zekavat, S. In *Proc. of Asilomar Conf. on Signals, Systems, and Computers*, 2014.

[2] Sun, W.; Wang, C.; Wang, Z.-H.; Song, M. In *Proc. of the ACM Intl. Conf. on Underwater Networks (WUWNet)*, page 39. ACM, 2015.

[3] Barazideh, R.; Sun, W.; Natarajan, B.; Nikitin, A. V.; Wang, Z. In *2019 IEEE 9th Annual Computing and Communication Workshop and Conference (CCWC)*, pages 0880–0885. IEEE, 2019.

[4] Moridian, B.; Wei, L.; Hoffman, J.; Sun, W.; Page, B.; Sietsem, M.; Zhang, Y.; Wang, Z.; Mahmoudian, N. In *2018 IEEE/OES Autonomous Underwater Vehicle Workshop (AUV)*, pages 1–6. IEEE, 2018.

[5] Sun, W.; Wang, Z. *IEEE Access* **2018**, *6*, 73984–74002.

[6] Domingo, M. C. *IEEE Transactions on Antennas and Propagation* **2012**, *60*(6), 2929–2939.

[7] Hanson, F.; Radic, S. *Applied optics* **2008**, *47*(2), 277–283.

[8] Lanbo, L.; Shengli, Z.; Jun-Hong, C. *Wireless Communications and Mobile Computing* **2008**, *8*(8), 977–994.

[9] Wenz, G. M. *J. Acoust. Soc. Am.* **1962**, *34*(12), 1936–1956.

[10] Duan, W.; Tao, J.; Zheng, Y. R. *IEEE Journal of Oceanic Engineering* **2017**, *43*(3), 792–804.

[11] Northrop, J.; Colborn, J. *Journal of Geophysical Research* **1974**, *79*(36), 5633–5641.

[12] Chen, C.-T.; Millero, F. J. *J. Acoust. Soc. Am.* **1977**, *62*(5), 1129–1135.

[13] Knudsen, V.; Alford, R.; Emling, J. *Survey of Underwater Sound: Report No. 3 Ambient Noise;* National Defense Research Committee, Office of Scientific Research and Development, 1944.

[14] Hildebrand, J. A. *Marine Ecology Progress Series* **2009**, *395*, 5–20.

[15] Ma, B. B.; Nystuen, J. A.; Lien, R.-C. *J. Acoust. Soc. Am.* **2005**, *117*(6), 3555–3565.

[16] Potter, J. R.; Porter, M. B.; Preisig, J. C. *IEEE Journal of Oceanic Engineering* **2013**, *38*(4), 603–613.

[17] Johnson, M.; Herold, D.; Catipovic, J. In *Proceedings of OCEANS'94*, Vol. 3, pages III–467. IEEE, 1994.

[18] Freitag, L.; Koski, P.; Morozov, A.; Singh, S.; Partan, J. In *2012 Oceans*, pages 1–8. IEEE, 2012.

[19] 2014 elk river chemical spill. Wikipedia. **2014**.

[20] E. coli contaminates portland, ore., tap water. News, N. **2015**.

[21] Yang, X.; Ong, K.; Dreschel, W.; Zeng, K.; Mungle, C.; Grimes, C. *Sensors* **2002**, *2*(11), 455–472.

[22] Telci, I. T.; Nam, K.; Guan, J.; Aral, M. M. *Journal of environmental management* **2009**, *90*(10), 2987–2998.

[23] Haugan, P. M.; Sagen, H.; Sandven, S. In *2012 Oceans-Yeosu*, pages 1–5. IEEE, 2012.

[24] Li, W.; Preisig, J. C. *IEEE Journal of Oceanic Engineering* **2007**, *32*(4), 927–939.

[25] Berger, C. R.; Zhou, S.; Preisig, J. C.; Willett, P. In *OCEANS 2009-EUROPE*, pages 1–8. IEEE, 2009.

[26] Stojanovic, M.; Catipovic, J. A.; Proakis, J. G. *IEEE journal of oceanic engineering* **1994**, *19*(1), 100–111.

[27] Chitre, M. *J. Acoust. Soc. Am.* **2007**, *122*(5), 2580–2586.

[28] Francois, R.; Garrison, G. *The Journal of the Acoustical Society of America* **1982**, *72*(3), 896–907.

[29] Francois, R.; Garrison, G. *J. Acoust. Soc. Am.* **1982**, *72*(6), 1879–1890.

[30] Browning, D. G.; Jones, E. N.; Mellen, R. H.; Thorp, W. H. *Science* **1968**, *162*(3858), 1120–1121.

[31] Browning, D.; Gorman, J.; Jones, E.; Thorp, W.; Mellen, R.; Weigle, F. *Nature Physical Science* **1972**, *240*(100), 86.

[32] Fisher, F.; Simmons, V. In *OCEAN 75 Conference*, pages 21–24. IEEE, 1975.

[33] Tomasi, B.; Toni, L.; Casari, P.; Rossi, L.; Zorzi, M. In *Proc. of MTS/IEEE OCEANS Conf.*, pages 1–8. IEEE, 2010.

[34] Hashemi, H.; Tholl, D. *IEEE Transactions on Vehicular Technology* **1994**, *43*(1), 110–120.

[35] van Walree, P. A. *IEEE J. Ocean. Eng.* **2013**, *38*(4), 614–631.

[36] Aquasent acoustic modems. Technologyl, A. S. N. **2015**.

[37] Kaharl, V. A. *Sounding Out the Ocean's Secrets;* National Academey of Sciences, 1999.

[38] Wang, Z.; Zhou, S.; Preisig, J. C.; Pattipati, K. R.; Willett, P. *IEEE Transactions on Signal Processing* **2012**, *60*(6), 3079–3091.

[39] Zhou, S.; Wang, Z.-H. *OFDM for underwater acoustic communications;* John Wiley & Sons, 2014.

[40] Berger, C. R.; Wang, Z.; Huang, J.; Zhou, S. *IEEE Communications Magazine* **2010**, *48*(11), 164–174.

[41] Carbone, N. M.; Hodgkiss, W. S. *IEEE J. Ocean. Eng.* **2000**, *25*(1), 84–94.

[42] Song, A.; Badiey, M.; Song, H.; Hodgkiss, W. S.; Porter, M. B.; others. *J. Acoust. Soc. Am.* **2008**, *123*(2), 856–865.

[43] Kilfoyle, D. B.; Baggeroer, A. B. *IEEE Journal of oceanic engineering* **2000**, *25*(1), 4–27.

[44] Chitre, M.; Shahabudeen, S.; Stojanovic, M. *Marine technology society journal* **2008**, *42*(1), 103–116.

[45] Qarabaqi, P.; Stojanovic, M. *IEEE J. Ocean. Eng.* **2013**, *38*(4), 701–717.

[46] Caiti, A.; Grythe, K.; Hovem, J. M.; Jesus, S. M.; Lie, A.; Munafò, A.; Reinen, T. A.; Silva, A.; Zabel, F. *IEEE J. Ocean. Eng.* **2013**, *38*(4), 758–771.

[47] Tomasi, B.; Preisig, J.; Deane, G. B.; Zorzi, M. In *Proc. of IEEE European Wireless Conf.*, pages 1–6. VDE, 2011.

[48] Chitre, M.; Pelekanakis, K. In *Proc. of Underwater Communications and Networking Conf. (UComms)*, pages 1–4. IEEE, 2014.

[49] Box, G. E.; Jenkins, G. M.; Reinsel, G. C. *Time series analysis: forecasting and control;* Wiley, 4th ed., 2008.

[50] Jensen, F. B.; Kuperman, W. A.; Porter, M. B.; Schmidt, H. *Computational ocean acoustics;* Springer, 2011.

[51] Ainslie, M. A.; McColm, J. G. *J. Acoust. Soc. Am.* **1998**, *103*(3), 1671–1672.

[52] Weston, D. E.; Ching, P. A. *J. Acoust. Soc. Am.* **1989**, *86*(4), 1530–1545.

[53] Jackson, D. *Applied Physics Laboratory, University of Washington, Technical Report* **1994**, *9407.*

[54] van Walree, P. A.; Otnes, R. *IEEE J. Ocean. Eng.* **2013**, *38*(4), 678–688.

[55] Llor, J.; Malumbres, M. P. *Sensors* **2013**, *13*(2), 2279–2294.

[56] Qarabaqi, P.; Stojanovic, M. In *2011 49th Annual Allerton Conference on Communication, Control, and Computing (Allerton)*, pages 445–452. IEEE, 2011.

[57] Bishop, C. M. *Pattern recognition and machine learning;* springer, 2006.

[58] Demirors, E.; Sklivanitis, G.; Santagati, G. E.; Melodia, T.; Batalama, S. N. *IEEE Access* **2018**, *6*, 18602–18615.

[59] Wang, Z.-H.; Wang, C.; Sun, W. In *Proc. of MTS/IEEE OCEANS Conf.*, 2015.

[60] Bar-Shalom, Y.; Li, X. R.; Kirubarajan, T. *Estimation with applications to tracking and navigation;* Wiley-Interscience, 2001.

[61] Weather history and data archieve. Channel, T. W. **2015**.

[62] Rissanen, J. *Automatica* **1978**, *14*(5), 465–471.

154

[63] The Martha's Vinyard coastal observatory. The Woods Hole Oceanographic Institution. **2016**.

[64] Wang, C.; Wang, Z.; Sun, W.; Fuhrmann, D. R. *IEEE Access* **2017**, *6*, 2541–2558.

[65] Nicholson, J.; Healey, A. *Marine Technology Society Journal* **2008**, *42*(1), 44–51.

[66] Baggeroer, A. B.; Kuperman, W.; Schmidt, H. *J. Acoust. Soc. Am.* **1988**, *83*(2), 571–587.

[67] Baggeroer, A. B.; Kuperman, W. A.; Mikhalevsky, P. N. *IEEE J. Ocean. Eng.* **1993**, *18*(4), 401–424.

[68] Huang, C.-F.; Gerstoft, P.; Hodgkiss, W. S. *The Journal of the Acoustical Society of America* **2008**, *123*(6), EL162–EL168.

[69] Candy, J. V.; Sullivan, E. *IEEE J. Ocean. Eng.* **1993**, *18*(3), 240–252.

[70] Carriere, O.; Hermand, J.-P.; Meyer, M.; Candy, J. V. In *OCEANS 2007-Europe*, pages 1–6. IEEE, 2007.

[71] Carrière, O.; Hermand, J.-P.; Candy, J. V. *IEEE Journal of Oceanic Engineering* **2009**, *34*(4), 586–602.

[72] Lin, T.; Michalopoulou, Z.-H. *J. Acoust. Soc. Am.* **2014**, *135*(3), 1115–1126.

[73] Sun, W.; Wang, C.; Wang, Z.; Song, M. In *Proc. of the ACM Intl. Workshop on Underwater Networks (WUWNet)*, page 23. ACM, 2017.

[74] Jain, S.; Ali, M. *IEEE Geoscience and Remote Sensing Letters* **2006**, *3*(4), 467–470.

[75] Bianco, M.; Gerstoft, P. *J. Acoust. Soc. Am.* **2016**, *139*(3), EL90–EL94.

[76] Shiba, H. In *2013 MTS/IEEE OCEANS-Bergen*, pages 1–7. IEEE, 2013.

[77] Ahmed, A.; Younis, M. In *2017 IEEE International Conference on Communications (ICC)*, pages 1–7. IEEE, 2017.

[78] Skarsoulis, E.; Piperakis, G. *The Journal of the Acoustical Society of America* **2009**, *125*(3), 1384–1393.

[79] Mridula, K.; Rahman, N.; Ameer, P. *IET Communications* **2018**, *13*(5), 528–538.

[80] Paull, L.; Saeedi, S.; Seto, M.; Li, H. *IEEE Journal of Oceanic Engineering* **2013**, *39*(1), 131–149.

[81] Vaganay, J.; Leonard, J. J.; Curcio, J. A.; Willcox, J. S. In *2004 IEEE/OES Autonomous Underwater Vehicles (IEEE Cat. No. 04CH37578)*, pages 59–65. IEEE, 2004.

[82] Bahr, A.; Leonard, J. J.; Fallon, M. F. *The International Journal of Robotics Research* **2009**, *28*(6), 714–728.

[83] Newman, P.; Leonard, J. In *2003 IEEE International Conference on Robotics and Automation (Cat. No. 03CH37422)*, Vol. 2, pages 1921–1926. Ieee, 2003.

[84] Huang, Y.; Liang, W.; Yu, H.-b.; Xiao, Y. *Wireless Communications and Mobile Computing* **2008**, *8*(8), 1023–1033.

[85] Detweiler, C. C. J. *Passive mobile robot localization within a fixed beacon field* PhD thesis, Massachusetts Institute of Technology, **2006**.

[86] Isbitiren, G.; Akan, O. B. *IEEE Transactions on Vehicular Technology* **2011**, *60*(8), 3897–3906.

[87] Ramezani, H.; Rad, H. J.; Leus, G. *IEEE Trans. Signal Processing* **2013**, *61*(6), 1434–1446.

[88] Ameer, P.; Jacob, L. *IEEE Communications Letters* **2010**, *14*(10), 930–932.

[89] Ameer, P.; Jacob, L. *Wireless networks* **2013**, *19*(7), 1679–1690.

[90] Shang, Y.; Ruml, W. In *IEEE INFOCOM 2004*, Vol. 4, pages 2640–2651. IEEE, 2004.

[91] Agrafiotis, D. K. *Journal of computational chemistry* **2003**, *24*(10), 1215–1221.

[92] Kim, Y.; Noh, Y.; Kim, K. *IEEE Communications Letters* **2017**, *21*(11), 2328–2331.

[93] Porter, M. B.; Liu, Y.-C. *Theoretical and computational acoustics* **1994**, *2*, 947–956.

[94] Porter, M. B. *IEEE Journal of Oceanic Engineering* **1993**, *18*(4), 425–437.

[95] Ramezani, H.; Leus, G. *Sensors* **2012**, *12*(3), 2996–3017.

[96] Rasmussen, C. E. In *Summer School on Machine Learning*, pages 63–71. Springer, 2003.

[97] Jiang, Y.; Leung, V. C. In *2007 International Symposium on Signals, Systems and Electronics*, pages 525–528. IEEE, 2007.

[98] Kschischang, F. R.; Frey, B. J.; Loeliger, H.-A.; others. *IEEE Transactions on information theory* **2001**, *47*(2), 498–519.

[99] Loeliger, H.-A.; Dauwels, J.; Hu, J.; Korl, S.; Ping, L.; Kschischang, F. R. *Proceedings of the IEEE* **2007**, *95*(6), 1295–1322.

[100] Sudderth, E. B.; Ihler, A. T.; Isard, M.; Freeman, W. T.; Willsky, A. S. *Communications of the ACM* **2010**, *53*(10), 95–103.

[101] Wymeersch, H.; Lien, J.; Win, M. Z. *Proceedings of the IEEE* **2009**, *97*(2), 427–450.

[102] Forney, G. D. *IEEE Transactions on Information Theory* **2001**, *47*(2), 520–548.

[103] Xu, Y.; Choi, J.; Oh, S. *IEEE Transactions on Robotics* **2011**, *27*(6), 1118–1131.

Appendix A

Derivation from Eq. (3.15) to Eqs. (3.16) and (3.17) in Chapter 3

According to (3.15), we have the batched representation of $Q_k(\boldsymbol{\Theta}|\hat{\boldsymbol{\Theta}})$,

$$Q_k(\boldsymbol{\Theta}|\hat{\boldsymbol{\Theta}}) = \mathbb{E}[\ln f(x_k, y_k|\mathbf{x}_{k-1}, \boldsymbol{\Theta})] +$$

$$\sum_{k'=0}^{k-1} \lambda^{k-k'} \mathbb{E}[\ln f(x_{k'}, y_{k'}|\mathbf{x}_{k'-1}, \boldsymbol{\Theta})] + \ln f(\mathbf{x}_{-1}|\boldsymbol{\Theta}), \qquad (A.1)$$

where the expectation of $[\ln f(x_k, y_k|\mathbf{x}_{k-1}, \boldsymbol{\Theta})]$ is performed with respect to $\tilde{f}(x_k, \mathbf{x}_{k-1}|y_k, \mathbf{y}_0^{k-1}, \hat{\boldsymbol{\Theta}})$, and the expectation of $[\ln f(x_{k'}, y_{k'}|\mathbf{x}_{k'-1}, \boldsymbol{\Theta})]$, $k' < k$ is performed with respect to $\tilde{f}(x_{k'}, \mathbf{x}_{k'-1}|y_{k'}, \mathbf{y}_0^{k'-1}, \hat{\boldsymbol{\Theta}}_{k'})$. Note that $f(x_k, y_k|\mathbf{x}_{k-1}, \boldsymbol{\Theta}) =$

$f(y_k|x_k, \mathbf{\Theta})f(x_k|\mathbf{x}_{k-1}, \mathbf{\Theta})$. We have,

$$Q_k(\mathbf{\Theta}|\hat{\mathbf{\Theta}}) = \mathbb{E}[\ln f(x_k|\mathbf{x}_{k-1}, \mathbf{\Theta})] + \mathbb{E}[\ln f(y_k|x_k, \mathbf{\Theta})]$$
$$+ \sum_{k'=0}^{k-1} \lambda^{k-k'} \{\mathbb{E}[\ln f(x_{k'}|\mathbf{x}_{k'-1}, \mathbf{\Theta})] + \mathbb{E}[\ln f(y_{k'}|x_{k'}, \mathbf{\Theta})]\} + \ln f(\mathbf{x}_{-1}|\mathbf{\Theta}). \qquad (A.2)$$

Substitute $f(y_k|x_k, \mathbf{\Theta}) = \mathcal{N}(\gamma_0 + x_k + \mathbf{b}^\mathrm{T}\mathbf{u}_k, \sigma_v^2)$ and $f(x_k|\mathbf{x}_{k-1}) = \mathcal{N}(\mathbf{a}^\mathrm{T}\mathbf{x}_{k-1}, \sigma_w^2)$ into (A.2), and set the partial derivative of $Q_k(\mathbf{\Theta}|\hat{\mathbf{\Theta}})$ with respect to each unknown parameter in the set $\mathbf{\Theta} = \{\gamma_0, \mathbf{a}, \mathbf{b}, \sigma_w^2, \sigma_v^2\}$ to zero. One can obtain the batched estimation of the unknown parameters. The recursive estimation can then be derived based on the batched estimation. Next, we take $\mathbf{a}$ as an example to illustrate the derivation of the recursive estimation in (3.16a). The recursive estimation of all the other unknown parameters can be similarly derived.

Substitute $f(x_{k'}|\mathbf{x}_{k'-1}) = \mathcal{N}(\mathbf{a}^\mathrm{T}\mathbf{x}_{k'-1}, \sigma_w^2)$ into (A.2). We have

$$- Q_k(\mathbf{\Theta}|\hat{\mathbf{\Theta}}) = \mathbb{E}\left[\frac{1}{2\sigma_w^2}(x_k - \mathbf{a}^\mathrm{T}\mathbf{x}_{k-1})^2\right] + \sum_{k'=0}^{k-1} \lambda^{k-k'} \mathbb{E}\left[\frac{1}{2\sigma_w^2}(x_{k'} - \mathbf{a}^\mathrm{T}\mathbf{x}_{k'-1})^2\right] + \text{others.}$$
$$(A.3)$$

Set the partial derivative of $Q_k(\boldsymbol{\Theta}|\hat{\boldsymbol{\Theta}})$ with respect to $\mathbf{a}$ to zero,

$$-\frac{\partial Q_k(\boldsymbol{\Theta}|\hat{\boldsymbol{\Theta}})}{\partial \mathbf{a}} = \mathbb{E}\left[\frac{1}{2\sigma_w^2}(x_k - \mathbf{a}^{\mathrm{T}}\mathbf{x}_{k-1})\mathbf{x}_{k-1}^{\mathrm{T}}\right]$$
$$+ \sum_{k'=0}^{k-1} \lambda^{k-k'}\mathbb{E}\left[\frac{1}{2\sigma_w^2}(x_{k'} - \mathbf{a}^{\mathrm{T}}\mathbf{x}_{k'-1})\mathbf{x}_{k'-1}^{\mathrm{T}}\right] = 0. \qquad (A.4)$$

We obtained the batched estimation of $\mathbf{a}$ at time k,

$$\hat{\mathbf{a}}_k = \mathbf{M}_{k-1}^{-1}\boldsymbol{\pi}_k, \qquad (A.5)$$

where the matrix $\mathbf{M}_{k-1}$ and the vector $\boldsymbol{\pi}_k$ are defined, respectively, as

$$\mathbf{M}_{k-1} := \mathbb{E}[\mathbf{x}_{k-1}\mathbf{x}_{k-1}^{\mathrm{T}}] + \sum_{k'=0}^{k-1} \lambda^{k-k'}\mathbb{E}[\mathbf{x}_{k'-1}\mathbf{x}_{k'-1}^{\mathrm{T}}],$$

$$\boldsymbol{\pi}_k := \mathbb{E}[x_k\mathbf{x}_{k-1}] + \sum_{k'=0}^{k-1} \lambda^{k-k'}\mathbb{E}[x_{k'}\mathbf{x}_{k'-1}].$$

which can be recursively represented as,

$$\mathbf{M}_{k-1} = \lambda\mathbf{M}_{k-2} + \mathbb{E}[\mathbf{x}_{k-1}\mathbf{x}_{k-1}^{\mathrm{T}}],$$

$$\boldsymbol{\pi}_k = \lambda\boldsymbol{\pi}_{k-1} + \mathbb{E}[x_k\mathbf{x}_{k-1}].$$

According to the Woodbury matrix identity [60], we have

$$\mathbf{M}_{k-1}^{-1} = \lambda^{-1}\mathbf{M}_{k-2}^{-1} - \lambda^{-1}\mathbf{M}_{k-1}^{-1}\mathbb{E}[\mathbf{x}_{k-1}\mathbf{x}_{k-1}^{\mathrm{T}}]\mathbf{M}_{k-2}^{-1}. \tag{A.6}$$

The recursive representation of (A.5) can then be derived as,

$$
\begin{aligned}
\hat{\mathbf{a}}_k &= \mathbf{M}_{k-1}^{-1}\mathbb{E}[x_k\mathbf{x}_{k-1}] + \left(\lambda^{-1}\mathbf{M}_{k-2}^{-1} - \lambda^{-1}\mathbf{M}_{k-1}^{-1}\mathbb{E}[\mathbf{x}_{k-1}\mathbf{x}_{k-1}^{\mathrm{T}}]\mathbf{M}_{k-2}^{-1}\right)\lambda\boldsymbol{\pi}_{k-1} \\
&= \mathbf{M}_{k-1}^{-1}\mathbb{E}[x_k\mathbf{x}_{k-1}] + \left(\mathbf{M}_{k-2}^{-1}\boldsymbol{\pi}_{k-1} - \mathbf{M}_{k-1}^{-1}\mathbb{E}[\mathbf{x}_{k-1}\mathbf{x}_{k-1}^{\mathrm{T}}]\mathbf{M}_{k-2}^{-1}\boldsymbol{\pi}_{k-1}\right) \\
&= \mathbf{M}_{k-1}^{-1}\mathbb{E}[x_k\mathbf{x}_{k-1}] + \left(\hat{\mathbf{a}}_{k-1} - \mathbf{M}_{k-1}^{-1}\mathbb{E}[\mathbf{x}_{k-1}\mathbf{x}_{k-1}^{\mathrm{T}}]\hat{\mathbf{a}}_{k-1}\right) \\
&= \hat{\mathbf{a}}_{k-1} + \mathbf{M}_{k-1}^{-1}\left(\mathbb{E}[x_k\mathbf{x}_{k-1}] - \mathbb{E}[\mathbf{x}_{k-1}\mathbf{x}_{k-1}^{\mathrm{T}}]\hat{\mathbf{a}}_{k-1}\right). \tag{A.7}
\end{aligned}
$$

For the proposed recursive and iterative algorithm in Section 3.3.2, corresponding to the parameter set estimation $\hat{\boldsymbol{\Theta}}_k^{(i)}$ in the ith iteration, the result in (A.7) can be generalized to (3.16a) which is obtained by maximizing $Q_k(\boldsymbol{\Theta}|\hat{\boldsymbol{\Theta}}_k^{(i)})$.

Appendix B

Detailed Derivations for Chapter 4

B.1 Gradients of τ in Uniform and Isogradient Sound Speed Fields

B.1.1 Uniform sound speed field

For a homogeneous sound speed model, the distance between the transmitter at location (r_T, z_T) and the receiver at location (r_R, z_R) is $d = \sqrt{(r_T - r_R)^2 + (z_T - z_R)^2}$, and the propagation delay is $\tau = d/c$. The partial derivatives w.r.t coordinates can

be easily found. For example,

$$\frac{\partial \tau}{\partial r_{\mathrm{T}}} = \frac{r_{\mathrm{T}} - r_{\mathrm{R}}}{cd}, \tag{B.1}$$

$$\frac{\partial \tau}{\partial c} = \frac{-d}{c^2}. \tag{B.2}$$

B.1.2 Isogradient sound speed field

According to the ray theory, the propagation delay in an isogradient sound speed field can be obtained analytically as [87],

$$\tau = -\frac{1}{a} \left(\log \frac{1 + \sin \theta_{\mathrm{T}}}{\cos \theta_{\mathrm{T}}} - \log \frac{1 + \sin \theta_{\mathrm{R}}}{\cos \theta_{\mathrm{R}}} \right), \tag{B.3}$$

where θ_{T} and θ_{R} are the angle between the ray and the horizontal direction at the transmitter and the receiver, respectively. Define $\theta_{\mathrm{T}} = \beta + \alpha$ and $\theta_{\mathrm{R}} = \beta - \alpha$, and α and β can be found by solving Eqs. (10) and (11) in [87]. The gradients w.r.t. the locations can be computed using Eqs. (13) to (18) in [87].

The gradient of the propagation delay w.r.t. the sound speed parameters, i.e. $\partial \tau / \partial a$

and $\partial \tau / \partial b$ are derived next. From (B.3) one can obtain

$$\frac{\partial \tau}{\partial b} = \frac{1}{a} \left(\frac{1}{\cos \theta_{\mathrm{T}}} + \frac{1}{\cos \theta_{\mathrm{R}}} \right) \frac{\partial \alpha}{\partial b}, \tag{B.4}$$

$$\frac{\partial \tau}{\partial a} = -\frac{\tau}{a} + \frac{1}{a} \left(\frac{1}{\cos \theta_{\mathrm{T}}} + \frac{1}{\cos \theta_{\mathrm{R}}} \right) \frac{\partial \alpha}{\partial a}, \tag{B.5}$$

where we have used (B.3) and the fact that β depends only on the locations of the transmitter and the receiver, thus $\partial \theta_{\mathrm{R}} / \partial b = \partial \alpha / \partial b$, $\partial \theta_{\mathrm{T}} / \partial b = -\partial \alpha / \partial b$, $\partial \theta_{\mathrm{R}} / \partial a = \partial \alpha / \partial a$, and $\partial \theta_{\mathrm{T}} / \partial a = -\partial \alpha / \partial a$. To this point, we still need $\partial \alpha / \partial b$ and $\partial \alpha / \partial a$ to solve (B.4) and (B.5), which can be obtained by performing partial derivative on both sides of (B.3). After simple manipulations, we list the results below

$$\frac{\partial \alpha}{\partial a} = \frac{b(z_{\mathrm{T}} - z_{\mathrm{R}})}{(b + a z_{\mathrm{R}})^2} \frac{(\cos \alpha - \sin \alpha \tan \beta)^2}{2 \tan \beta}, \tag{B.6}$$

$$\frac{\partial \alpha}{\partial b} = \frac{a(z_{\mathrm{R}} - z_{\mathrm{T}})}{(b + a z_{\mathrm{R}})^2} \frac{(\cos \alpha - \sin \alpha \tan \beta)^2}{2 \tan \beta}. \tag{B.7}$$

In the special case where $r_{\mathrm{T}} = r_{\mathrm{R}}$, the propagation delay becomes,

$$\tau = -\mathrm{sign}(z_{\mathrm{R}} - z_{\mathrm{T}}) \cdot \frac{1}{a} \log \frac{c(z_{\mathrm{T}})}{c(z_{\mathrm{R}})}, \tag{B.8}$$

where sign(x) is the sign of x. When $z_\mathrm{T} > z_\mathrm{R}$, the corresponding gradients are

$$\frac{\partial \tau}{\partial r_\mathrm{T}} = \frac{\partial \tau}{\partial r_\mathrm{R}} = 0, \tag{B.9}$$

$$\frac{\partial \tau}{\partial z_\mathrm{R}} = -\frac{1}{b + a z_\mathrm{R}}, \tag{B.10}$$

$$\frac{\partial \tau}{\partial z_\mathrm{T}} = \frac{1}{b + a z_\mathrm{T}}, \tag{B.11}$$

$$\frac{\partial \tau}{\partial a} = \frac{1}{a^2} \log \frac{b + a z_\mathrm{R}}{b + a z_\mathrm{T}} - \frac{b(z_\mathrm{R} - z_\mathrm{T})}{a(b + a z_\mathrm{R})(b + a z_\mathrm{T})}, \tag{B.12}$$

$$\frac{\partial \tau}{\partial b} = \frac{z_\mathrm{R} - z_\mathrm{T}}{(b + a z_\mathrm{R})(b + a z_\mathrm{T})}. \tag{B.13}$$

When $z_\mathrm{T} < z_\mathrm{R}$, the signs of the above gradients are negated. During numerical implementation, when two nodes are approximately vertically aligned, it is safe to consider $r_\mathrm{T} = r_\mathrm{R}$ and use the corresponding results to avoid numerical problems caused by $\frac{1}{r_\mathrm{T} - r_\mathrm{R}}$ in the results of the common cases.

B.2   Gaussian Process Regression

The Gaussian process defined in (4.8) is determined by the mean function $m_c(\mathbf{s})$ and the covariance function $\mathcal{K}(\mathbf{s}, \mathbf{s}')$ defined in (4.9). Assume some noisy observations of the function, e.g. $\tilde{y}(\mathbf{s}_i)$, are available at $\mathbf{s}_i$ for $i \in \mathcal{M}$ as

$$y(\mathbf{s}_i) = c(\mathbf{s}_i) + \epsilon, \tag{B.14}$$

where $\epsilon_i \sim \mathcal{N}(0, \sigma_\epsilon^2)$ is the additive Gaussian noise. Stack the observations into a vector $\mathbf{y} := [y(\mathbf{s}_1), y(\mathbf{s}_2), \cdots, y(\mathbf{s}_M),]^{\mathrm{T}}$. $\mathbf{y}$ follows Gaussian distribution,

$$\mathbf{y} \sim \mathcal{N}(\mathbf{m}, \mathbf{V}), \tag{B.15}$$

where $\mathbf{m}$ and $\mathbf{V}$ are the mean and the covariance matrix, respectively. The i-th element of $\mathbf{m}$ is $[\mathbf{m}]_i = m_c(\mathbf{s}_i)$, and the (i, j)-th element of the covariance matrix is $[V]_{ij} = \mathcal{K}_c(\mathbf{s}_i, \mathbf{s}_j) + \delta_{ij}\sigma_\epsilon^2$, which is related to the distance between $\mathbf{s}_i$ and $\mathbf{s}_j$ and the uncertainty of the measurement itself.

Denote $\mathbf{c}_*$ as the Gaussian process at interested locations $\mathbf{s}_*$. According to the Gaussian Process Regression (GPR) algorithm[96], $[\mathbf{c}_*^{\mathrm{T}}, \mathbf{y}^{\mathrm{T}}]^{\mathrm{T}}$ is jointly Gaussian, thus the conditional distribution of $\mathbf{c}_*$ given $\mathbf{y}$ is also Gaussian, i.e., $p(\mathbf{c}_*|\mathbf{y}) \sim \mathcal{N}(\mathbf{m}_*, \mathbf{C}_*)$, and

$$\mathbf{m}_* = \mathbf{m}_{\mathbf{s}_*} + \mathbf{V}_{\mathbf{s}_*,\mathbf{s}} \mathbf{V}^\dagger (\mathbf{y} - \mathbf{m}), \tag{B.16}$$

$$\mathbf{V}_* = \mathbf{V}_{\mathbf{s}_*} - \mathbf{V}_{\mathbf{s}_*,\mathbf{s}} \mathbf{V}^\dagger \mathbf{V}_{\mathbf{s}_*,\mathbf{s}}^{\mathrm{T}}, \tag{B.17}$$

where $\mathbf{V}_{\mathbf{s}_*,\mathbf{s}}$ is the covariance matrix of the variables at $\mathbf{s}_*$ and $\mathbf{s}$.

Appendix C

Letters of Permission

C.1   Permission Letters for Chapter 2

IEEE
Requesting permission to reuse content from an IEEE publication

Title: Experimental study on the difference between acoustic communication channels in freshwater rivers/lakes and in oceans

Conference Proceedings: 2014 48th Asilomar Conference on Signals, Systems and Computers

Author: Wensheng Sun

Publisher: IEEE

Date: Nov. 2014

Copyright © 2014, IEEE

Thesis / Dissertation Reuse

The IEEE does not require individuals working on a thesis to obtain a formal reuse license, however, you may print out this statement to be used as a permission grant:

Requirements to be followed when using any portion (e.g., figure, graph, table, or textual material) of an IEEE copyrighted paper in a thesis:

1) In the case of textual material (e.g., using short quotes or referring to the work within these papers) users must give full credit to the original source (author, paper, publication) followed by the IEEE copyright line © 2011 IEEE.
2) In the case of illustrations or tabular material, we require that the copyright line © [Year of original publication] IEEE appear prominently with each reprinted figure and/or table.
3) If a substantial portion of the original paper is to be used, and if you are not the senior author, also obtain the senior author's approval.

Requirements to be followed when using an entire IEEE copyrighted paper in a thesis:

1) The following IEEE copyright/ credit notice should be placed prominently in the references: © [year of original publication] IEEE. Reprinted, with permission, from [author names, paper title, IEEE publication title, and month/year of publication]
2) Only the accepted version of an IEEE copyrighted paper can be used when posting the paper or your thesis on-line.
3) In placing the thesis on the author's university website, please display the following message in a prominent place on the website: In reference to IEEE copyrighted material which is used with permission in this thesis, the IEEE does not endorse any of [university/educational entity's name goes here]'s products or services. Internal or personal use of this material is permitted. If interested in reprinting/republishing IEEE copyrighted material for advertising or promotional purposes or for creating new collective works for resale or redistribution, please go to http://www.ieee.org/publications_standards/publications/rights/rights_link.html to learn how to obtain a License from RightsLink.

If applicable, University Microfilms and/or ProQuest Library, or the Archives of Canada may supply single copies of the dissertation.

BACK   CLOSE WINDOW

RightsLink®

IEEE
Requesting permission to reuse content from an IEEE publication

Title: A Low-cost Mobile Infrastructure for Multi-AUV Networking

Conference Proceedings: 2018 IEEE/OES Autonomous Underwater Vehicle Workshop (AUV)

Author: Barzin Moridian

Publisher: IEEE

Date: Nov. 2018

Copyright © 2018, IEEE

Thesis / Dissertation Reuse

The IEEE does not require individuals working on a thesis to obtain a formal reuse license, however, you may print out this statement to be used as a permission grant:

Requirements to be followed when using any portion (e.g., figure, graph, table, or textual material) of an IEEE copyrighted paper in a thesis:

1) In the case of textual material (e.g., using short quotes or referring to the work within these papers) users must give full credit to the original source (author, paper, publication) followed by the IEEE copyright line © 2011 IEEE.
2) In the case of illustrations or tabular material, we require that the copyright line © [Year of original publication] IEEE appear prominently with each reprinted figure and/or table.
3) If a substantial portion of the original paper is to be used, and if you are not the senior author, also obtain the senior author's approval.

Requirements to be followed when using an entire IEEE copyrighted paper in a thesis:

1) The following IEEE copyright/ credit notice should be placed prominently in the references: © [year of original publication] IEEE. Reprinted, with permission, from [author names, paper title, IEEE publication title, and month/year of publication]
2) Only the accepted version of an IEEE copyrighted paper can be used when posting the paper or your thesis on-line.
3) In placing the thesis on the author's university website, please display the following message in a prominent place on the website: In reference to IEEE copyrighted material which is used with permission in this thesis, the IEEE does not endorse any of [university/educational entity's name goes here]'s products or services. Internal or personal use of this material is permitted. If interested in reprinting/republishing IEEE copyrighted material for advertising or promotional purposes or for creating new collective works for resale or redistribution, please go to http://www.ieee.org/publications_standards/publications/rights/rights_link.html to learn how to obtain a License from RightsLink.

If applicable, University Microfilms and/or ProQuest Library, or the Archives of Canada may supply single copies of the dissertation.

BACK   CLOSE WINDOW

Copyright
Clearance
Center

RightsLink®

Home | Create Account | Help | LIVE CHAT

IEEE
Requesting
permission
to reuse
content from
an IEEE
publication

Title: Impulsive Noise Mitigation in Underwater Acoustic Communication Systems: Experimental Studies

Conference Proceedings: 2019 IEEE 9th Annual Computing and Communication Workshop and Conference (CCWC)

Author: Reza Barazideh

Publisher: IEEE

Date: Jan. 2019

Copyright © 2019, IEEE

Thesis / Dissertation Reuse

The IEEE does not require individuals working on a thesis to obtain a formal reuse license, however, you may print out this statement to be used as a permission grant:

Requirements to be followed when using any portion (e.g., figure, graph, table, or textual material) of an IEEE copyrighted paper in a thesis:

1) In the case of textual material (e.g., using short quotes or referring to the work within these papers) users must give full credit to the original source (author, paper, publication) followed by the IEEE copyright line © 2011 IEEE.
2) In the case of illustrations or tabular material, we require that the copyright line © [Year of original publication] IEEE appear prominently with each reprinted figure and/or table.
3) If a substantial portion of the original paper is to be used, and if you are not the senior author, also obtain the senior author's approval.

Requirements to be followed when using an entire IEEE copyrighted paper in a thesis:

1) The following IEEE copyright/ credit notice should be placed prominently in the references: © [year of original publication] IEEE. Reprinted, with permission, from [author names, paper title, IEEE publication title, and month/year of publication]
2) Only the accepted version of an IEEE copyrighted paper can be used when posting the paper or your thesis on-line.
3) In placing the thesis on the author's university website, please display the following message in a prominent place on the website: In reference to IEEE copyrighted material which is used with permission in this thesis, the IEEE does not endorse any of [university/educational entity's name goes here]'s products or services. Internal or personal use of this material is permitted. If interested in reprinting/republishing IEEE copyrighted material for advertising or promotional purposes or for creating new collective works for resale or redistribution, please go to http://www.ieee.org/publications_standards/publications/rights/rights_link.html to learn how to obtain a License from RightsLink.

If applicable, University Microfilms and/or ProQuest Library, or the Archives of Canada may supply single copies of the dissertation.

BACK | CLOSE WINDOW

172

C.2 Permission Letters for Chapter 3

Copyright Clearance Center RightsLink®

Home Create Account Help LIVE CHAT

Title: Online Modeling and Prediction of the Large-Scale Temporal Variation in Underwater Acoustic Communication Channels

Author: Wensheng Sun

Publication: IEEE Access

Publisher: IEEE

Date: 2018

Copyright © 2018, IEEE

Thesis / Dissertation Reuse

The IEEE does not require individuals working on a thesis to obtain a formal reuse license, however, you may print out this statement to be used as a permission grant:

Requirements to be followed when using any portion (e.g., figure, graph, table, or textual material) of an IEEE copyrighted paper in a thesis:

1) In the case of textual material (e.g., using short quotes or referring to the work within these papers) users must give full credit to the original source (author, paper, publication) followed by the IEEE copyright line © 2011 IEEE.
2) In the case of illustrations or tabular material, we require that the copyright line © [Year of original publication] IEEE appear prominently with each reprinted figure and/or table.
3) If a substantial portion of the original paper is to be used, and if you are not the senior author, also obtain the senior author's approval.

Requirements to be followed when using an entire IEEE copyrighted paper in a thesis:

1) The following IEEE copyright/ credit notice should be placed prominently in the references: © [year of original publication] IEEE. Reprinted, with permission, from [author names, paper title, IEEE publication title, and month/year of publication]
2) Only the accepted version of an IEEE copyrighted paper can be used when posting the paper or your thesis on-line.
3) In placing the thesis on the author's university website, please display the following message in a prominent place on the website: In reference to IEEE copyrighted material which is used with permission in this thesis, the IEEE does not endorse any of [university/educational entity's name goes here]'s products or services. Internal or personal use of this material is permitted. If interested in reprinting/republishing IEEE copyrighted material for advertising or promotional purposes or for creating new collective works for resale or redistribution, please go to http://www.ieee.org/publications_standards/publications/rights/rights_link.html to learn how to obtain a License from RightsLink.

If applicable, University Microfilms and/or ProQuest Library, or the Archives of Canada may supply single copies of the dissertation.

BACK CLOSE WINDOW

RightsLink®

Home | Create Account | Help | LIVE CHAT

IEEE
Requesting permission to reuse content from an IEEE publication

Title: Modeling and prediction of large-scale temporal variation in underwater acoustic channels

Conference Proceedings: OCEANS 2016 - Shanghai

Author: Wensheng Sun

Publisher: IEEE

Date: April 2016

Copyright © 2016, IEEE

Thesis / Dissertation Reuse

The IEEE does not require individuals working on a thesis to obtain a formal reuse license, however, you may print out this statement to be used as a permission grant:

Requirements to be followed when using any portion (e.g., figure, graph, table, or textual material) of an IEEE copyrighted paper in a thesis:

1) In the case of textual material (e.g., using short quotes or referring to the work within these papers) users must give full credit to the original source (author, paper, publication) followed by the IEEE copyright line © 2011 IEEE.
2) In the case of illustrations or tabular material, we require that the copyright line © [Year of original publication] IEEE appear prominently with each reprinted figure and/or table.
3) If a substantial portion of the original paper is to be used, and if you are not the senior author, also obtain the senior author's approval.

Requirements to be followed when using an entire IEEE copyrighted paper in a thesis:

1) The following IEEE copyright/ credit notice should be placed prominently in the references: © [year of original publication] IEEE. Reprinted, with permission, from [author names, paper title, IEEE publication title, and month/year of publication]
2) Only the accepted version of an IEEE copyrighted paper can be used when posting the paper or your thesis on-line.
3) In placing the thesis on the author's university website, please display the following message in a prominent place on the website: In reference to IEEE copyrighted material which is used with permission in this thesis, the IEEE does not endorse any of [university/educational entity's name goes here]'s products or services. Internal or personal use of this material is permitted. If interested in reprinting/republishing IEEE copyrighted material for advertising or promotional purposes or for creating new collective works for resale or redistribution, please go to http://www.ieee.org/publications_standards/publications/rights/rights_link.html to learn how to obtain a License from RightsLink.

If applicable, University Microfilms and/or ProQuest Library, or the Archives of Canada may supply single copies of the dissertation.

BACK | CLOSE WINDOW

174

C.3   Permission Letter for Chapter 4

ACM Information for Authors

Author Rights	FAQ

ACM Author Rights

ACM exists to support the needs of the computing community. For over sixty years ACM has developed publications and publication policies to maximize the visibility, impact, and reach of the research it publishes to a global community of researchers, educators, students, and practitioners. ACM has achieved its high impact, high quality, widely-read portfolio of publications with:

- Affordably priced publications

- Liberal Author rights policies

- Wide-spread, perpetual access to ACM publications via a leading-edge technology platform

- Sustainability of the good work of ACM that benefits the profession

ACM Author Rights

▶

CHOOSE

Authors have the option to choose the level of rights management they prefer. ACM offers three different options for authors to manage the publication rights to their work.

- Authors who want ACM to manage the rights and permissions associated with their work, which includes defending against improper use by third parties, can use ACM's traditional copyright transfer agreement.

- Authors who prefer to retain copyright of their work can sign an exclusive licensing agreement, which gives ACM the right but not the obligation to defend the work against improper use by third parties.

- Authors who wish to retain all rights to their work can choose ACM's author-pays option, which allows for perpetual open access through the ACM Digital Library. Authors choosing the author-pays option can give ACM non-exclusive permission to publish, sign ACM's exclusive licensing agreement or sign ACM's traditional copyright transfer agreement. Those choosing to grant ACM a non-exclusive permission to publish may also choose to display a Creative Commons License on their works.

POST

Authors can post the accepted, peer-reviewed version prepared by the author-known as the "pre-print"-to the following sites, with a DOI pointer to the Definitive Version of Record in the ACM Digital Library.

- On Author's own Home Page *and*

- On Author's Institutional Repository *and*

175

- In any repository legally mandated by the agency funding the research on which the work is based *and*

- On any non-commercial repository or aggregation that does not duplicate ACM tables of contents, i.e., whose patterns of links do not substantially duplicate an ACM-copyrighted volume or issue. Non-commercial repositories are here understood as repositories owned by non-profit organizations that do not charge a fee for accessing deposited articles and that do not sell advertising or otherwise profit from serving articles.

DISTRIBUTE

Authors can post an *Author-Izer* link enabling free downloads of the Definitive Version of the work permanently maintained in the ACM Digital Library

- On the Author's own Home Page *or*

- In the Author's Institutional Repository.

REUSE

Authors can reuse any portion of their own work in a new work of *their own* (and no fee is expected) as long as a citation and DOI pointer to the Version of Record in the ACM Digital Library are included.

- Contributing complete papers to any edited collection of reprints for which the author is *not* the editor, requires permission and usually a republication fee.

Authors can include partial or complete papers of their own (and no fee is expected) in a dissertation as long as citations and DOI pointers to the Versions of Record in the ACM Digital Library are included. Authors can use any portion of their own work in presentations and in the classroom (and no fee is expected).

- Commercially produced course-packs that are *sold* to students require permission and possibly a fee.

CREATE

ACM's copyright and publishing license include the right to make Derivative Works or new versions. For example, translations are "Derivative Works." By copyright or license, ACM may have its publications translated. However, ACM Authors continue to hold perpetual rights to revise their own works without seeking permission from ACM.

- If the revision is minor, i.e., less than 25% of new substantive material, then the work should still have ACM's publishing notice, DOI pointer to the Definitive Version, and be labeled a "Minor Revision of"

- If the revision is major, i.e., 25% or more of new substantive material, then ACM considers this a new work in which the author retains full copyright ownership (despite ACM's copyright or license in the original published article) and the author need only cite the work from which this new one is derived.

Minor Revisions and Updates to works already published in the ACM Digital Library are welcomed with the approval of the appropriate Editor-in-Chief or Program Chair.

RETAIN

Authors retain all *perpetual rights* laid out in the ACM Author Rights and Publishing Policy, including, but not limited to:

- Sole ownership and control of third-party permissions to use for artistic images intended for exploitation in other contexts

- All patent and moral rights

176